Measurement of Forward Beauty Photoproduction at HERA Using Semileptonic Decays

Dissertation
zur Erlangung des Doktorgrades
des Fachbereichs Physik
der Universität Hamburg

vorgelegt von
Henning Lüders
aus
Stade

Hamburg
2005

Gutachter der Dissertation:	Prof. Dr. B. Naroska Prof. Dr. P. Schleper
Gutachter der Disputation:	Prof. Dr. B. Naroska Dr. E. Elsen
Datum der Disputation:	26. Oktober 2005
Dekan des Fachbereichs Physik und Vorsitzender des Promotionsauschusses	Prof. Dr. G. Huber

Abstract

Beauty production in the forward region is measured in positron-proton scattering at the H1 experiment at the HERA collider. Events in photoproduction ($Q^2 < 1\,\mathrm{GeV}^2$) are selected with a muon of momentum $p_\mu > 7\,\mathrm{GeV}$ and polar angle $10^\circ < \vartheta < 18^\circ$ and two jets within the polar angle $10^\circ < \vartheta_{\mathrm{jet}} < 170^\circ$ with a minimal transverse energy of 7 GeV for the jet associated to the muon and 6 GeV for the second jet. The event sample was collected in the year 2000, corresponding to an integrated luminosity of $\mathcal{L} = 45\mathrm{pb}^{-1}$. The beauty fraction is extracted using the transverse momentum of the muon relative to the associated jet p_t^{rel}. The cross section in the visible range is measured to be

$$\sigma^{\mathrm{vis}}(e^+p \to b\bar{b}Xe' \to\ jj\mu Xe') = \left[11.0 \pm 2.2(\mathrm{stat.})^{+1.2}_{-1.9}(\mathrm{syst.})\right]\,\mathrm{pb}.$$

The result is found to be twice as high as the leading order QCD prediction, corresponding to two standard deviations of the measurement.

Kurzfassung

Eine Messung von Beauty-Produktion in Vorwärtsrichtung in Positron-Proton-Streuung am H1-Experiment am HERA-Speicherring wird vorgestellt. Photoproduktionsereignisse ($Q^2 < 1\,\mathrm{GeV}^2$) werden selektiert mit einem Myon mit Impuls $p_\mu > 7\,\mathrm{GeV}$ im Polarwinkelbereich $10^\circ < \vartheta < 18^\circ$ sowie zwei Jets im Polarwinkelbereich $10^\circ < \vartheta_{\mathrm{jet}} < 170^\circ$ mit einer minimalen transversalen Energie von 7 GeV für den zum Myon assoziierten Jet und 6 GeV für den zweiten Jet. Der Datensatz wurde im Jahr 2000 aufgenommen und entspricht einer integrierten Luminosität von $\mathcal{L} = 45\mathrm{pb}^{-1}$. Der Beauty-Anteil am Datensatz wird an Hand des großen Transversalimpulses des Myons relativ zum assoziierten Jet bestimmt. Die Messung des Wirkungsquerschnitts im sichtbaren Bereich ergibt:

$$\sigma^{\mathrm{vis}}(e^+p \to b\bar{b}Xe' \to\ jj\mu Xe') = \left[11.0 \pm 2.2(\mathrm{stat.})^{+1.2}_{-1.9}(\mathrm{syst.})\right]\,\mathrm{pb}.$$

Das Ergebnis ist doppelt so hoch wie die Vorhersage aus QCD führender Ordnung, was zwei Standardabweichungen der Messung entspricht.

Contents

Introduction

The Standard Model of particle physics successfully describes almost all measurements performed in the field of high energy physics. In this framework matter is built from two types of fermions, leptons and quarks. The forces between them are mediated via gauge bosons. While leptons can be observed as free particles, quarks are confined in hadrons. Confinement can be described by quantum chromodynamics (QCD), the field theory of the strong interaction.

In practise suitable approximations have to be used for the prediction of experimental results within QCD. The most successful apporach to describe the experimental results is perturbative QCD, which requires the presence of a hard scale in the scattering process. This can be provided by a large centre of mass energy, high transverse momenta or the large mass of the interacting quarks.

At the ep collider HERA the production of beauty hadrons provides a testing ground for perturbative QCD, which has proven to provide a very good description for charm production in e^+e^-, $p\bar{p}$ and ep scattering. Most measurements of beauty production cross sections however have shown results significantly higher than the prediction of perturbative QCD. This came as a surprise, because with the beauty quark being considerably heavier than the charm quark it was expected that perturbative QCD would be more precise for beauty than for charm production. These observations have triggered many new analyses at HERA, extending the measurements into yet uncovered regions of the available phase space. In the last years the understanding of the theoretical description of the measurement has improved and the meaurements and the corresponding theoretical predictions have converged. Nevertheless most mesurements are still somewhat above the theoretical predictions.

In this analysis the visible cross section for beauty production is measured in the forward region, defined by the direction of the outgoing proton beam at the H1 experiment. Beauty production is a relatively rare process at HERA, the cross section being two to three orders of magnitude lower than the total ep scattering cross section. The semimuonic decay channel provides a clear event signature which allows the separation of beauty from charm and light flavours on a statistical basis using the p_t^{rel} method. The large mass

difference in the decay from beauty to charm allows a high transverse momentum of the decay muon relative to the axis of the jet formed by the other decay products of the beauty hadron.

The analysis covers the kinematic region of photoproduction, defined by a very low virtuality of the exchanged photon. In photoproduction the exchanged photon can fluctuate into a hadronic state. If a parton from this state takes part in the hard interaction this is referred to as a resolved process. In the forward region an enrichment of resolved processes with respect to the direct production is expected.

This thesis starts in chapter 1 with a brief description of the theoretical framework. In chapter 2 the H1 experiment at HERA is described. Chapter 3 gives a brief introduction of the strategy of the analysis. The selection of the event sample is described in detail in chapter 4. Based on this selection the visible cross section is extracted and compared to theoretical predictions and other results in chapter 5.

Chapter 1

Beauty Production in Electron Proton Scattering

In this chapter the basic theoretical foundation of this analysis will be laid out. Beginning with the Standard Model and the investigation of the structure of the proton in the framework of deep inelastic scattering (DIS), the important basic principles for beauty production in the regime of photoproduction will be presented.

1.1 The Standard Model

The Standard Model successfully describes almost all phenomena observed in particle physics experiments today. The fundamental particles are fermions which are the constituents of matter and gauge bosons, which mediate the electroweak and the strong force. Gravitation is not treated in the Standard Model.

The fermions, which constitute matter, are grouped into three generations. The stable matter in the universe only consists of particles from the first generation. Each particle has an antiparticle. However large quantities of antimatter have not been observed in the universe, so the universe is believed to consist predominantly of matter. In each generation there is a lepton and the corresponding neutrino and a pair of up and down type quarks. The leptons and quarks and their masses and electromagnetic charges are shown in table 1.1. The Standard Model does not assign a mass to the neutrino. So until recent observations the neutrinos were assumed to be massless. However SNO [4] and other neutrino experiments have proven that the three different neutrino flavours can oscilate into each other and therefore must have have mass differences. Therefore at least two of the neutrino types must have a mass greater than zero. Only upper limits for the neutrino mass have been measured so far.

The forces are mediated via virtual gauge bosons. For the electroweak force these are

generation	lepton	c_{em}	mass	quark	c_{em}	mass
1	e	-1	511 keV	u	$+2/3$	$1.5 - 4.0$ MeV
	ν_e	0	< 3 eV	d	$-1/3$	$4 - 8$ MeV
2	μ	-1	105.7 MeV	c	$+2/3$	$1.15 - 1.35$ GeV
	ν_μ	0	< 0.19 MeV	s	$-1/3$	$80 - 130$ MeV
3	τ	-1	1.777 GeV	t	$+2/3$	174 ± 5.1 GeV
	ν_τ	0	< 18.2 MeV	b	$-1/3$	$4.1 - 4.4$ GeV

Table 1.1: Fundamental fermions in the standard model. c_{em} denotes the electromanetic charge is units of the proton's charge. The value for the charges and masses are taken from [17]. The definitions of the quark masses and details of their derivation can be found there.

the photon, the neutral Z^0, and the charged $W^\pm$ bosons. While the photon is massless, the other electroweak bosons are very heavy, with $M_Z = 91.1876 \pm 0.0021$ GeV and $M_{W^\pm} = 80.425 \pm 0.038$ GeV. The electroweak interaction is described by the theory of *Quantum-Flavour-Dynamics* (QFD). The strong force is mediated via 8 different massless gluons. While all fermions are subject to the electroweak interaction, gluons can only couple to quarks and gluons.

Particles aquire masses by their interactions with the *Higgs* field. However the corresponding Higgs boson has not been observed yet.

1.2 Quantum Chromodynamics

Quantum chromodynamics (QCD) is the field theory of the strong interaction. In the framework of QCD the strong force is mediated via *gluons*. Each quark flavour can appear in three different colour states and the antiquarks in the corresponding anticolour states. Gluons carry a colour-anticolour combination. Whereas quarks can couple also to electroweak gauge bosons, gluons can only couple to particles carrying a net colour charge, i.e. quarks and gluons. The self-coupling of the gluon results in effects, which are not present in electroweak interactions. The strength of the strong interaction is given by the *strong coupling constant* α_s. In contrast to the electromagnetic coupling constant α_{em}, the strong coupling constant depends on the energy scale μ where it is evaluated. This phenomenon is known as the *running* of the strong coupling. In a leading order approximation in α_s this running is given by

$$\alpha_s(\mu) = \frac{12\pi}{(33 - 22n_f)\ln(\mu^2/\Lambda^2_{QCD})}, \tag{1.1}$$

where n_f is the number of quark flavours with mass below μ. Λ_{QCD} is a free parameter

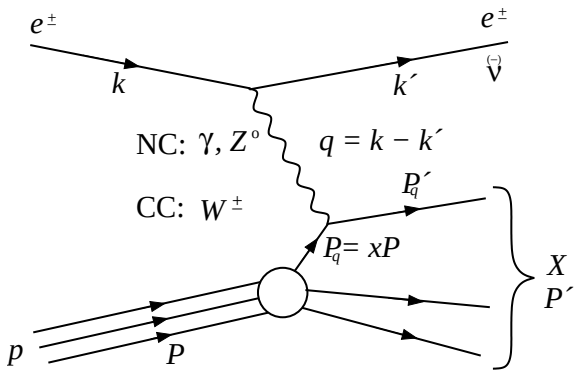

Figure 1.1: Kinematics in electron proton scattering

known as the *QCD scale* and is experimentally determined to be $\Lambda_{QCD} \approx 0.2\,\mathrm{GeV}$.

Large values of μ correspond to short distances. For $\mu \longrightarrow \infty$ equation 1.1 predicts $\alpha_s \longrightarrow 0$. The strong coupling vanishes at short distances and in high energy processes quarks can be treated as free particles. This behaviour is referred to as *asymptotic freedom*[1].

On the other hand α_s becomes large at large distances, corresponding to $\mu \longrightarrow 0$. This may be the explanation for the fact that free quarks have never been observed in any experiment. Quarks are always *confined* in colour neutral *hadrons*. These can be either *mesons*, which consist of a quark and an antiquark, or *baryons*, which consist of three quarks. Recently observations of *pentaquark* states were claimed, which consist of four quarks and one antiquark distinct in flavour.

1.3 Kinematics of Electron Proton Scattering

In electron proton scattering the electron interacts with the proton via the exchange of a gauge boson. In *Charged Current* (CC) interactions a $W^{\pm}$ boson is exchanged and the electron is transformed into a neutrino. In *Neutral Current* (NC) interactions a photon or a Z^0 boson is exchanged and the scattered electron can be detected if the scattering angle is large enough. The scattering process can be described by a set of variables, which are illustrated in figure 1.1. The momentum transfer between the electron and the proton is given by the virtuality of the exchanged boson:

$$Q^2 = -\mathbf{q}^2 = -(\mathbf{k} - \mathbf{k}')^2.$$

[1]For the theoretical prediction of this behaviour David J. Gross, H. David Politzer and Frank Wilczek were awarded the Nobel Prize in physics 2004.

Furthermore there is the centre of mass energy

$$s = (\mathbf{p} + \mathbf{k})^2,$$

the inelasticity defined by

$$y = \frac{\mathbf{p} \cdot \mathbf{q}}{\mathbf{p} \cdot \mathbf{k}}, \tag{1.2}$$

which is equal to the relative energy transfer at the electron vertex, and the Bjorken scaling variable,

$$x = \frac{Q^2}{2\mathbf{p} \cdot \mathbf{q}},$$

equal to the momentum fraction carried by the interacting parton. Neglecting the masses of the interacting particles, these four variables are related by the equation

$$Q^2 = xys. \tag{1.3}$$

This means that in the case of a fixed centre of mass energy only two of the variables are independent.

1.4 The Structure of the Proton

In the Standard Model the proton is not an elementary particle but consists of quarks and gluons. For the treatment of electron proton scattering this substructure has to be modelled appropriately. Deep inelastic scattering experiments like those performed at HERA deliver insights into the structure of the proton and the dynamics between its constituents.

1.4.1 Structure Functions

Commonly the proton's structure is described by a set of *structure functions*. Both the NC and the CC cross sections can be expressed in terms of these structure functions. The NC cross section contains terms for γ exchange, Z exchange and γZ interference. The propagator terms for Z exchange are proportional to $1/(Q^2 + M_Z^2)^2$, which for $Q^2 \ll M_Z^2$ leads to a suppression of Z exchange and γZ interference with respect to γ exchange. In the regime of medium and low Q^2 pure γ exchange can be assumed and only the structure function $F_2^p(x, Q^2)$ enters the calculation of the cross section:

$$\frac{d^2\sigma}{dxdQ^2} = \frac{2\pi\alpha}{xQ^4} F_2^p \left(1 + (1-y)^2\right).$$

1.4.2 Quark Parton Model

If the momentum of the proton is large, i.e. $p_p \gg m_p$ the proton can can approximated as a parallel stream of free quarks. In this *quark parton model* (QPM) the scattering process is identified as the scattering of the electron from a single quark, whereas the other quarks are referred to as spectators, which form the *proton remnant*. In this simplified model the structure function F_2^p can be written as

$$F_2^p = x \sum_q c_q^2 \left(f_q^p(x, Q^2) + f_{\bar{q}}^p(x, Q^2) \right).$$

Here c_q is the charge of the quark and the functions f_q^p and $f_{\bar{q}}^p$ are the quark and antiquark densities in the proton. If it is assumed that the proton consists only of the three *valence quarks* the structure function F_2^p should only depend on x. This behaviour is known as *Bjorken scaling*. The detailed measurements of NC DIS however have shown that F_2^p does depend as well on Q^2 and this is known as *scaling violation*. Gluons and gluon induced quark-antiquark pairs give rise to this behaviour. Figure 1.2 shows the dependence of F_2^p on x and Q^2 as measured by H1 in [3]. The effect of scaling violation is clearly visible.

1.4.3 Factorisation and Parton Density Functions

The *factorisation theorem* gives a theoretical foundation of the definition of parton densities. Here the scattering process is split into the interaction of high energy partons, which is referred to as the *hard subprocess* and which can be modelled by perturbative QCD (pQCD) and a long distance part which is not accessible within pQCD. The short distance part is described by *coefficient functions* C_2^i which are calculable within pQCD. The long distance part is described by *parton density functions* (PDFs) $f_i^p(\xi)$, which give the probability of finding a parton with a fraction ξ of the proton's longitudinal momentum. The structure function can be written as a convolution of these terms:

$$F_2^p(x, Q^2) = \sum_{i \in q, \bar{q}, g} \int_x^1 d\xi C_2^i \left(\frac{x}{\xi}, \frac{Q^2}{\mu^2}, \frac{\mu_f^2}{\mu^2}, \alpha_s(\mu) \right) f_i^p(\xi, \mu_f, \mu).$$

Here μ is the QCD renormalisation scale. An additional factorisation scale μ_f is introduced, which defines the boundary between the perturbative regime and the non-perturbative regime. The value of this scale depends on the factorisation scheme used. However within a given factorisation scheme the PDFs are universal, i.e. they do not depend on the scattering process the proton is involved in. The concept of factorisation requires a hard scale in the scattering process. In the case of DIS this is provided by the high virtuality of the exchanged boson.The hard scale can be provided as well by a

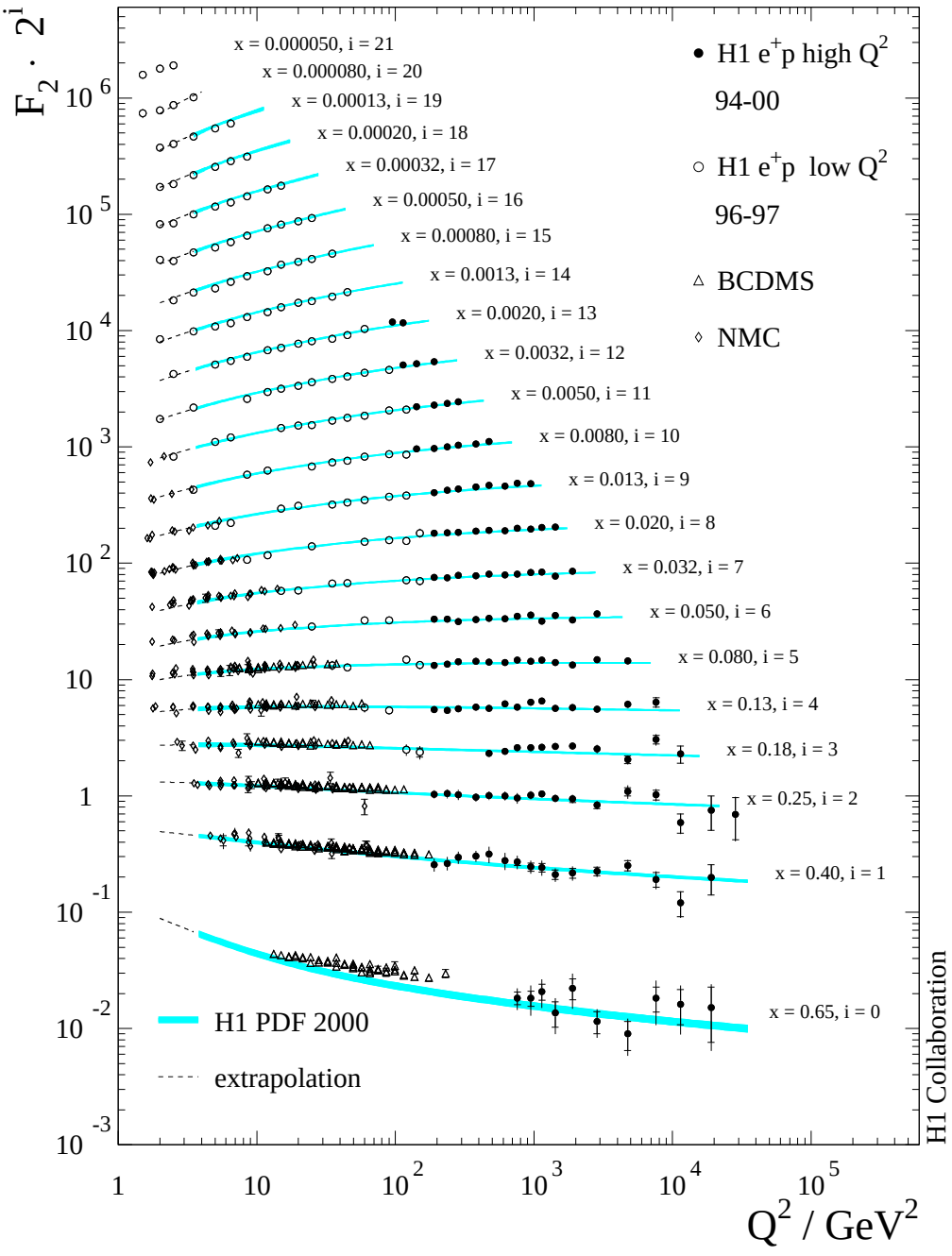

Figure 1.2: The structure function F_2^p as measured by H1 in [3].

high transverse momentum of the outgoing partons or the high mass of beauty and charm quarks, which is the case in this analysis, see section 1.6.

1.4.4 Parton Evolution Models

Using the factorisation theorem the inclusive DIS cross section factorises into the parton level cross section, which can be calculated in pQCD and the parton density functions for the parton that takes part in the hard interaction. Symbolically this can be represented as

$$\sigma_{ep} = \sum_{i=q,\bar{q},g} \hat{\sigma}_{ei} \otimes f_i^p(\mu_f).$$

Both the parton level cross section and the PDFs depend on the *factorisation scale* μ_f. However the measured cross section does not depend on this parameter. Hence it is possible to derive the μ_f dependence of the PDFs from the measured cross sections using the parton level cross section calculated in pQCD. The PDFs can be extracted using *parton evolution equations*. Due to the complexity of these calculations *parton evolution models* are used, which are valid only in certain regions of phase space. In practise a reference frame is chosen in which the contributions to $\hat{\sigma}$ take the form of a *parton ladder* built by n parton emissions of partons with transverse momentum $k_{t,i}$ and longitudinal momentum x_i, with $x_i > x_{i+1}$. The principle is illustrated in figure 1.3. The calculation simplifies, if a certain *kinematical ordering* of these emissions is assumed. The most common models are presented in the following:

DGLAP: In this ansatz, proposed by Dokshitzer, Gribov, Lipatov, Altarelli and Parisi [23, 6, 15], a strong ordering of the transverse momenta $k_{t,i} \ll k_{t,i+1}$ is assumed. In addition it is required that the longitudinal momentum of the parton xp_p, p_p being the momentum of the proton, is much less than the transverse momentum, which is the case for not too small values of x.

CCFM: This model by Ciafaloni, Catani, Fiorani and Marchesini [14, 11, 29] assumes an angular ordering of the emissions. With this model the description of the low x region is expected to be more accurate than with DGLAP. CCFM allows for an *intrinsic* tranverse momentum of the gluon starting the gluon ladder.

1.5 Photoproduction

The regime of $Q^2 < 1\ \mathrm{GeV}^2$ is referred to as *photoproduction*. The propagator of the exchanged boson enters the cross section as a factor of $1/(Q^2 + M^2)^2$, where M is the

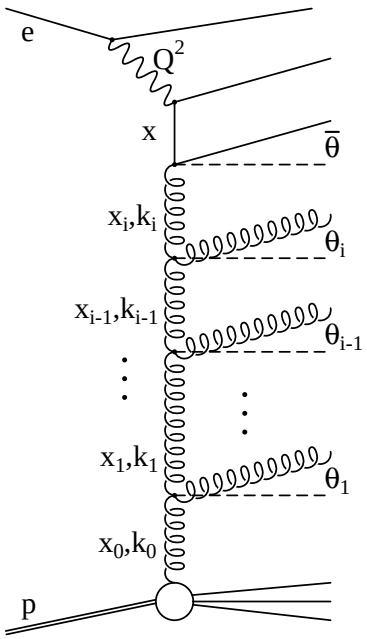

Figure 1.3: Parton ladder

mass of the exchanged boson. As the photon is a massless particle, γ exchange dominates the total cross section at low Q^2 by several orders of magnitude compared to Z^0 and $W^{\pm}$ exchange. Furthermore the exchanged photon has a very small virtuality and can be treated as a *quasi real* particle. In photoproduction the electron is scattered under a very low angle, corresponding to $\vartheta \lesssim 180°$ in the H1 coordinate system, which will be defined in section 2. Here the definition of y in equation 1.2 simplifies to $y = 1 - E'_e/E_e$. In the limit of $Q^2 \to 0$, with s and y being finite, equation 1.3 implies $x \to 0$.

1.5.1 Weizsäcker-Williams Approximation

In photoproduction the exchanged photon is quasi real. This allows the factorisation of the electron proton scattering process into the emission of a photon from the electron and the scattering of a real photon from the proton. The electron proton scattering differential cross section factorises to

$$\frac{d^2\sigma_{ep}(y,Q^2)}{dxdQ^2} = P_{\gamma e}(y,Q^2) \cdot \sigma_{\gamma p}(y),$$

where $\sigma_{\gamma p}(y)$ is the cross section for the scattering of a real photon with energy yE_e from a proton and $P_{\gamma e}(y,Q^2)$ is the probability for the electron to emit a photon with virtuality Q^2 and momentum fraction y.

1.5.2 Photon Structure

Although the photon is an elementary particle, it can fluctuate into a hadronic state, i.e. a pair of quarks. This can be modelled similarly to the partonic structure of the proton and parton density functions for the photon can be defined and measured. If a photon fluctuates into a hadronic state and a parton out of this state takes part in the hard interaction this is referred to as a *resolved process*. The properties of these processes and their importance for forward beauty production will be discussed in section 1.6.1.

1.6 Production of Beauty Quarks

Due to the higher mass of the beauty and charm quarks compared to the *light flavours* up, down and strange, these are often referred to as *heavy flavours*[2]. The mass of the charm quark is slightly higher than the QCD scale $\Lambda_{\mathrm{QCD}} \approx 0.2\,\mathrm{GeV}$, whereas the mass of the beauty quarks is considerably higher. This means that both flavours are expected to provide a hard scale μ, which allows pQCD to be applied. This is particularly useful in the photoproduction regime, where no natural hard scale like Q^2 is provided. Figure 1.4 shows the dependence of the strong coupling α_s on the scale μ [17].

α_s is considerably smaller if it is evaluated at the beauty mass than at the charm mass. This leads to the assumption that beauty production should be described better by pQCD than charm production. However it was found in measurements at HERA, LEP and the Tevatron, that charm production is reasonably well described by pQCD, while the measurements of beauty production cross sections are all above the prediction by pQCD. The most recent measurements performed at HERA, performed both in the regime of photoproduction and deep inelastic scattering are shown in figure 1.5 [5].

The total beauty production rate is much lower than the rate for charm and light flavours, with $\sigma_{uds} : \sigma_c : \sigma_b = 2000 : 200 : 1$. The main reason for the suppression of beauty production with respect to charm production is the available phase space. Both in direct and resolved processes a gluon from the proton takes part in the hard subprocess. The centre of mass energy of the initial parton pair has to be high enough to allow production of charm or beauty respectively. For the direct production process this translates into the condition

$$x_g > \frac{m_q^2}{yE_eE_p}.$$

This condition yields a minimal $x_g \approx 10^{-4}$ for charm and $x_g \approx 10^{-3}$ for beauty. Figure 1.6 shows the gluon density in the proton as measured in photoproduction of D^* mesons

[2] $t\bar{t}$ production is not possible at HERA, because the mass of the top quark of $m_t \approx 174\,\mathrm{GeV}$ is higher than half of the centre of mass energy $\sqrt{s}/2 \approx 160\,\mathrm{GeV}$.

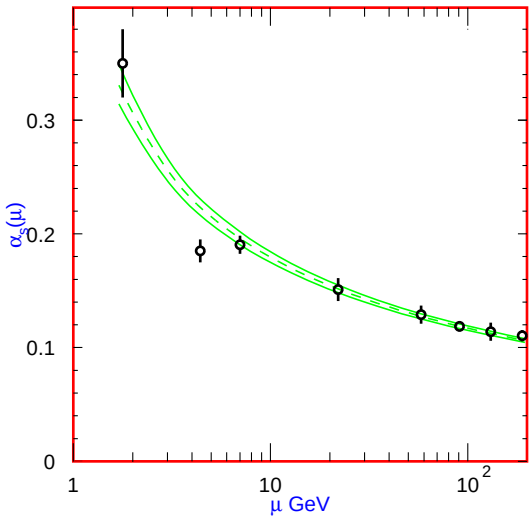

Figure 1.4: The dependence of α_s on the hard scale μ. The data are obtained from measurements of μ, τ and Υ decays, deep inelastic scattering and event shapes in e^+e^- collisions.

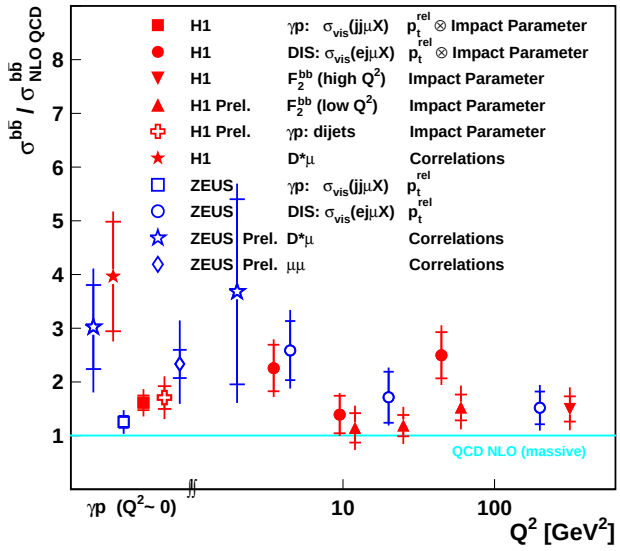

Figure 1.5: Summary of recent measurements of beauty cross section measurements at HERA.

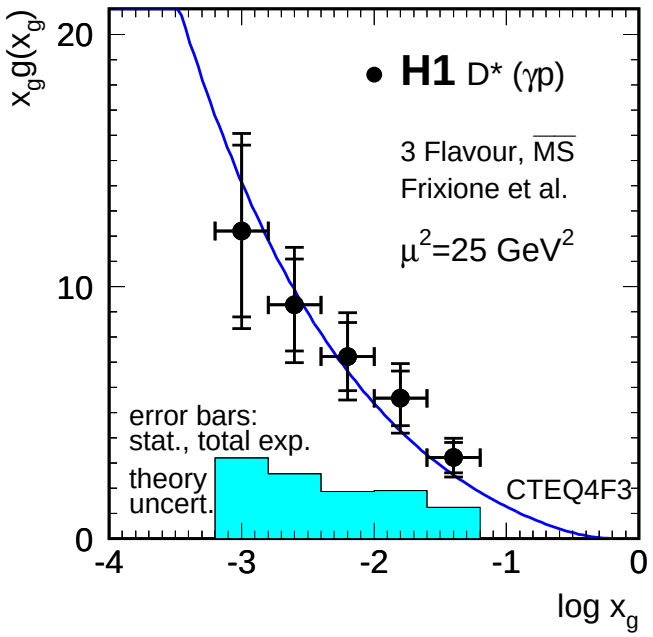

Figure 1.6: The gluon density in the proton as measured in photoproduction of D^* mesons by H1.

by H1 in [2]. The distribution falls steeply between the charm threshold at $x_g \approx 10^{-4}$ and the beauty threshold at $x_g \approx 10^{-3}$. This means that the phase space region with high gluon density is not accessible for beauty production at HERA, and beauty production is suppressed with respect to charm production.

1.6.1 Production Processes for Heavy Quarks

As mentioned in section 1.5.2 the photon can enter the hard interaction directly or it can fluctuate into a hadronic state before the interaction. These *direct* and *resolved* processes are important in in both charm and beauty production. However as mentioned before, beauty production is heavily suppressed with respect to charm production.

Boson-Gluon-Fusion

The *direct* production process, where the photon directly interacts with a gluon from the proton via a quark pair, is referred to as *Photon-gluon-fusion*. A Feynman graph for this process is shown in figure 1.7 a). The photon and the gluon couple via a pair of heavy quarks.

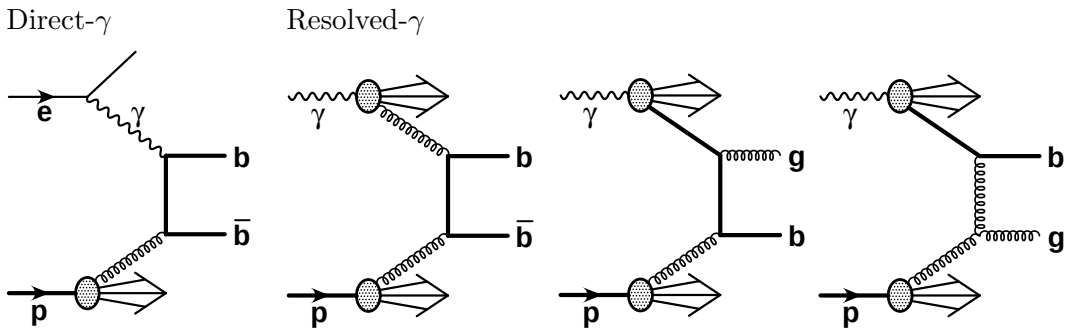

a) γg-fusion b) gg-fusion c) b-excitation d) b-excitation

Figure 1.7: Feynman diagrams for direct and resolved beauty production processes

Resolved and Excitation Processes

In resolved processes the photon fluctuates into a hadronic system, with one constituent of this system interacting with a gluon from the proton in the hard interaction. If the parton coming from the photon side is a gluon this process is referred to as *gluon-gluon-fusion* . A Feynman graph for this process is shown in figure 1.7 b). The photon can as well fluctuate into a pair of heavy quarks and if one of these heavy quarks enters the hard interaction the process is referred to as charm- or beauty-*excitation*, as shown in figures 1.7 c) and d). In resolved and excitation processes the remaining partons from the photon form the seed of the *photon remnant*. In this thesis the term *resolved* refers to all resolved photon processe except excitation.

1.6.2 Forward Beauty Production

So far the beauty measurements at H1 as shown in figure 1.5 only covered the central region, i.e. with $\vartheta_b \gtrsim 25°$. However the very forward[3] direction exhibits a different kinematic region. Figure 1.8 shows the distribution of the azimuthal angle of the muon jet[4], as predicted by the Pythia Monte Carlo generator. In the forward region with $\vartheta < 35°$ the cross section is much higher than in the central region. This is mainly due to the large Lorentz boost from the large momentum of the incoming proton.

In resolved processes only a fraction x_γ of the photon's momentum enters the hard interaction. This results in a bigger boost of the final state into the direction of the outgoing proton compared to direct production. Figure 1.8 shows, that the relative contribution of

[3]At the HERA-Experiments H1 and ZEUS *forward* denotes the direction of the outgoing proton corresponding to $\vartheta = 0°$.

[4]The semimuonic decay of beauty hadrons will be described in section 1.8. The formation of jets will be described in section 1.10.

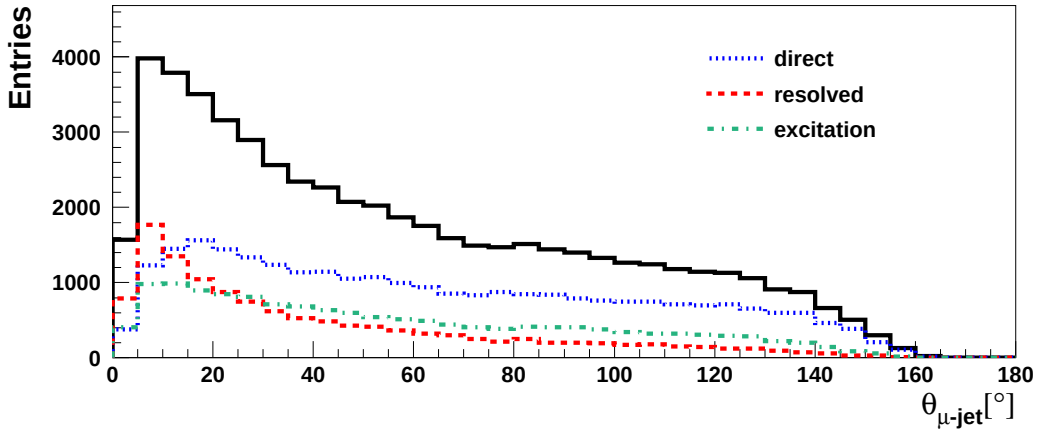

Figure 1.8: Azimuthal angle of the muon jet as predicted by the Pythia Monte Carlo generator. The solid line shows the sum of all processes, while the dashed lines show the contribution of direct, resolved and excitation processes.

resolved and excitation processes is much higher in the forward region than in the central region.

1.7 Fragmentation

In the hard interaction quarks and gluons are produced. However free quarks and gluons have never been observed experimentally. This is a consequence of *Confinement*, as predicted by QCD. With increasing distance between the partons the potential energy between them increases until new partons are formed which recombine with the initially produced partons and produce colourless hadrons. This process is referred to as *fragmentation* or *hadronisation*. This process is not entirely calculable in perturbative QCD and therefore the fragmentation is split into a perturbative part and a non-perturbative part. These processes are modelled in the fragmentation routines of Monte Carlo generators, which are described in section 1.9.

1.7.1 Parton Showers

The perturbatively calculable part of the fragmentation is in theory modelled by parton evolution equations. However these cannot be apllied on an event by an event base as it is needed by Monte Carlo generators. The full parton evolution is approximated by *partons showers*. Beginning with a parton from the proton, parton splittings are performed. The starting parton evolves to increasing negative virtuality until it enters the hard subprocess. These emissions are referred *initial state* parton showers. The possibility for such a

splitting depends on the splitting function and the virtuality of the parton. Any outgoing parton with positive virtuality can undergo *final state* parton showers. This cascade is stopped when the virtuality of the parton reaches values of approximately 1 GeV. Here pQCD calculations are not applicable any more and phenomenological models have to be applied.

1.7.2 Hadronisation Models

So far no complete theoretical model for the formation of hadrons in the fragmentation process is available. At large distances between the initial partons the strong coupling constant α_s becomes large and perturbative methods fail. Therefore phenomenological models are used which give a good description of the final state. These models are assumed to beindependent of the production mechanism of the partons. This was recently tested by ZEUS [13]. The most precise measurements of the parameters of the hadronisation models come from the experiments at the e^+e^- collider LEP [17]. A set of *fragmentation functions* $D_i^h(z)$ describes the probability of the parton i to form a hadron h, carrying a fraction z of the longitudinal momentum of the incident parton. The additional quarks needed to form mesons are taken from $q\bar{q}$ pairs from the vacuum. The remaining quark of the pair continues hadronisation For the fragmentation into a baryon a set of $qq\bar{q}\bar{q}$ has to be created. The splitting processes continue until all energy is used up.

The model used in this analysis for the fragmentaion of beauty and charm is the *independent fragmentation*. Here every outgoing parton hadronises independently. Several parametrisations for the fragmentation functions are known, which produce similar results for heavy flavour production. In this analysis the *Peterson parametrisation* is used, which models the the fragmentation like

$$D_i^h(z) \sim \frac{1}{z}\left(1 - \frac{1}{z} - \frac{\epsilon}{1-z}\right)^{-2}.$$

Here ϵ is a parameter which has to obtained experimentally. In this analysis $\epsilon_c = 0.058$ for charm and $\epsilon_b = 0.0069$ for beauty are used.

Another model is the *Lund string fragmentation*, which is used in this analysis for the fragmentation of light flavours. Here a colour string is formed between the quarks. As the QCD potential between colour charges rises strongly with the distance[5], the energy stored in the string is used to produce a $q\bar{q}$ pair and the string breaks up. This process continues until the strings do not provide enough energy for further production of $q\bar{q}$ pairs.

For the production of heavy flavour hadrons these models produce comparable results.

[5]The shape of this potential for large distances is only approximately known. It is usually modelled like $V(r) \backsim r$ or $V(r) \backsim \log(r)$.

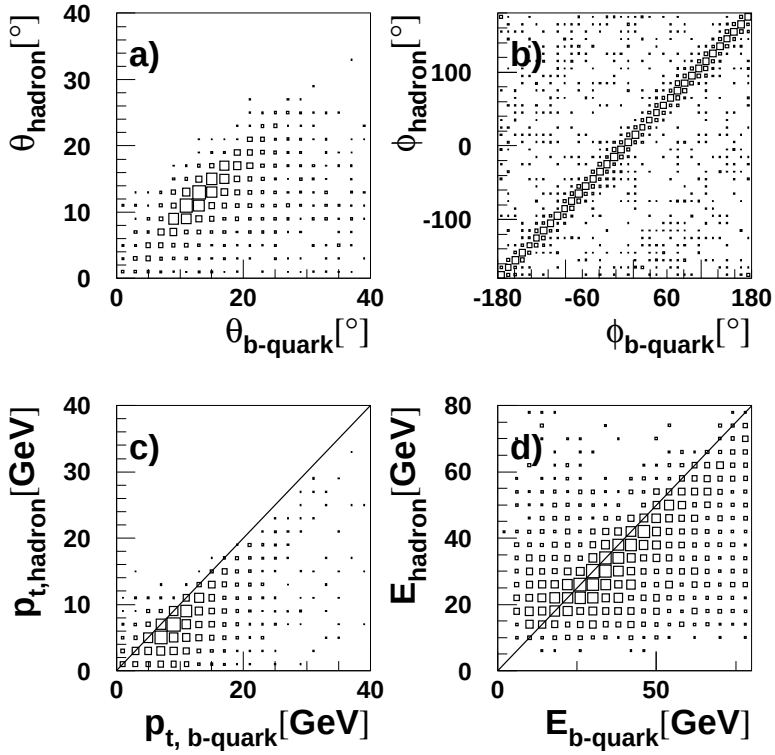

Figure 1.9: Correlation between the beauty quark and the associated beauty hadron, as predicted by the Pythia Monte Carlo simulation.

1.7.3 Beauty Hadrons

After the fragmentation the beauty quarks end up in beauty hadrons. These are significantly heavier than charmed hadrons and hadrons which are made up of light quarks. Beauty mesons usually have masses around 5.3 GeV. These have to be compared with the masses of charmed mesons around 1.8 GeV and of light mesons like the pion with a mass of $m_{\pi^0} = 0.135$ GeV.

Figure 1.9 shows the correlation between the incident beauty quark and the beauty hadron produced in the fragmentation. These events were generated using the Pythia Monte Carlo simulation and had to pass the final event selection of this analysis. The plots show good correlations between the quark and the hadron.

1.8 Semileptonic Decay of Heavy Hadrons

Heavy flavour hadrons are short lived and never observed directly. Only the decay products are visible in the detector. The weak decay of a beauty quark via a $W^{\pm}$ boson can result

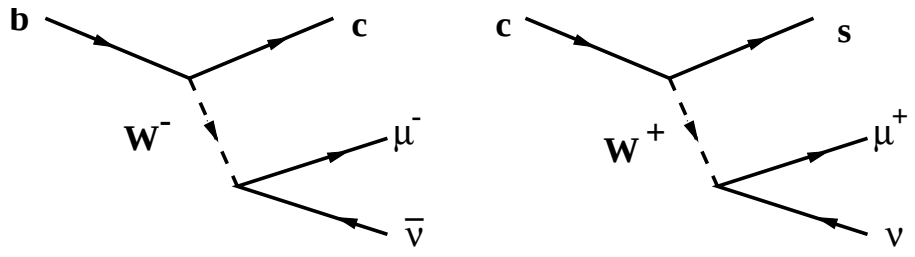

Figure 1.10: Semimuonic decay of beauty and charm quarks

either in a charm or an up quark. The latter is suppressed by the CKM matrix, with $0.039 < V_{cb} < 0.044$ and $0.0029 < V_{ub} < 0.0045$. The small value of V_{cb} is the reason for the long life time of beauty hadrons compared to charm hadrons [16]. The virtual $W^{\pm}$ decays to all kinematically allowed pairs of of up and down type fermions.

The produced fermions can either be a pair of up and down type quarks or a lepton and the corresponding antineutrino. The latter case is referred to as the *semileptonic* decay, which has a branching ratio ca. 10% for each lepton type [16]. In the case of semileptonic charm decays only electrons and muons can be produced. The high mass of beauty hadrons enables as well semileptonic tau production. In this analysis the semimuonic channel is chosen as it will offer the clearest experimental signature. This process is illustrated in figure 1.10 both for beauty and charm decay. In the case of beauty decay both the prompt decay, where the muon originates directly from the beauty quark and the cascade decay, where the muon originates from a charm quark resulting from the beauty decay are possible. This results in a combined branching ratio for $b \to \mu X$ of 20%.

1.9 Monte Carlo Generators

Monte Carlo programs are used to simulate the ep scattering process on an event by event basis. Starting from the incoming particles, the reaction is modelled up to the formation of stable hadrons. For the case of boson gluon fusion the method is sketched in figure 1.11. The hard interaction described by a matrix element (ME) is modelled in leading order[6]. As described in section 1.7.1 gluon emissions in the initial and final state are simulated by evolution equations and parton showers (PS). These partons together with the partons produced in the hard interaction enter the hadronisation step. Here the JETSET program [31] is used to perform the hadronisation either in the framework of independent fragmentation or Lund fragmentation for heavy flavours.

[6]A next to leading order implementation (MC@NLO) exists for $p\bar{p}$ collisions [22, 21] and is currently being adapted for HERA physics.

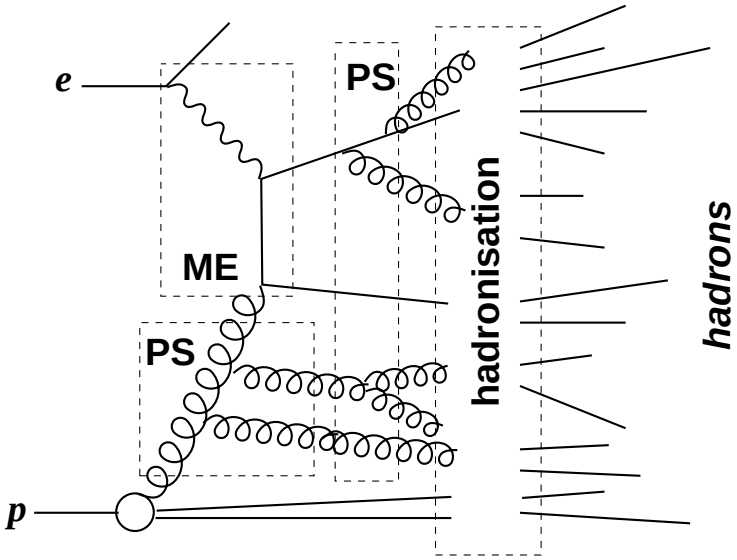

Figure 1.11: Schematic view of the Monte Carlo event generation

The hard subprocess can be modelled by different event generators, each specialised on certain physics processes, like photoproduction, DIS or diffraction. For photoproduction of heavy flavours the most commonly used generators are *Pythia* [31] and *Cascade* [27]. In Pythia the on-shell DGLAP parton evolution is implemented. Treatment of the photon structure allows the inclusion of resolved processes. Cascade uses the CCFM evolution equation, unintegrated gluon densities and off-shell matrix elements. Resolved processes are not explicitly implemented, but are partially contained.

1.10 Jet Formation

After the fragmentation hadrons are formed, which decay into stable particles. Due to the boost of the incident hadron these particles form a collimated jet. A jet algorithm is used to match particles in the final state of the event to a jet. This algorithm will be described in section 4.2.2. The jet axis approximates the direction of flight of the beauty hadron, which in turn approximates the direction of flight of the beauty quark, as shown in figure 1.9. Figure 1.12 shows the correlation between the muon jet and the associated beauty hadron. The jet algorithm is applied to the particles generated by the Pythia Monte Carlo generator. The events in this plot have to pass the final selection of this analysis. Figure 1.12 b) shows a good correlation between the φ coordinates of the jet and the hadron. However there are two bands visible corresponding to an angular difference of the jet and the associated hadron of $\approx 180°$. These bands are an artefact of the matching algorithm

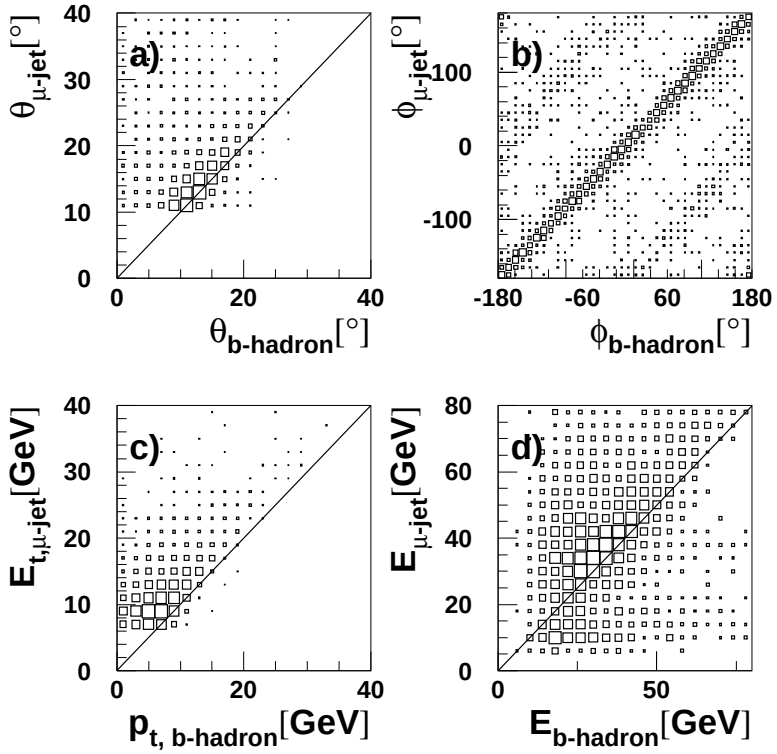

Figure 1.12: Correlation between the muon jet and the associated beauty hadron

between the jet and the beauty hadron. For the identified muon jet the beauty hadron is searched for which is closest in the $\eta\varphi$ plane[7] . In resolved processes however the muon jet may originate from a gluon which hadronised into a light hadron, whereas the beauty quark entering the hard subprocess from the photons's side is located opposite in φ. In these cases the beauty quark gets identified by the matching algorithm instead of the gluon which is the physical origin of the jet.

[7] η is the pseudorapidity, defined as $\eta = -\ln(\tan(\vartheta/2))$. The benefit of this parametrisation is that $\Delta\eta = \eta_1 - \eta_2$ is Lorentz invariant with respect to a boost along the z axis.

Chapter 2

The H1 Experiment

In the H1 experiment electron-proton collisions are studied. The beams of electrons[1] and protons are delivered by the HERA accelerator. The collisions are investigated using the H1 Detector. This chapter will give a brief overview over the HERA machine and the H1 detector.

2.1 The HERA Accelerator

HERA[2] is the only accelerator in the world, where protons collide with electrons. The HERA accelerator is situated in Hamburg Bahrenfeld and operated by DESY. Protons and electrons are accelerated and stored in two storage rings, which intersect at the interaction regions of the experiments H1 and ZEUS. These rings are located in an underground ring tunnel with a circumference of 6.3 km. The ring consists of four 90° arcs and four straight sections.

In a chain of preaccelerators the beam particles are stored and accelerated until they are transferred into the main HERA ring with an energy of 12 GeV for the electrons and 40 GeV for the protons. The beams are ramped up to their design energy, which is 920 GeV for the protons[3] and 27.5 GeV for the electrons. The energy of the proton beam is limited by the magnetic field of the dipole magnets in the arc sections. These magnets are superconducting and produce a magnetic field of 4.68T. The electron energy is limited by the energy loss of the electron beam due to synchrotron radiation, which scales proportional to E^4. Once the beams are at their design energy, collisions are established at the interaction points of H1 and ZEUS. The centre of mass energy here is $\sqrt{s} \approx 319\,\text{GeV}$. The layout of the accelerators at DESY and the HERA accelerator are shown in figure

[1] Hereafter the term *electrons* will be used both for electrons and positrons.
[2] HERA stands for Hadronen-Elektronen-Ring-Anlage.
[3] Until 1998 the proton energy was limited to 820 GeV.

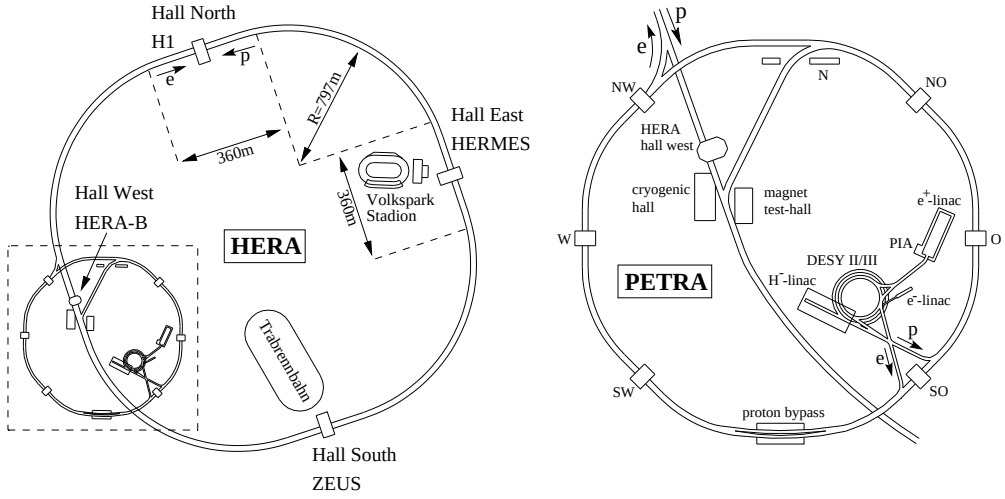

Figure 2.1: Layout of the HERA accelerator and the DESY accelerator chain

2.1.

On each straight section of HERA an experimental hall is situated. Two halls house the colliding beam experiments H1 and ZEUS. The others are used by the fixed target experiments HERMES and HERA-B. HERMES only uses the electron beam of the HERA accelerator for collisions with a gaseous fixed target. This experiment uses longitudinally polarised electrons[4]. The gaseous target as well can be spin polarised, enabling HERMES to measure the spin structure of the proton. HERA-B placed wire targets in the halo of the proton beam. The goal of this experiment was to measure CP violation in the beauty sector. HERA-B finished data taking in 2003.

In order to achieve a high luminosity the particles are not stored in continuous beams but are compressed in bunches. Up to $\approx$ 200 bunches are stored in each beam. The lifetime of the proton beam is of the order of 100h, the lifetime of the electron beam is about 10h. This limits the duration of a luminosity fill to about 16h. At the interaction points at H1 and ZEUS the bunches collide with a frequency of 10.4MHz, corresponding to a separation in time of 96ns. In the running period of the year 2000, in which the data of this analysis was taken, the peak luminosity was $17.9 \cdot 10^{30}\,\mathrm{cm^2 s^{-1}}$, the average luminosity was $6.47 \cdot 10^{30}\,\mathrm{cm^2 s^{-1}}$.

[4]Electrons in a storage ring become transversely polarised by the Sokolov-Ternov effect. Hermes uses spin rotators to obtain longitudinally polarised electrons. These spin rotators are installed on both sides of the experiment and flip the spin from transverse to longitudinal and back. In 2001 spin rotators were installed for H1 and ZEUS.

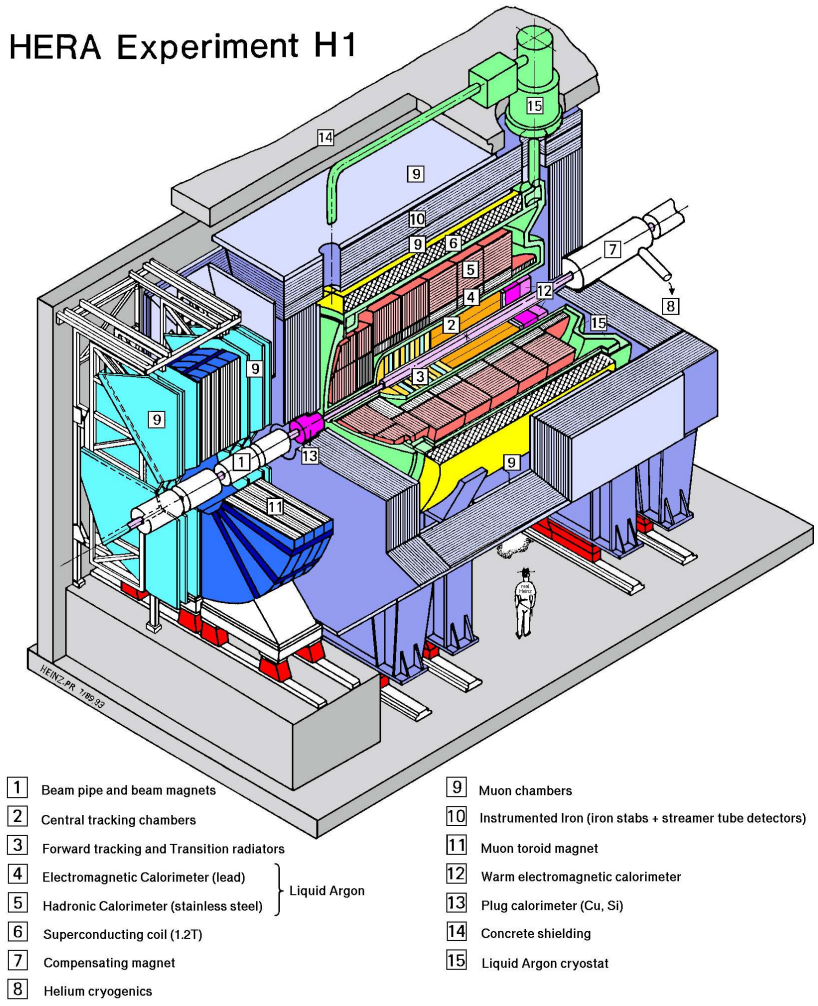

Figure 2.2: Drawing of the H1 detector. The direction of the view is from inside the HERA ring.

2.2 Layout of the H1 Detector

The H1 detector is located in the North Hall of the HERA accelerator. It consists of central tracking chambers, calorimeter systems, a superconducting coil to produce a magnetic field and an outer muon system. The layout of the H1 detector is sketched in figure 2.2. The coordinate system that will be used throughout this analysis can be defined here: The z coordinate points in the direction of the outgoing proton beam, the x coordinate point into the direction of the centre of the HERA ring and the y coordinate point upwards. A particular feature of the H1 detector is the very pronounced asymmetry of the detector along the z axis. This asymmetry is due to the large difference of the beam energies resulting in a large boost of the final state into the direction of the outgoing proton

beam. A detailed description of the complete detector can be found in [1]. The individual components of the detector and the system of data acquisition relevant for this analysis will be described in the next sections.

2.3 Inner Tracking Systems

Closest to the interaction point silicon trackers are located, followed by drift chambers and proportional chambers. These trackers are used to reconstruct the tracks which are formed by charged particles traversing the tracker volume. By extrapolation of the tracks to the beam line the space point of the *ep* collision, the *primary vertex*, can be identified. The magnetic field of $B = 1.15\text{T}$ produced by the superconducting solenoid located between the LAr calorimeter and the CMD bends the tracks and provides a momentum measurement. The asymmetry of the H1 detector is reflected in the design of the tracking system. The *Central Tracking Detector* (CTD) covers the polar angular region $15^\circ \lesssim \vartheta \lesssim 165^\circ$, the *Forward Tracking Detector* (FTD) covers $5^\circ \lesssim \vartheta \lesssim 25^\circ$. In the backward region the *Backward Silicon Tracker* (BST) and the *Backward Drift Chamber* (BDC) provide additional tracking information. The main component of the CTD is the two-component *Central Jet Chamber*. The measurement of the z and ϑ component of the tracks is improved by two additional drift chambers, the *Central Inner* and *Central Outer z Chamber* (CIZ and COZ). Two *Multi Wire Proportional Chambers* (MWPC) are installed for trigger purposes. The *Central Silicon Tracker* allows for precise vertexing. In the forward direction the FTD allows reconstruction of forward tracks. An additional MWPC is integrated in the FTD for trigger purposes.

The layout of the central tracker is illustrated in figure 2.3. The components of the tracking system, which are of importance to this analysis, will be explained in the following.

2.3.1 Central Jet Chambers CJC

The main tracking tracking detector is the Central Jet Chamber (CJC). It is separated into two cylindrical chambers CJC1 and CJC2. The chambers cover the region $-122.5\,\text{cm} < z < 107.5\,\text{cm}$. This corresponds to an angular acceptance of $11^\circ \lesssim \vartheta \lesssim 170^\circ$ for CJC1 and $26^\circ \lesssim \vartheta \lesssim 155^\circ$ for CJC2. The anode sense wires and field shaping cathode wires run parallel to the beam line. They are grouped into into 30 planes for CJC1 and 60 planes for CJC2. Accounting for the non-zero Lorentz angle due to the magnetic field the planes are tilted by $\approx 30^\circ$ with respect to the radial direction. The spatial resolution in the transverse plane is $\approx 0.14\,\text{mm}$. This allows for a resolution of the transverse momentum of $\sigma(p_t)/p_t^2 \approx 0.5\%\,\text{GeV}^{-1}$. As the sense wires are read out at both ends, the z coordinate of the hit can be calculated by charge divison. The poor z resolution of $\approx 22\,\text{mm}$ is improved

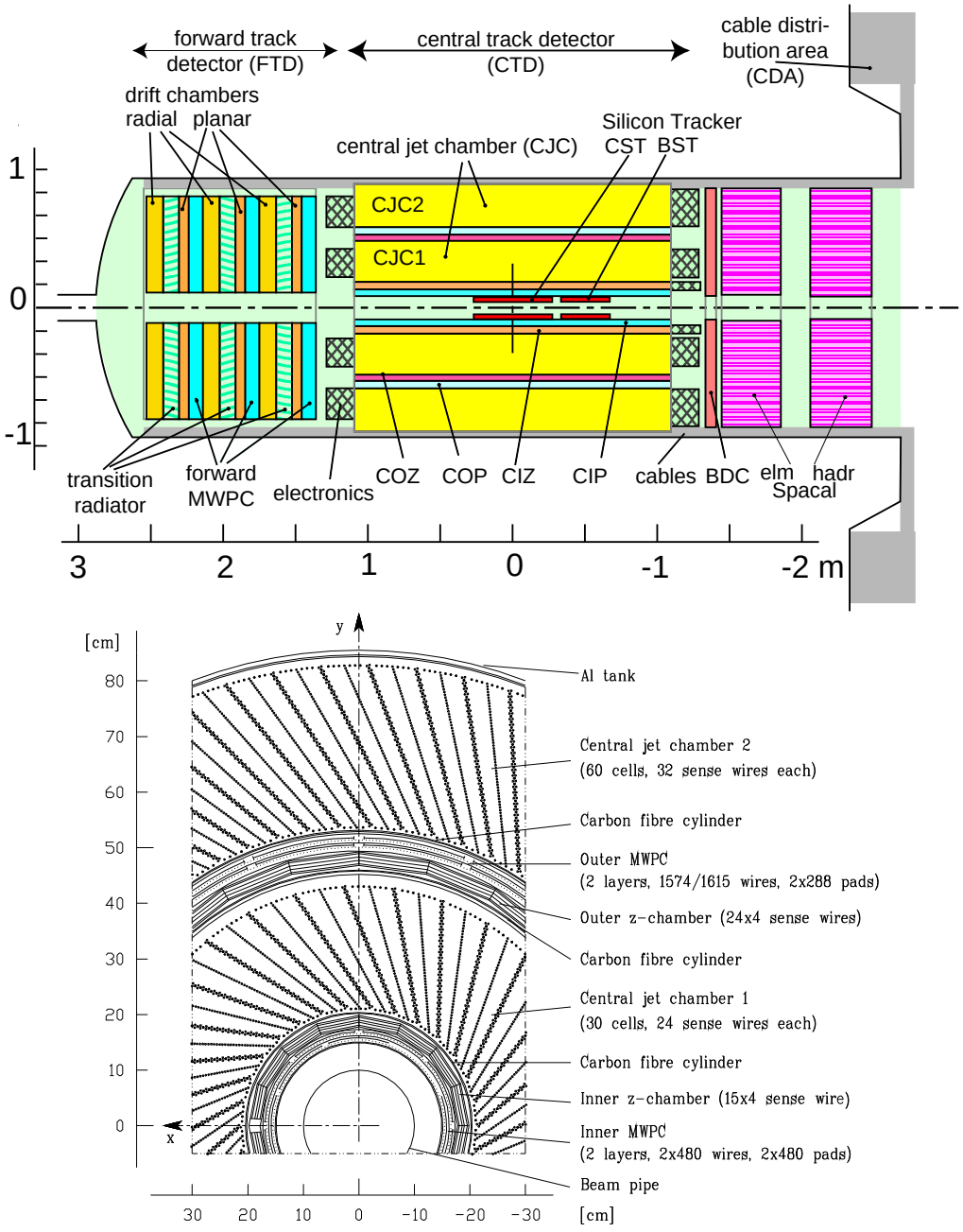

Figure 2.3: Sketch of the H1 tracking detectors. The upper drawing shows a cut through the tracker along the z axis. The lower drawing shows a transverse cut through the CTD. The CST is not shown in the transverse view.

in the track reconstruction software with information of the z-chambers, which have an intrinsic resolution of ≈ 0.38 mm.

2.3.2 Forward Tracking Detector FTD

The FTD is structured into three *supermodules* arranged perpendicularly to the beam axis. Viewed from the interaction point each supermodule consists of three planar drift chambers, followed by a MWPC, a transition radiator and a radial drift chamber. These drift chambers provide three dimensional hit information.

2.3.3 Multi Wire Proportional Chambers MWPC

H1 operates three MWPC systems. In the forward region the *Forward Proportional Chamber* FPC, which is integrated in the FTD has six independent planes. CIP and COP are located in the barrel area of the Central Tracker and have two layers each. The MWPCs offer

- a fast timing signal which is more accurate than the time difference between two HERA bunch crossing of 96 ns.
- space points with a reasonable resolution for track reconstruction on the first trigger level.

2.4 Calorimeters

The calorimeters at H1 cover almost the full 4π solid angle. The most important calorimeter is the liquid argon calorimeter (LAr), which is used in this analysis to reconstruct the hadronic final state. The backward calorimeter SpaCal is mainly used to detect the scattered electron at low values of Q^2. The layout of the H1 calorimeters is sketched in figure 2.4.

2.4.1 Liquid Argon Calorimeter LAr

The LAr is the main calorimeter of the experiment. It encloses the tracking detectors in the central and forward region, with $4^\circ \lesssim \vartheta \lesssim 153^\circ$. The layout is shown in figure 2.5. The calorimeter is structured in cells of readout and absorber material, filled with liquid argon as active material. The calorimeter is separated into an electromagnetic and a hadronic part. The inner electromagnetic part has lead absorbers and is built with a very fine granularity. This structure is optimised for the detection of electrons and photons. The outer hadronic part uses stainless steel absorber plates. It has a higher granularity,

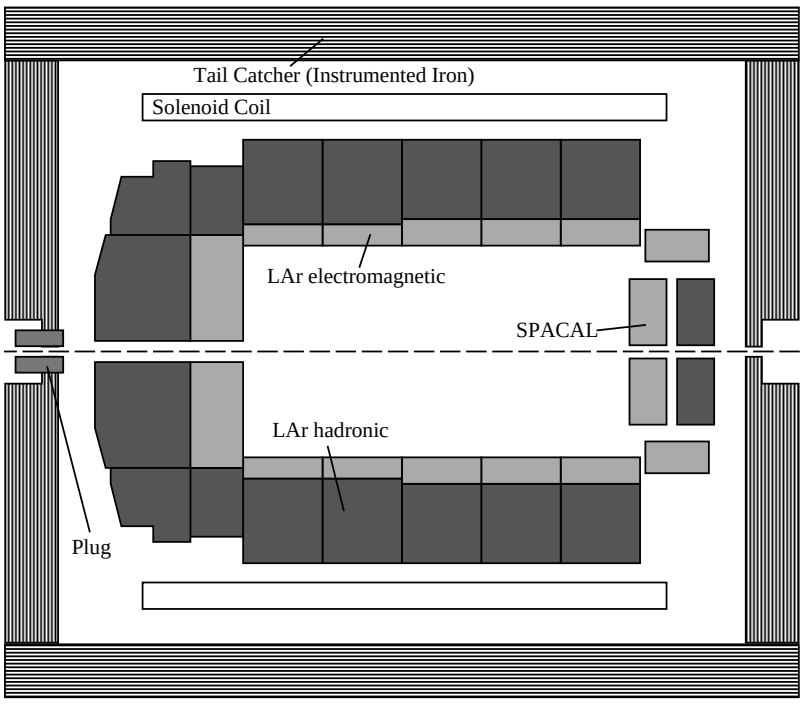

Figure 2.4: The H1 Calorimeters

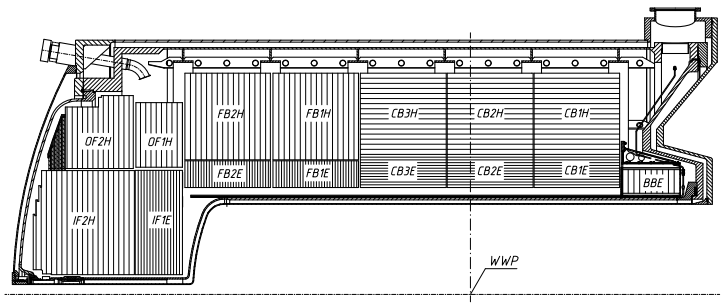

Figure 2.5: The Liquid Argon Calorimeter

because the energy deposit of hadrons is wider than for electrons and photons. The LAr is a non-compensating calorimeter, this means that the the signal response for an electromagnetically interacting particle is larger than for a hadron. This difference has to corrected in the reconstruction by a suitable weighting algorithm. The resolution of the calorimeter was measured in a test beam to be $\sigma(e)/E \approx 12\%/\sqrt{E\,[\,\mathrm{GeV}]}$ for electrons and $\sigma(e)/E \approx 50\%/\sqrt{E\,[\,\mathrm{GeV}]}$ in the hadronic part.

2.4.2 Spaghetti Calorimeter SpaCal

The SpaCal covers the backward region of the detector with $153^\circ \lesssim \vartheta \lesssim 178^\circ$. Its cells consist of scintillating fibres embedded in lead. The electromagnetic part consists of 1192 cells with a cross section of $4.5\,\mathrm{cm} \times 4.5\,\mathrm{cm}$. The energy resolution of the electromagnetic part is $\sigma(E)/E \approx 8\%/\sqrt{E\,[\,\mathrm{GeV}]}$. The hadronic part consists of 136 cells with a cross section of $11.93\,\mathrm{cm} \times 11.90\,\mathrm{cm}$ and provides an energy resolution of $\sigma(E)/E \approx 30\%/\sqrt{E\,[\,\mathrm{GeV}]}$. The SpaCal provides excellent spatial and time resolution. The latter can be used for trigger purposes as it can distinguish between particles arriving in the time window of the passing electron beam, which indicate a genuine *ep* event originating from the interaction point, and particles arriving in the time window of the passing proton beam, which can only be background.

2.5 Muon Detectors

Reliable muon detection is of great importance for many analyses in high energy physics. High energy muons traverse matter as minimum ionising particles and can pass through large stretches of matter. Therefore the muon systems form the outer layers of the H1 detector. The muon system at H1 consists of the *Central Muon Detector* which encloses the superconducting coil and serves as well as the return yoke for the magnetic field, and the *Forward Muon Detector*, which is equipped with a toroidal magnet, providing a momentum measurement independent of the FTD.

2.5.1 The Central Muon Detector CMD

The iron return yoke of the superconducting coil is instrumented with *limited streamer tubes*. The structure of the yoke is is an octagonal *barrel* closed by two flat *endcaps*, the Forward Endcap (FEC) and the Backward Endcap (BEC), see figure 2.2. The yoke is segmented in 10 layers of steel plates, each 7.5 cm thick. In between these plates 16 layers of limited streamer tubes are placed. Eight tubes are combined to form a *profile* and two profiles form a gas tight *element*. The surface of five of these elements is equipped with *strip* electrodes to measure the coordinate of a hit along the wire axis, while the remaining

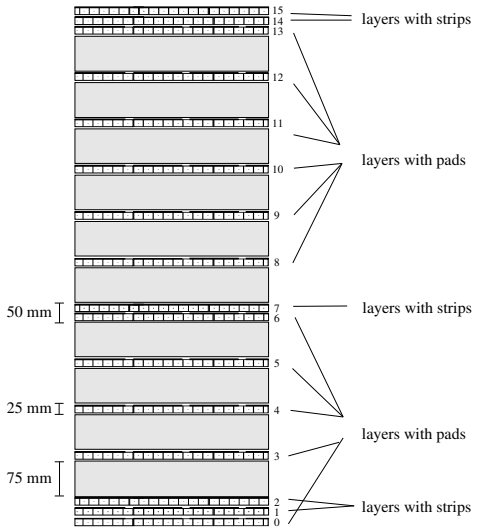

Figure 2.6: Cross section of the instrumented iron showing the position of the strip and pad layers.

11 elements are equipped with large rectangular *pad* electrodes providing a coarse energy measurement. Combining the information of several elements a three dimensional track reconstruction in the return yoke is possible. The instrumented detector volume covers the angular range of $6^\circ \lesssim \vartheta \lesssim 172^\circ$. The resolution provided by the wires of the streamer tubes is about $3-4\,\mathrm{mm}$, while the strips provide a resolution of $10-15\,\mathrm{mm}$. The resolution of the pads is about 10 cm. A cross section of the intrumented iron is shown in figure 2.6.

2.5.2 The Forward Muon Detector FMD

The FMD can measure high momentum muons in the angular range of $6^\circ \lesssim \vartheta \lesssim 18^\circ$. A side view of the FMD is shown in figure 2.7. The detector consists of a toroidal magnet sandwiched by three planes of drift chambers on either side. The toroidal magnet has an inner radius of 0.65 m and an outer radius of 2.9 m. The distance between the surfaces is 1.2 m. The magnet consists of eight solid iron modules which are assembled into half toroids, allowing easy access to the detector. The magnetic field varies from 1.75T at the inner radius to 1.5T at the outer radius.

Two planes of drift chambers on each side of the toroid measure the ϑ coordinate of a passing muon while in between those ϑ layers a φ layer is located, where the drift chambers are oriented perpendicularly to the drift chambers in the ϑ layers. The diameter of the layers ranges from 4 m for the first layers to 6 m for the last post-toroid layers. As the toroidal magnet bends tracks in the ϑ direction, the precise measurement of ϑ before and

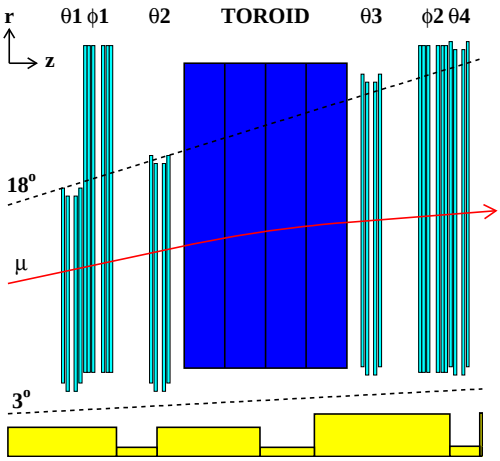

Figure 2.7: Side view of the FMD. Note that in this drawing the z axis points to the left as opposed to the normal H1 detector drawings.

after the toroid is crucial for the momentum measurement in the FMD.

The drift chamber layers are segmented into octants like the toroidal magnet. As an example a φ layer is shown in figure 2.8. The orientation of the drift chambers in the φ and ϑ planes is shown in figure 2.9. Each plane is equipped with a double layer of drift cells, which are staggered by half a cell width. This arrangement enables the resolution of left-right-ambiguities. The momentum resolution is limited by multiple scattering of the muon in the iron of the toroid. The minimum resolution is $\Delta p/p \approx 22\%$ at the lower momentum threshhold of 2.25 GeV. It deteriorates towards higher momenta.

2.6 Luminosity System

The luminosity is measured using the *Bethe-Heitler process*, $ep \to ep\gamma$. This process has a high cross section and is precisely calculable using QED. The luminosity system consists of an *electron tagger* at $z \approx -33\,\mathrm{m}$ and a *photon detector* at $z \approx -107\,\mathrm{m}$. The rate of the Bethe-Heitler process can be measured by counting coincidences of signals in the electron tagger and the photon detector. With the visible cross section of the Bethe-Heitler process corrected for the efficiency and detector acceptance of the two detectors the luminosity can be calculated. Reactions of the electron beam with residual gas can provide the same signal as the Bethe-Heitler process. The rate of this process can be measured using non colliding electron *pilot bunches*. This rate has to be subtracted from the measured rate of $e\gamma$ coincidences to calculate the luminosity. A more precise measurement is extracted for the offline analysis, where only the signals from the photon detector are used. In this

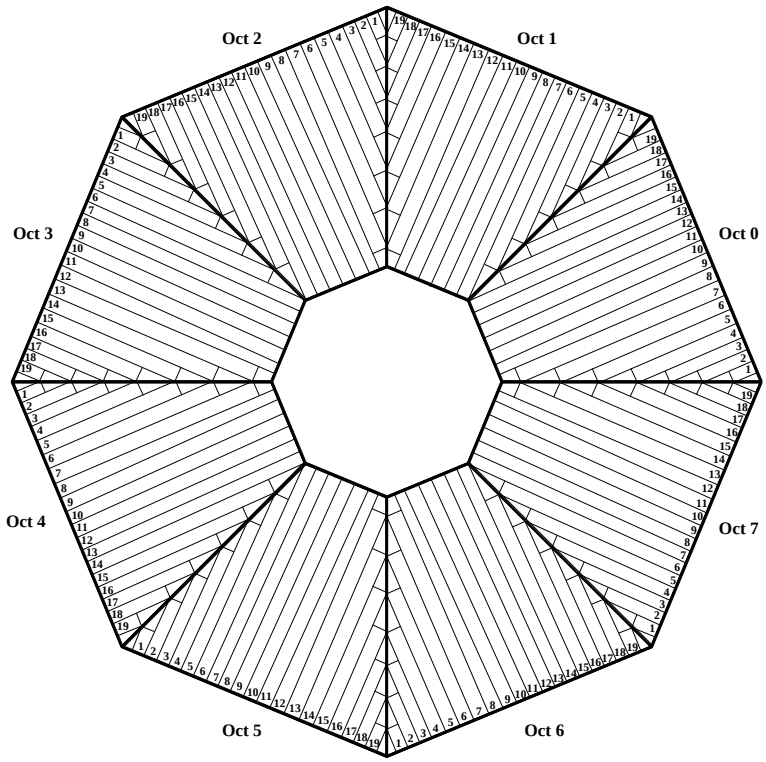

Figure 2.8: A φ layer of the FMD with the numbering of the octants

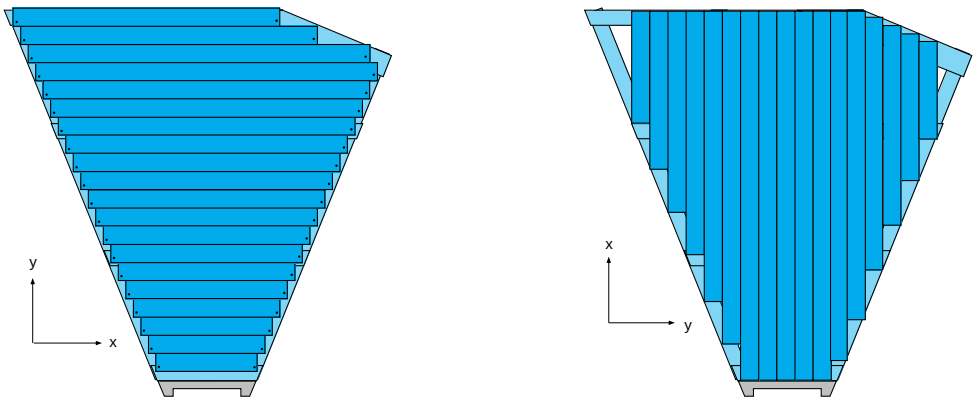

Figure 2.9: Orientation of the drift tubes in a ϑ octant (left) and in a φ octant (right). Here x and y define the local coordinate system for each octant.

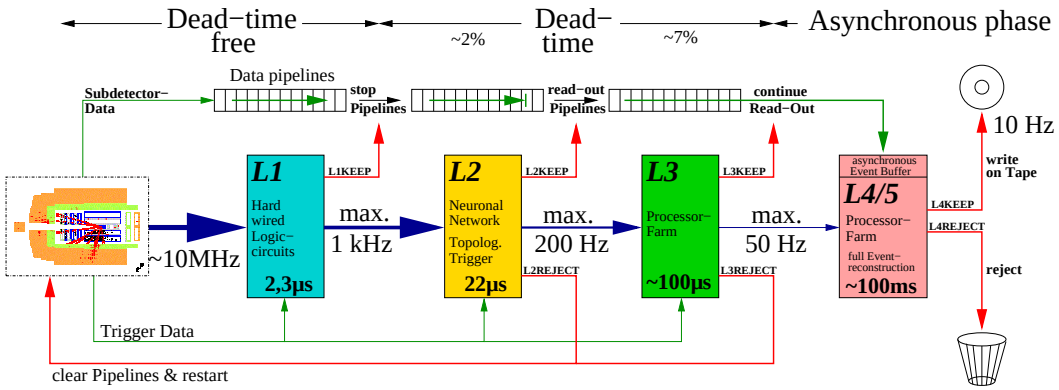

Figure 2.10: A schematic view of the H1 trigger system

case as well the photon rate from synchrotron radiation has to be subtracted using the electron pilot bunches.

2.7 Trigger System and Data Acquisition

The readout time of the total H1 detector is several orders of magnitude longer than the bunch spacing of 96 ns. The detector cannot detect events and be read out at the same time and therefore it is impossible to read out the detector at every bunch crossing where a genuine *ep* event might occur. Furthermore the expected rate of interesting *ep* events is several orders of magnitude lower than the rate of *background events*, which arise from collisions of beam particle with residual gas in the beam pipe and of off-orbit particles which collide with beam pipe or detector material. In addition the detector is exposed to a constant flux of muons originating from cosmic rays at a rate of ≈ 4 kHz. The task of identifying *ep* events while rejecting background events without reading out the complete detector is accomplished by the trigger system. The trigger system is organised in several levels labelled L1 to L5, which are illustrated in figure 2.10. Here the rates at every level and the decision time are shown. The trigger levels will be described in the following. Until the year 2005 L3 was not implemented and thus it will not be described here.

Level 1: The signals from the single subdetectors are stored in a pipeline which extends over 24 consequent bunch crossing. Thus an event needs 2.3μs to pass through the pipeline. In this time window the L1 trigger can decide to keep the event. Only detector components which have a sufficiently fast rise time for the trigger signal can be used on this trigger level.

At L1 information from different subdetectors is delivered in the form of trigger bits,

the *trigger elements*, to the central trigger logic. Here the trigger elements are combined using logical AND and OR operations to form *subtriggers*. These subtriggers make the decision if an event is kept or rejected. In the year 2000 running period the trigger system was capable of 192 trigger elements and 128 subtriggers.

The total trigger rate at H1 is limited to $\approx$ 45Hz at the input to the Level 4 filter. Based on this condition every subtrigger only gets a certain trigger budget. If a subtrigger runs on a higher rate than its assigned bandwidth, it gets prescaled: A prescale of n means, that only every n^{th} time where the trigger condition is true, the central trigger assigns an L1KEEP signal to it. If a trigger condition was true, the 'raw' bit is set. If the trigger condition was true and the event was triggered by an L1KEEP signal due to this subtrigger, the 'actual' bit is set. If an event has the 'raw' bit set but the 'actual' bit is not, then the event has been triggered by another 'actual' subtrigger.

Once L1 issues an L1KEEP signal, the readout starts. The percentage of time in which the detector is being read out and cannot take data is referred to as *dead time*. The trigger elements and subtriggers, that are used in this analysis, are described in section 4.5.

Level 2: Some L1 subtriggers are subject to a L2 validation. If this fails, the L1KEEP signal assigned to this L1 subtrigger is revoked. However L2 will not necessarily reject the event as it might be triggered by another subtrigger. The L2 system is capable of prescaling like on L1 and as well of *overrides*, where some events are kept although the L2 verification failed. Both methods are not used at present.

On L2 22 μs can be used to produce a decision. Due to the longer time available more complex information can be processed and the rate of certain L1 subriggers can be reduced significantly without big losses in efficiency. The system is split into two subsystems, L2NN and L2TT[5]. The L2NN can combine information from various subdetectors and delivers a trigger decision based on a neural net. L2TT investigates trigger information for various topological patterns and produces a trigger decision based on this. L2NN and L2TT can provide up to 16 L2 trigger elements each.

Level 4: Contrary to the previous trigger levels L4 is implemented in software running on a dedicated processor farm. On L4 the total detector information is available and a fast event reconstruction is performed. Based on this incomplete reconstruction calibration constants are obtained and filter algorithms are run. The output of the read out is stored in *Physics Output Tapes* (POT).

[5]A new L2 system based on the new Fast Track Trigger (FTT) was taken into operation in 2005.

Level 5: Here the complete event reconstruction is performed using the calibration constants obtained on L4. Furthermore the events are classified in physics classes. The result of the reconstruction is stored on *Data Summary Tapes* (DST), which contain all information needed for data analysis.

2.8 Detector Simulation

As described in section 1.9, the underlying physical processes are modelled using Monte Carlo generators, which produce predictions on an event-by-event base. In order to compare these generated events with the measuered data a simulation of the detector response is needed. The detector response is modelled by the software package GEANT [9] and H1 specific software simulating the digital detector response and the trigger decisions. The output of this detector simulation is in the same format as the output of the detector and undergoes the same reconstruction steps. Thus the data and the simulated Monte Carlo events can be compared directly and efficiencies and detector acceptance can be extracted directly from the Monte Carlo simulation.

Chapter 3

Analysis Overview

This chapter describes the strategy of this analysis. The key features and selections are motivated and the background sources which will contribute to the final sample are described. The method which is used to separate beauty events from the backround sources will be described and finally an overview of the analysis strategy will be given. Details of the reconstruction will be given in chapter 4. The visible cross section will be defined and measured in chapter 5.

3.1 Event Signature

As described in section 1.8, the branching ratio for the semileptonic decays of a beauty hadron is roughly 20% both for decays into electrons and muons. Both the semimuonic and the semielectronic channel are candidates for the analysis of beauty production. However inside a jet a muon is more easy to identify than an electron. If its initial momentum is high enough, a muon traverses the tracking chambers and the calorimeters as a minimum ionising particle and leaves a clear signature in the outer muon systems. In the present analysis, a track in the Forward Muon Detector will be used as a signature.

The hadrons are produced in the fragmentation of the partons from the hard process. For beauty production these partons are either a $b\bar{b}$ pair or a beauty quark and a gluon. The decay products of these hadrons form jets. In next to leading order additional gluon radiation is possible, which can give rise to additional jets. The jet axis approximates the direction of flight of the initial parton. For the jet associated to the muon this is unavoidably smeared out by the missing momentum of the neutrino which is not detected.

The event selection for forward beauty production will require a muon in the FMD and two jets. Figure 3.1 shows a typical event from the final selection.

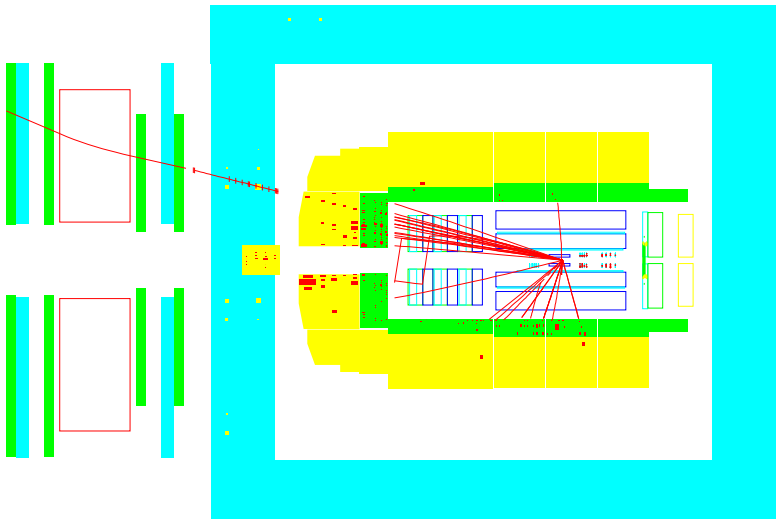

Figure 3.1: Display of an event from the final data selection, showing two jets and a muon passing through the FMD

3.2 Muon Identification

The muon will be identified in the FMD. In the forward region only the FMD can deliver a reliable identification of muons and an acccurate momentum measurement. A muon can in principle be identified as well by its signature as a minimum ionising particle in the LAr or as a track in the CMD. However these methods will fail for the events selected in this analysis:

Muon identification in the LAr is only possible if the muon is isolated from other particles. In the events considered in this analysis the muon is always accompanied by a jet and so there is high activity in the LAr. Hence the LAr cannot easily be used for muon identification in this analysis.

The inner region of the FEC which covers the polar angular range of this analysis suffers from punch through hadrons which are not fully absorbed in the LAr. A track in the FEC produced by one of those hadrons cannot be distinguished from a track produced by a genuine muon. Furthermore the FEC does not provide a momentum measurement. This means that to measure the momentum of a muon identified in the CMD one has to link the track in the CMD with track information from the inner trackers. For the angular range considered in this analysis the FTD would have to supply this information. In the running period of this analysis the tracking information of the FTD was very limited. Thus only the FMD can deliver reliable muon identification and kinematic for this analysis.

3.3 Background Processes

As beauty production is not the only process that can lead to the signature of two or more jets and at least one forward muon, the final event sample contains events from background processes which have to be taken into account. The main background sources are list below.

Charm production: The production processes for charm are the same as for beauty. The total cross section for charm production is about 200 times higher than for beauty production, see section 1.6. The requirement of two jets with a high transverse momentum and a muon will enrich the beauty contribution in this sample, but still there will be a sizeable contamination by charm events.

Light Flavour production: The total dijet cross section is much higher than the beauty production cross section and is dominated by the production of light quarks and gluons. Like in the charm case the contamination of the final sample by light flavour production will be reduced by the requirement of a high p_t muon.

In the decay of both heavy flavour and light flavour hadrons the most frequent hadrons in the final state are pions and kaons. Both are long lived with $c\tau \approx 7.8$m for pions and $c\tau \approx 3.7$m for kaons. They can decay within the volume of the detector, thus producing a muon with a branching ratio of $\approx 100\%$ for pions and $\approx 63\%$ for kaons [16]. Most pions and kaons will be stopped in the calorimeter before they can decay, but a small fraction will produce a muon. If the momentum of the decaying hadron is high enough, the produced muon will have a momentum high enough to traverse the FMD. Muons originating from light hadrons in heavy flavour events are not considered as signal in this analysis.

Misidentified hadrons (Punch through): Pions and Kaons have a small but non-negligible probability to pass through the LAr and leave a track in the CMD. These so called punch through hadrons make up a sizeable background in beauty analyses using muons reconstructed in the CMD. However in the forward region the hadron would have to traverse not only the FEC of the CMD but as well the toroid of the FMD. This is very improbable and so background from misidentified hadrons can be neglected in this analysis.

3.4 Monte Carlo Samples

The physics processes contributing to the final sample are simulated using the Pythia Monte Carlo generator. They are generated in the massless scheme. Generated particles

are only forced to decay by the event generator if their lifetime is less than 10^{-8}s. Resolved and excitation processes are included as predicted by the event generator. The samples used are:

Beauty: Events are generated with at least one beauty quark in the hard subprocess. Events with a least one generated muon with $p_\mu > 5\,\text{GeV}$ and $4^\circ < \vartheta_\mu < 25^\circ$ and two jets, reconsructed from the output of the event generator, with $E_t > 4\,\text{GeV}$ are selected. This sample consists of the channels $b \to c\mu\nu_\mu$, $b \to cX \to \mu\nu_\mu X'$ and $b \to c\tau\nu_\tau$, with $\tau \to \mu\nu_\mu\nu_\tau$. The sample corresponds to an integrated luminosity of 750pb^{-1}.

Charm: Events are generated with a least one charm quark in the hard subprocess. The further preselection is the same as in the beauty sample. This sample only contains the channel $c \to \mu\nu_\mu X$ and corresponds to an integrated luminosity of 250pb^{-1}.

Light flavours: The starting point for this sample is an inclusive production of all quark flavours accessible at HERA. The only requirements are two jets reconsructed from the generated particles with $p_t^{\text{jet}} > 4\,\text{GeV}$ and a forward particle with $8^\circ < \vartheta < 25^\circ$ and $p > 5\,\text{GeV}$. This particle is the possible seed for a muon produced in the decay of long lived hadrons. These decays are not produced by the event generator. Therefore this sample is processed with the H1 detector simulation. Here long lived hadrons can decay and eventually a muon can be produced within the kinematic range of this analysis. Only events are kept which have a reconstructed muon in the FMD. Events where the reconstructed muon can be mapped to a generated muon originating from beauty or charm production are vetoed, because these are already accounted for in the beauty and charm samples. The sample corresponds to an integrated luminosity of 50pb^{-1}.

Cascade Beauty: For cross checks a beauty sample was generated using Cascade. The selection is the same as in the Pythia beauty sample except of the Jet selection which is not performed. This sample was generated without final state parton showers. The integrated luminosity is 50pb^{-1}.

3.5 Separation of Beauty From Other Processes

The data sample which will be the basis of this analysis will consist of beauty, charm and light flavour hadrons. Two features of beauty hadrons can be used to determine the beauty fraction in the final sample: The long lifetime of beauty hadrons and their high mass. The long lifetime of the beauty hadrons can only be exploited using a precise silicon vertex detector. The Forward Silicon Tracker was only taken into operation in the year

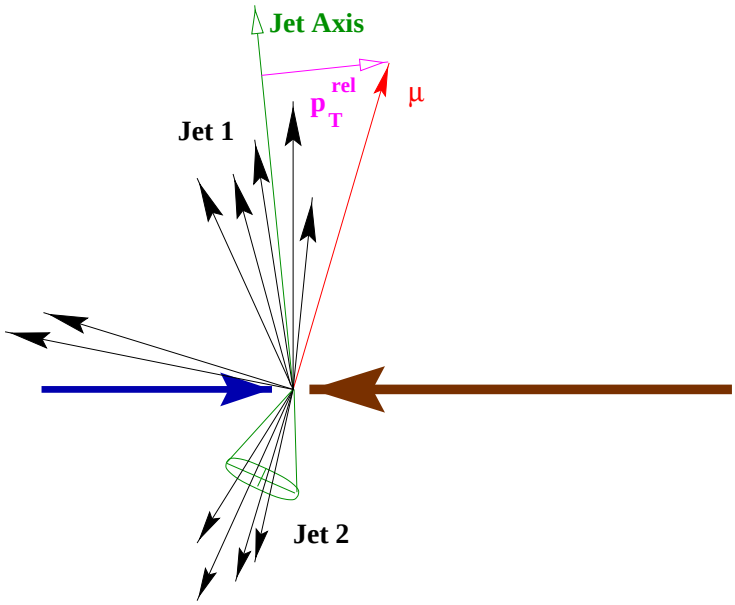

Figure 3.2: Sketch of the definition of p_t^{rel}

2004. So for the 2000 data taking period the decay length of the beauty hadrons cannot be exploited for an analysis in the forward region.

Therefore the high mass of the beauty quarks is used as the separating feature. In the decay from beauty to charm the large mass difference between the b quark and the c quark has to be transferred into kinetic energy of the lighter decay products. These masses are $4.0\,\text{GeV} \leq m_b \leq 4.5\,\text{GeV}$ and $1.0\,\text{GeV} \leq m_c \leq 1.4\,\text{GeV}$ [16]. In the rest frame of the decaying hadron the muon will have a higher momentum for beauty decays than for charm and light flavour decays. This difference is exploited in the p_t^{rel} method. p_t^{rel} is defined as the relative transverse momentum of the muon with respect to its associated jet:

$$p_t^{rel} = \frac{\overrightarrow{p}_\mu \times (\overrightarrow{p}_{\text{jet}} - \overrightarrow{p}_\mu)}{|\overrightarrow{p}_{\text{jet}} - \overrightarrow{p}_\mu|}. \tag{3.1}$$

The variable is illustrated in figure 3.2. To obtain a better separation power, the muon is excluded from the jet in the definition of p_t^{rel}. Reference spectra for p_t^{rel} of beauty, charm and light flavours are obtained using the Pythia Monte Carlo simulation. These will be shown in figure 5.1 on page 77. The weighted sum of these spectra will be fitted to the p_t^{rel} distribution of the data. The fit yields the fraction of beauty events in the data.

3.6 Analysis Strategy

From these basic ingredients the analysis strategy can be laid out. Events with a forward muon and at least two jets will be selected. Cuts against background will be applied. The observable p_t^{rel} will be used to separate beauty events from the background events on a statistical basis. This separation procedure will yield the fraction of beauty events in the total data sample. From this the visible cross section will be calculated in chapter 5.

Chapter 4

Data Selection

As stated in the previous chapter, the signature of forward beauty photoproduction are two jets and a muon. This chapter will describe the detailed selection of data events. The events are selected from the year 2000 running period corresponding to an intergrated luminosity of 45pb^{-1}.

4.1 Muon Selection

Muons are identified in the FMD. The FMD provides a momentum measurement independent from the inner trackers. Only muons can traverse the FMD. Hadrons which penetrate the LAr, so called *punch through hadrons*, will be stopped in the toroid. Thus they cannot produce a valid FMD track. Therefore the FMD delivers all information necessary for the identification and reconstruction of muons in this analysis.

4.1.1 Muon Reconstruction Using the FMD

A muon in this analysis is always accompanied by a forward jet, which causes high track multiplicities in the FTD. Presently it is not possible to unambiguously link the FMD track to a track in the FTD and so only the information from the FMD is used to reconstruct the momentum vector of the muon. The muon track is approximated by a straight line from the reconstructed vertex of the event to its impact point in the FMD. In this approach the magnetic field of the solenoid of the detector is neglected. This introduces a small mismeasurement of the φ coordinate. This effect is shown in figure 4.5 and will be discussed below. The polar and azimuthal angle of this line and the momentum reconstructed in the FMD are sufficient to determine the momentum vector, see figure 4.1.

In order to achieve an accurate momentum measurement the muon has to traverse the pre- and post-toroidal layers of the FMD. Only if a pre and a post toroidal track segment can be linked, the bending angle can be measured and the momentum of the muon can

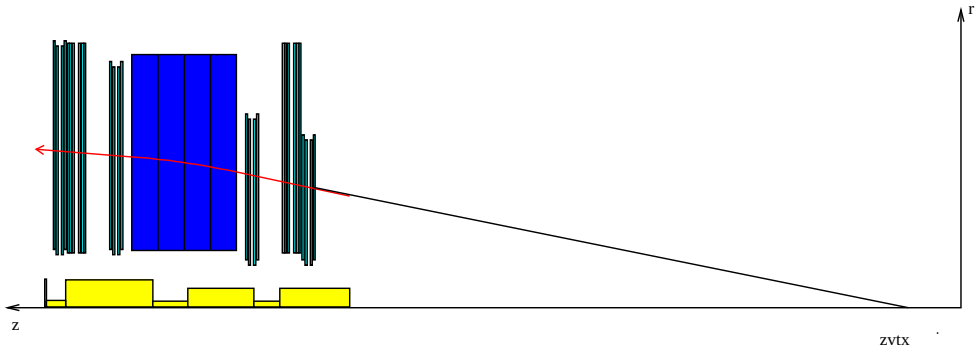

Figure 4.1: Sketch of the reconstruction of the muon momentum vector: The drawing shows a side view of the upper hemisphere of the experiment. Only the FMD is shown. A straight line is drawn from the starting point of the pre-toroid track to the reconstructed vertex of the event.

be calculated. The momentum is determined in the following way[1]: The pre-toroid track is extrapolated through the toroid using 52 different momentum hypotheses, taking into account the magnetic field of the toroid and the energy loss of the muon. The principle is illustrated in figure 4.2. For each of these momentum hypotheses a χ^2 for the fit of the pre- and post-toroid track segments is calculated and the hypothesis with the lowest χ^2 is taken as a preliminary momentum measurement if the χ^2 is below a given threshold. The momentum measurement is then further refined: The χ^2 determined in the fit is plotted as a function of the assumed momentum. A quadratic function is fitted through the determined point of minimal χ^2 and the two adjacent points. The minimum of this function is then taken as the momentum measurement.

Depending on the outcome of this fit a quality grade is assigned to the reconstructed muon track. The classification depends on the inputs used for the χ^2 fit and of the result of the fit:

5: The fit could only determine a minimal χ^2 for the lowest momentum hypothesis. This means that the momentum could not be determined, but the charge determination is correct.

4: A minimum χ^2 was found, but the track, which is reconstructed, laterally exits the toroid.

3: Only the impact coordinates were used for the track fit.

2: Only the slope was used for the track fit.

[1] A more detailed description of the reconstruction in the FMD can be found in [25].

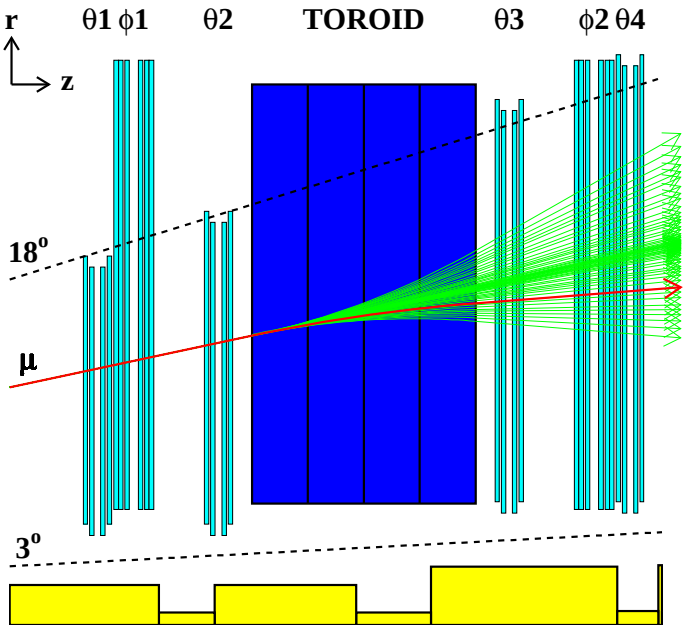

Figure 4.2: Illustration of the FMD momentum scan

1: Both, impact coordinates and slope were used for the track fit .

In order to obtain the best possible momentum measurement only grade 1 tracks are used in this analysis.

On its way from the interaction point to the first layer of the FMD the muon looses approximately 3 GeV. On average 2 GeV are lost in the transit through the toroid. Thus the muon needs a minimum momentum of 5 GeV to be reconstructed and measured in the FMD. The Forward Muon Trigger is efficient for $p_\mu > 7$ GeV as will be shown below. The FMD covers the angular range $4° < \vartheta < 20°$, the acceptance of the FMD restricts the angular range to $8° < \vartheta < 18°$. A good description of the data by the detector simulation can only be achieved for $\vartheta > 10°$. This is illustrated in figure 4.3. The distribution of the Monte Carlo simulation is flat up to the lower acceptance cut at $\vartheta_\mu \approx 5°$. The distribution in the data drops off for $\vartheta_\mu \lesssim 10°$. Thus a cut on $\vartheta_\mu > 10°$ is applied.

The reconstruction efficiency of the FMD and the applied cuts are shown in figure 4.4. The applied cuts on ϑ_μ and p_μ are shown as vertical lines. The acceptance threshhold at $p_\mu = 5$ GeV is clearly visible.

The accuracy of the muon reconstruction was checked using the Pythia Monte Carlo simulation: The correlations between generated and reconstructed properties are shown in figure 4.5. The plots show good agreement between the generated and reconstructed values. The ϑ resolution is better than 0.5°. Figure b2) shows a double peak structure.

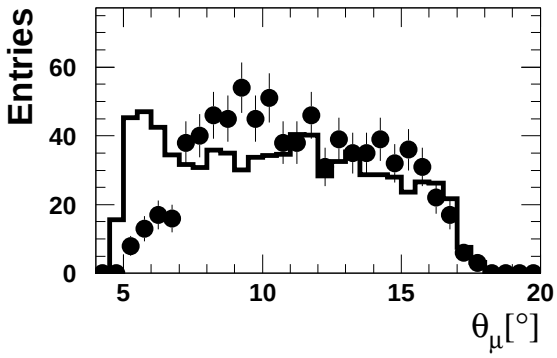

Figure 4.3: Distribution of ϑ_μ in the data and the description by the Pythia Monte Carlo simulation. The events in this plot have to pass the final event selection except the cuts on ϑ_μ and the maximum distance between the muon and its associated jet. The events are triggered by subtrigger s71, so no bias by the Forward Muon Trigger is introduced. The Monte Carlo sample is a mixture of beauty, charm and light flavour samples. The used fractions are obtained from the final fit of this analysis, the sum is normalised to the distribution of the data. At low values of ϑ_μ the distribution is very badly described by the simulation.

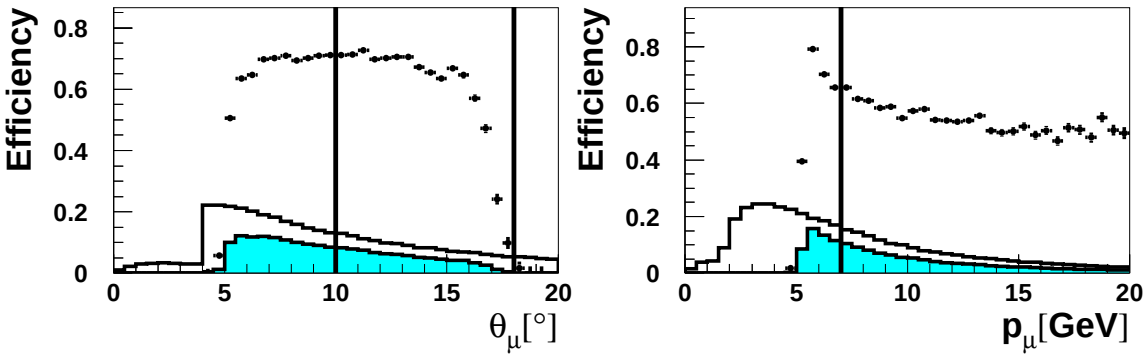

Figure 4.4: The reconstruction efficiency of the FMD as function of the azimuthal angle and the momentum of the muon. The vertical lines show the applied cuts. In the plot for ϑ_μ the cut on p_μ is applied and vice versa. The open histogram shows the distribution of the generated events, the filled histogram shows the distribution of the reconstructed events.

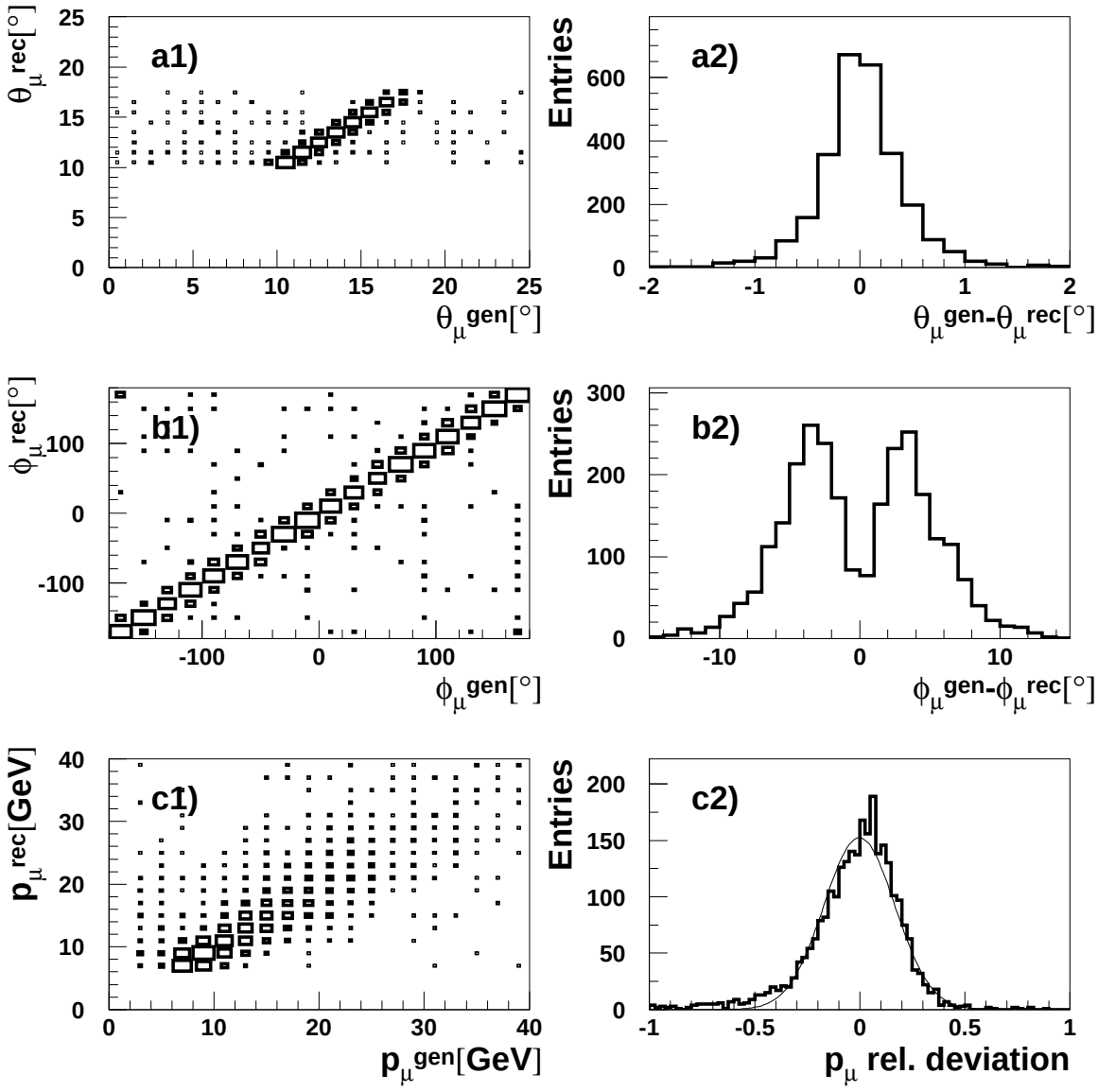

Figure 4.5: Correlations of the generated and reconstructed kinematic properties of the muon. Figure a1) shows the correlation between the generated and reconstructed azimuthal angle, and figure a2) shows the difference between these values. Figure b1) and b2) show the same for the polar angle. Figure c1) shows the correlation between the generated and the reconstructed momentum of the muon and figure c2) shows the relative deviation of the momentum measurement, defined as $(p_\mu^{\mathrm{gen}} - p_\mu^{\mathrm{rec}})/p_\mu^{\mathrm{gen}}$.

This effect is generated by the simplified treatment of the muon track. In the track reconstruction this is assumed to be a straight line coming from the event vertex. In this approximation the influence of the magnetic field of the solenoid is neglected. The magnetic field bends the track of the muon in the $r\varphi$ plane. The direction of this deflection depends on the charge of the muon and this produces the double peak structure. Figure c2) shows the momentum resolution of the FMD. A fit of a Gaussian function to the histogram yields a resolution of $\approx 16\%$.

4.1.2 Cross Checks with J/ψ Mesons

The momentum measurement calculated from the FMD reconstruction is the momentum of the muon at its entry point into the FMD. This has to be corrected for the energy loss of the muon on its way from the event vertex to the surface of the FMD. 3 GeV are added to the reconstructed momentum of the muon. The validity of this correction is checked with a sample of J/ψ candidates from the year 2000 data taking period: Events are selected with a muon reconstructed in the FMD and exactly one track in the angular region $20^\circ < \vartheta < 160^\circ$, which was identified as a muon by either its signature as minimum ionising particle in the LAr or by an associated track in the CMD. The invariant mass of this pair of tracks is reconstructed under the hypothesis that both tracks are produced by genuine muons. The events are required to be triggered by the FMD subtrigger s16. The distribution of the invariant mass is shown in figure 4.6, showing a clear peak. The position of this peak is used to check the validity of the FMD momentum reconstruction. The momentum measurement of the track in the central region is very accurate, so any shift of the peak position from the known mass of the J/ψ of $M_{J/\psi} = 3.097\,\mathrm{GeV}$ [16] would be due to an inaccurate reconstruction of the momentum of the forward going muon.

The signal is modelled by a Gaussian function. The background is assumed to be the sum of two Gaussian functions. The sum of this function is fitted to the data. The result of this fit is shown in figure 4.6 as the solid line. The position of the signal peak is calculated as $M^{\mathrm{rec}}_{J/\psi} = 3.102 \pm 0.012\,\mathrm{GeV}$ which agrees within errors with the world average. Therefore the correction method of adding 3 GeV to the reconstructed momentum in the FMD is proven to be correct. The width of the signal peak is 230 MeV. In comparison the J/ψ signal reconstructed using two muons in the central region has a width of ≈ 50 MeV [20]. The signal peak reconstructed from a central muon and a muon in the FMD is considerably broader. This is due to multiple scattering of the muon on its way to and through the FMD and the resolution of the FMD which is inferior to that of the CJC.

The polar and azimuthal angle and the momentum of the muon reconstructed in the FMD and the z coordinate of the point of closest approach of the extrapolated pre-toroid track with the z axis of the H1 coordinate system as defined in equation 4.1 on page 50,

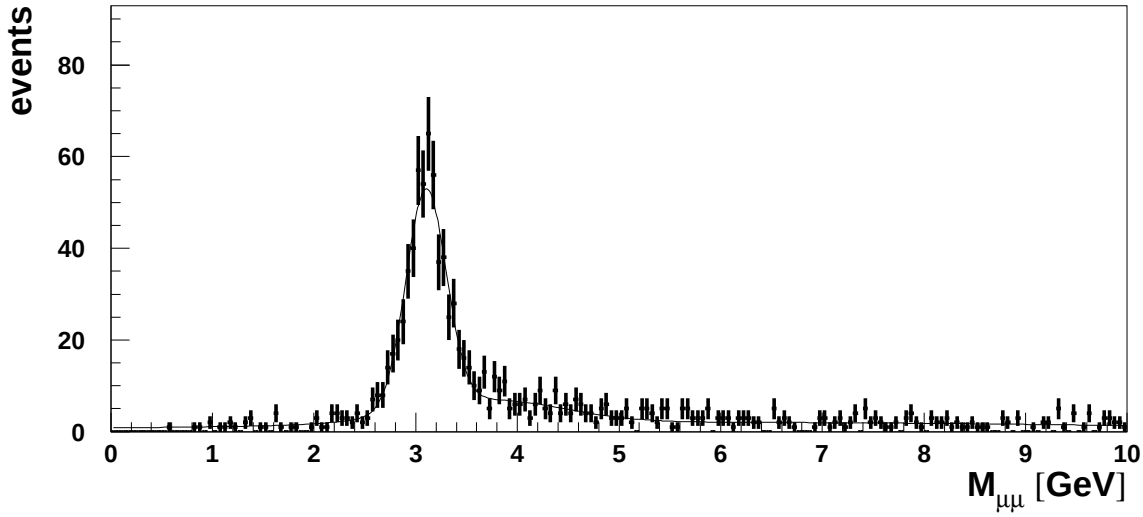

Figure 4.6: Distribution of the invariant mass of the J/ψ candidates. The crosses show the distribution of the data, the solid line is the result of the fit to the data. The J/ψ signal is modelled by a Gaussian function, the background is modelled as the sum of two Gaussian functions.

are shown in figure 4.7.

4.1.3 Final Muon Selection

To select a clean sample for the beauty measurement, further quality criteria have to be applied: The sense wires of the FMD have a lack of response at their readout ends. This leads to a structure seen in the xy hitmap known as the *Maltese Cross* effect [25], see figure 4.8. The events are taken from the preselection of this analysis, which consists of events with two jets and a forward going muon. They have been triggered by subtrigger s71 and hence are independent of the Forward Muon Trigger. This effect is not modelled in the detector simulation and hence events with a track in the FMD within a wedge of $\pm 4°$ around each diagonal in the xy plane are excluded from the selection.

Figures 4.9 a) - d) show the distribution of the polar and azimuthal angle of the reconstructed muon, its momentum and its transverse momentum. Figure 4.9 e) shows the relative error of the momentum reconstruction as calculated in the FMD reconstruction. All events in these plots have to pass the final selection of this analysis[2]. All these variables are very well described by the Monte Carlo simulation.

Furthermore the pre-toroid track is required to point to the primary vertex. Because

[2]The final event selection will be laid out in the following pages and summarised in section 4.8 on page 75.

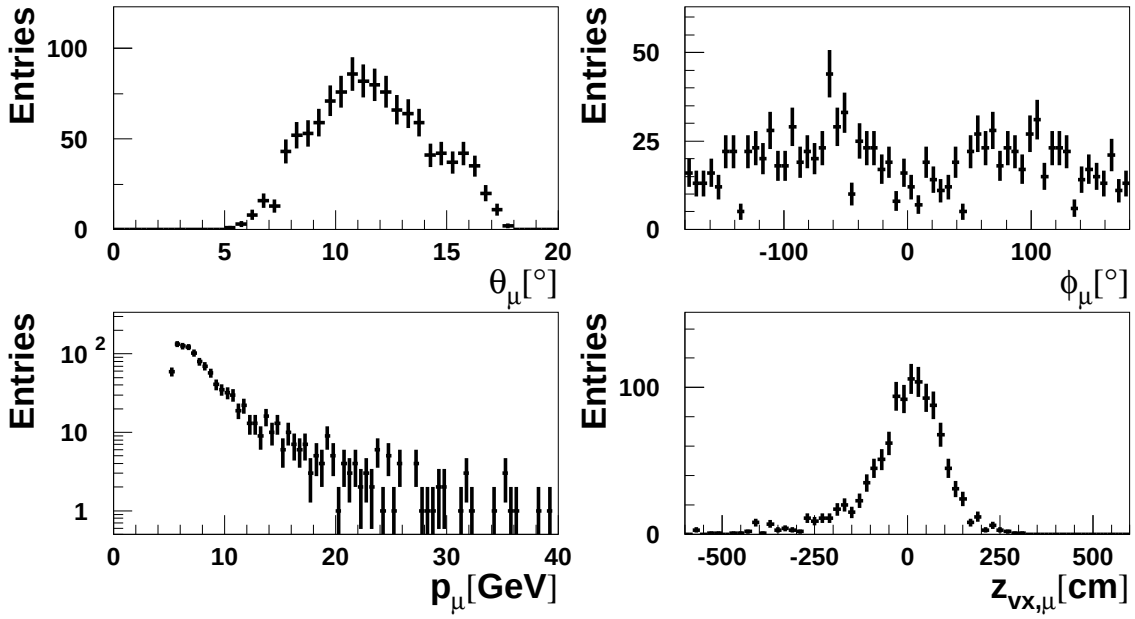

Figure 4.7: Distribution of the polar angle, the azimuthal angle and the momentum of the muon reconstructed in the FMD and the distribution of $z_{\mathrm{vx},\mu}$ for the sample of J/ψ candidates.

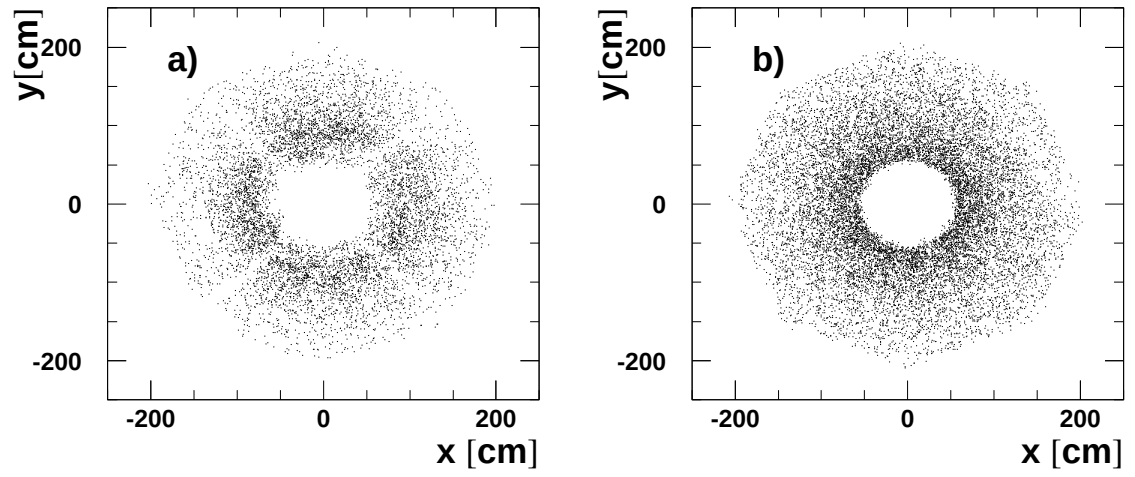

Figure 4.8: xy hitmap of good quality muons for data (a) and Monte Carlo simulation(b).

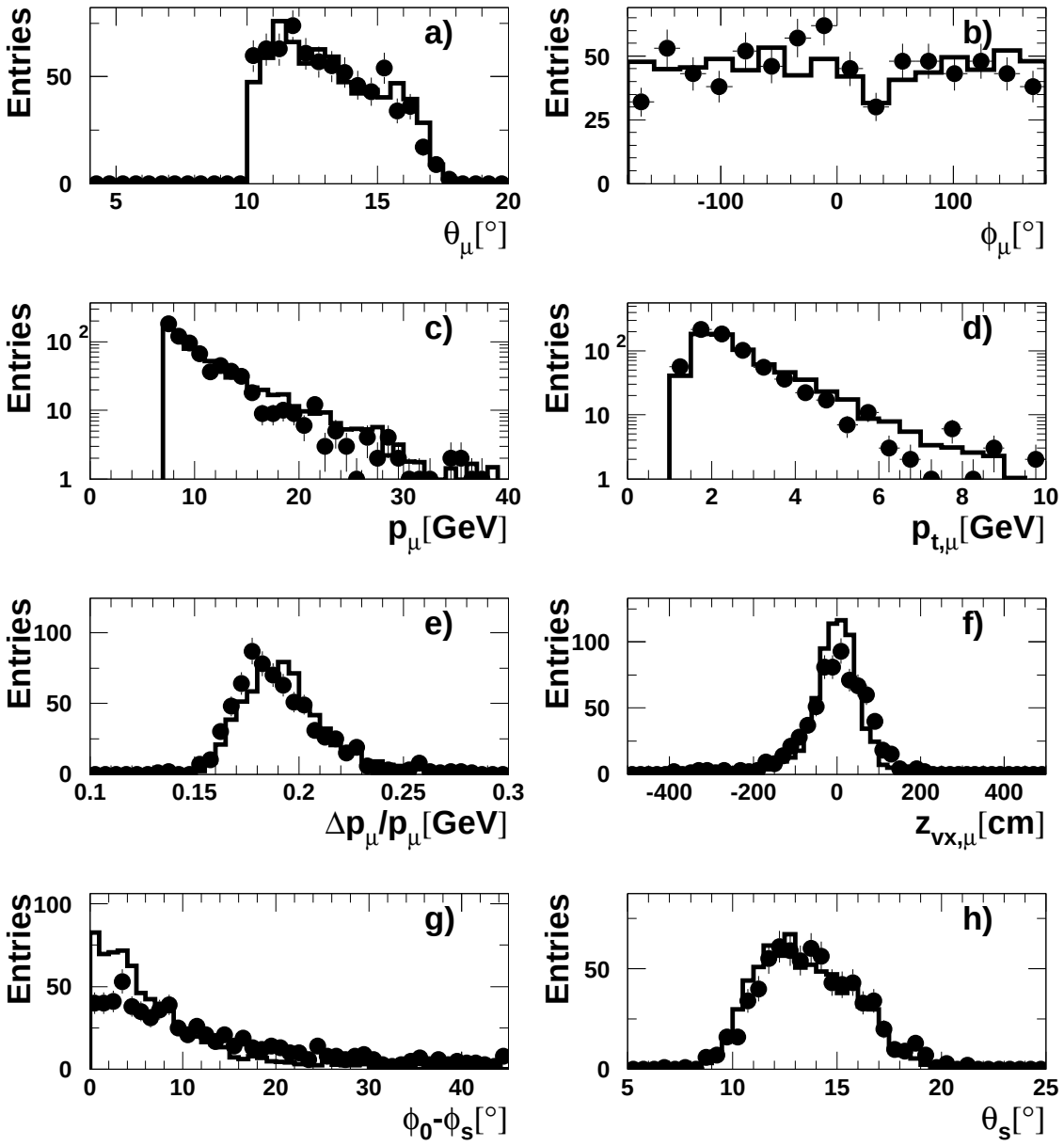

Figure 4.9: Distribution of a) the polar angle, b) the azimuthal angle, c) the momentum, d) the transverse momentum of the muon reconstructed in the FMD, e) the relative uncertainty of the momentum measurement, f) $z_{\mathrm{vx},\mu}$, g) the difference between the azimuthal coordinate of the start hit of the pre-toroid track and the azimuthal component of its slope and h) the azimuthal slope of the pre-toroid track. The events in these histograms have to pass the final selection of the analysis. The relative contributions of beauty, charm and light flavours in the Monte Carlo simulation are taken from the fit result of this analysis, the sum of the contributions is normalised to the data.

of multiple scattering the slope of the pre-toroid track will not exactly point to the event vertex. The pre-toroid track is extrapolated to its point of closest approach with the z axis. The z coordinate of this point is given by

$$z_{\mathrm{vx},\mu} = z_0 - \frac{r_0}{\tan\vartheta_s}\frac{1}{\cos\left(\varphi_0 - \varphi_s\right)}, \tag{4.1}$$

where (z_0, r_0, φ_0) denote the coordinates of the starting point of the FMD track in cylindrical coordinates and ϑ_s and φ_s denote the slope of the pre toroid track. This coordinate is required to lie within $-400\mathrm{cm} < z_{\mathrm{vx},\mu} < 300\mathrm{cm}$. This cut is already applied on trigger Level 4, see section 4.5 on page 64. This cut reduces proton beam induced background, which mainly originates from the backward region, where collimators are placed in the beam pipe. Figure 4.9 f) shows the distribution of $z_{\mathrm{vx},\mu}$ and its description by the Monte Carlo simulation. The distribution in the data is broader than in the Monte Carlo simulation. This can be explained by the inaccurate simulation of the slope of the pre-toroid track as can be seen in figures 4.9 g) and h). The ϑ-component of the slope is very well described, however the φ component is not.

4.2 Jet Reconstruction

Jets are used to identify events with high momentum partons, as the jet axis approximates the direction of flight and the momentum of the decayed hadron. Jets are reconstructed from the hadronic final state (HFS). The HFS objects are formed by combining tracks and calorimeter clusters. Tracks are only used if they are reconstructed using CJC information. The HFS objects serve as input to the jet algorithm.

4.2.1 Reconstruction of the Hadronic Final State

The HFS has to reflect the energy and momentum distribution in the event. Tracks from charged particles are combined with clusters in the LAr to reconstruct all particles produced in the event. Charged particles with a momentum sufficiently high to reach the LAr produce a track and a cluster and a matching algorithm is applied to select the object with the best estimate of the true energy and to avoid double counting of the particle momenta.

Track and vertex reconstruction: Tracks are reconstructed from hits in the central tracker. They form part of the hadronic final state which serves as input for the jet finding. Furthermore they are used to constrain the primary vertex of the event. Hits in the CJCs, CIZ and COZ are used for the track finding. As a first step tracks are fitted in the $r\phi$ plane without the constraint that they come from a common vertex. In a combined fit

these tracks are then used to determine the primary vertex of the event. Only tracks, which fulfil minimal quality requirements are used.

Reconstruction of Clusters in the LAr: The energy in the LAr is collected in cells. The reconstruction algorithm combines the energy deposit in nearby cells and combines the cell energies to clusters, where the position of the cluster is taken as the centre of gravity of the cell energies.

Track Cluster Matching: Neutral particles only leave clusters in the LAr. Here the energy deposit in the LAr gives the energy of the particle. Charged particles leave a track in the central tracker and produce a cluster in the LAr. To avoid double counting of the energy, clusters and tracks have to be matched: Every track is extrapolated into the LAr and if a cluster is found within a small distance of the impact point the track and the cluster are merged to form a HFS object. For tracks with a p_t of less than 20 GeV the momentum of the particle is taken from the track, if the track has a higher p_t the energy measurement is used. Clusters which cannot be matched to a track form individual HFS objects. Only tracks which were reconstructed using CJC information are considered. For $\vartheta \lesssim 20^\circ$ tracks are reconstructed only from FTD information and these tracks are not used as input for the HFS.

4.2.2 Jet Algorithm

Jets are identified by running a jet algorithm on the HFS objects, which are characterised by their position in the $\eta\varphi$ plane and their transverse energy E_t. The algorithm merges HFS objects into jets. In this analysis the inclusive k_t algorithm [10, 18] in the massless scheme is used:

1. for each pair of HFS objects ij a distance parameter is defined:

$$d_{ij} = min(E_{t,i}, E_{t,j})^2 \frac{R_{ij}^2}{R_0^2},$$

   where R_{ij} is the distance of the objects in $\eta\varphi$ space: $R_{ij}^2 = (\eta_i - \eta_j)^2 + (\varphi_i - \varphi_j)^2$, and R_0 is a distance parameter which is set to 1.

2. For each object k a distance measure to the beam direction is defined: $d_k = E_{t,k}^2 R_0^2$.

3. The object with the minimum d_k and the pair with the minimum d_{ij} are identified. If

   - $d_k < d_{ij}$: object k is defined as a jet and removed from the list of input objects.

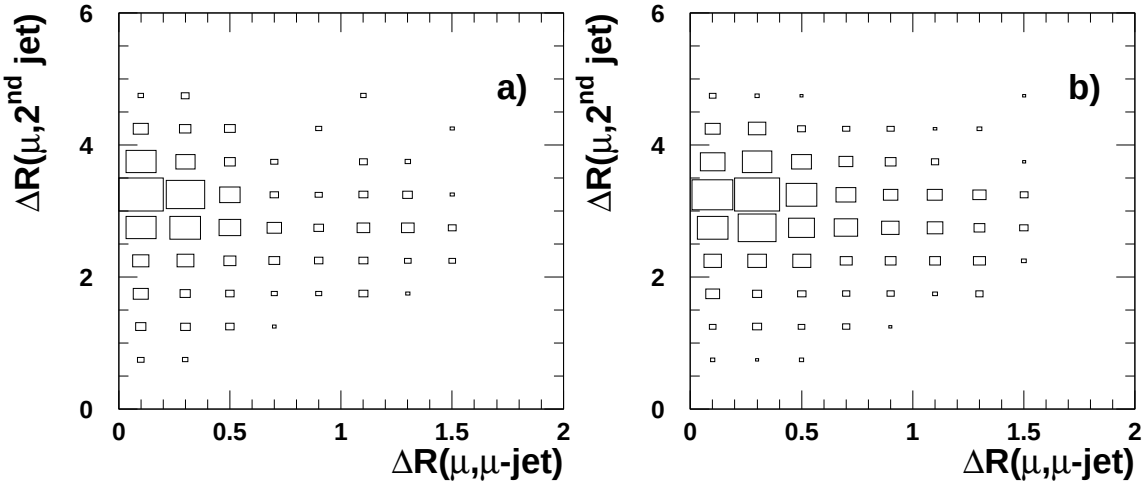

Figure 4.10: Distance of the muon to the muon jet versus distance of the muon to the second jet for the final data selection in data (a) and in the Pythia beauty Monte Carlo simulation (b). The events in these plots have to pass the final selection of this analysis.

- $d_k > d_{ij}$: objects i and j are merged to a new object l with

$$E_{t,l} = E_{t,i} + E_{t,j},\ \eta_l = \frac{\eta_i E_{t,i} + \eta_j E_{t,j}}{E_{t,l}} \text{ and } \varphi_l = \frac{\varphi_i E_{tij} + \varphi_j E_{t,j}}{E_{t,l}}.$$

4. This procedure is repeated until all objects are merged into jets.

4.2.3 Jet Muon Association

A muon passes the LAr as a minimum ionising particle and thus deposits little energy. The FTD is not used for the reconstruction of the HFS and therefore a muon identified in the FMD does not generally form a HFS object. This means that the association of the muon to a jet has to be done after the jet finding. This association works in the following way: For each jet the momentum vector of the muon is temporarily added to the momentum vector of this jet. Out of these temporarily formed jets, if they pass the kinematic cuts described in the next section, the jet which is closest to the muon in the $\eta\varphi$ space is identified as the muon jet and the muon is incorporated permanently into the momentum vector of the jet. The event is kept if the distance of the muon to the jet axis in $\eta\varphi$ space is less than 1.5. The correlation of the distances between the muon jet and the muon and the distance of the second jet and the muon are depicted in figure 4.10.

4.2.4 Jet Selection

Reliable jet reconstruction is only possible within a certain fiducial volume. If the lower cut on ϑ is applied at a too low value, parts of the jet will not any more lie within the

acceptance of the LAr. The LAr in the forward region covers the angle $\vartheta > 4°$. To ensure that all particles of the jet are reconstructed the angular range of the jet axis is restricted to $10° < \vartheta < 170°$. The jet axis can only be reconstructed safely, if the jet has a sizeable transverse energy. The accurate reconstruction of the jet axis is crucial for the determination of p_t^{rel}, the variable, which will be used to determine the beauty contribution to the data sample. The resolution of the ϑ component of the muon jet's axis and p_t^{rel} are shown in figure 4.11 for different E_t thresholds, calculated from the Monte Carlo simulation: The jet algorithm is run both on the four vectors of the generated particles and on the reconstructed HFS and the difference is plotted for ϑ and for p_t^{rel}. A good reconstruction of the jet axis is only possible for $E_t \gtrsim 7\,\mathrm{GeV}$.

Jets are selected with $E_t^{\mu\ \mathrm{jet}} > 7\,\mathrm{GeV}$ and $E_t^{2^{\mathrm{nd}}\ \mathrm{jet}} > 6\,\mathrm{GeV}$. The asymmetry in the E_t cuts is motivated by the NLO calculations. If the same cut is applied to both jets, gluon radiation is suppressed in the event generation and the results of the calculation become unphysical. The distributions of the polar angle, the azimuthal angle, the energy and the transverse energy in the final data set and their description by the Pythia Monte Carlo simulation are shown in figure 4.12 for the muon jet and in figure 4.13 for the second jet[3]. Figure 4.14 shows the distance of the jets in η and φ.

The data is generally well described by the Monte Carlo simulation. The distribution of the transverse energy of the muon jet shows a light overshoot of the data with respect to the Monte Carlo simulation for high values of $E_t^{\mu\ \mathrm{jet}}$. The distribution of $\vartheta^{2^{\mathrm{nd}}\ \mathrm{jet}}$ shows an overshoot of the data with respect to the Monte Carlo simulation at low values of $\vartheta^{2^{\mathrm{nd}}\ \mathrm{jet}}$. The overshoot of the data with respect to the Monte Carlo simulation in the $\Delta\eta$ distribution at low values of $\Delta\eta$ corresponds to the discrepancy seen in the distributuion of $\vartheta^{2^{\mathrm{nd}}\ \mathrm{jet}}$, since $\vartheta^{\mu\ \mathrm{jet}}$ is well decribed by the Monte Carlo simulation.

4.3 Kinematic Reconstruction and Jet Multiplicities

The kinematic variables important in this analysis are the inelasticity y and and the observable x_γ. x_γ is the energy fraction of the incoming partron from the photon which takes part in the hard interaction in the proton rest-frame. In photoproduction the scattered electron remains undetected and cannot be used for the reconstruction of the event kinematics. Therefore the Jaquet-Blondel method [26] is used to reconstruct the event kinematics:

$$y_{\mathrm{JB}} = \frac{\Sigma_h (E_h - p_{z,h})}{2E_e},$$

where the sum runs over all HFS objects h including the muon reconstructed in the FMD. For low values of y the hadronic final state will be concentrated in the forward region of

[3]The corresponding plots for the selected muon were already shown in figure 4.9 on page 49.

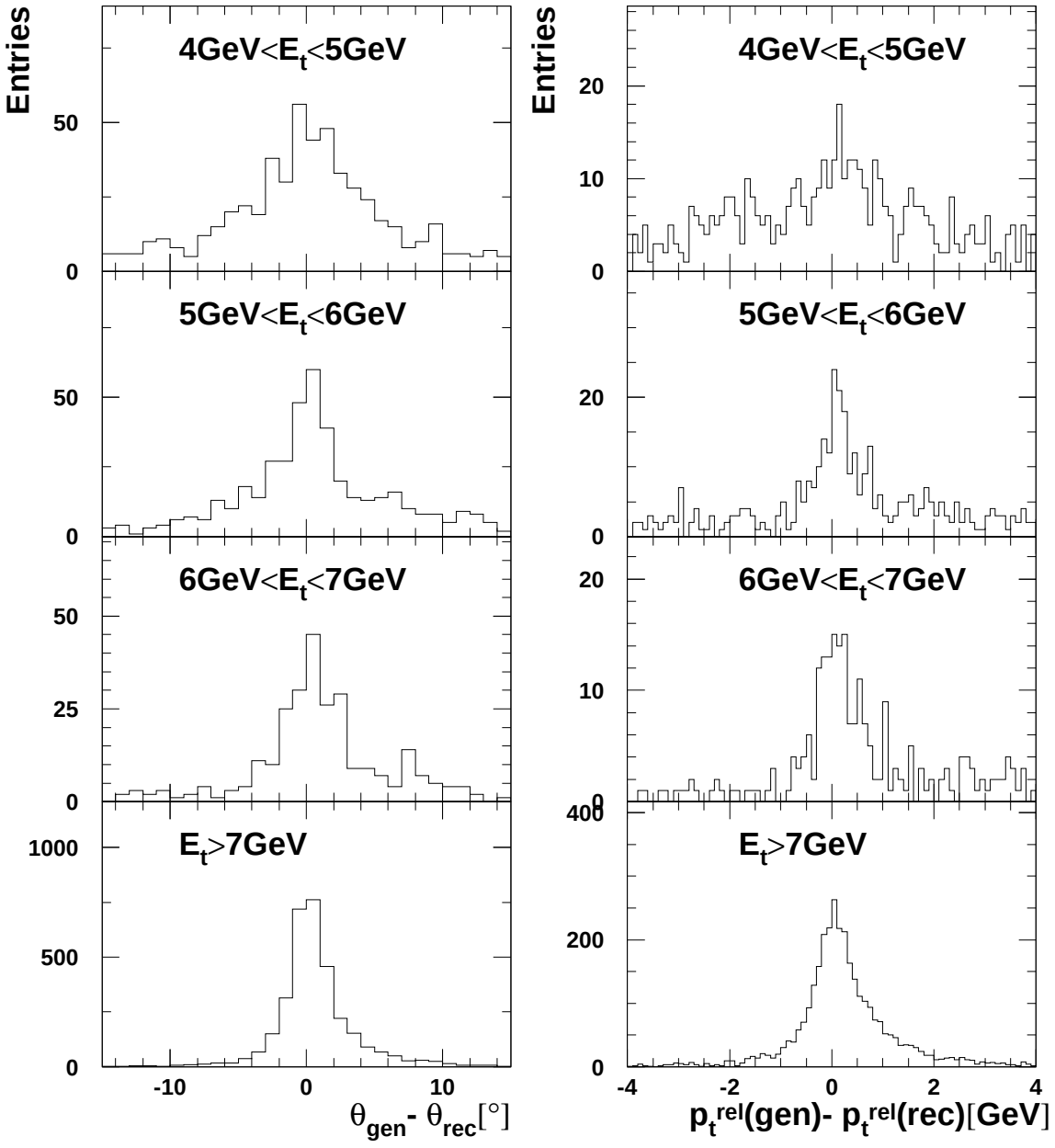

Figure 4.11: $\vartheta_{\mu\,\mathrm{jet}}$ and p_t^{rel} resolution for different regions of $E_t^{\mu\,\mathrm{jet}}$. The event is only accepted if $E_t^{\mu\,\mathrm{jet}} > 7\,\mathrm{GeV}$.

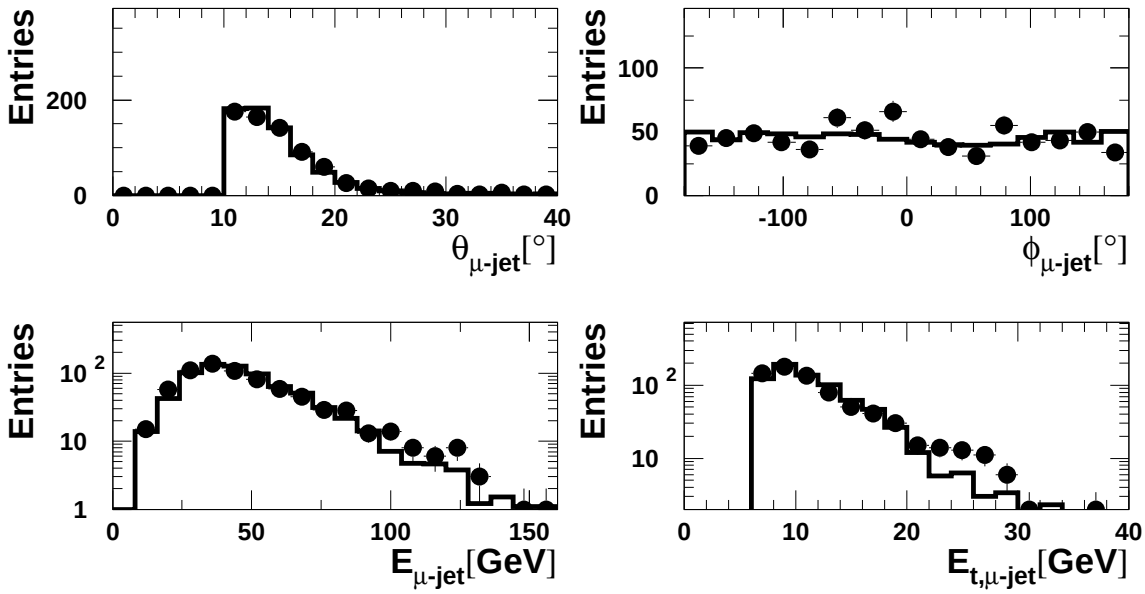

Figure 4.12: Control distributions for the muon jet. The events in these histograms have to pass the final selection of the analysis. The relative contributions of beauty, charm and light flavours in the Monte Carlo simulation are taken from the fit result of this analysis, the sum of the contributions is normalised to the data.

the LAr and parts of the hadronic final state will not be reconstructed. Thus a cut of $y > 0.1$ is applied.

In resolved processes only a fraction x_γ of the momentum of the photon enters the hard interaction. The remaining momentum fraction enters the *photon remnant*. x_γ can be calculated from the final state as

$$x_\gamma = \frac{\Sigma_{fs}(E_{fs} - p_{z,fs})}{\Sigma_h(E_h - p_{z,h})}, \tag{4.2}$$

where the sum in the numerator extends over all particles produced in the hard interaction and the sum in the denominator extends over all particles emerging from the ep interaction, except the scattered electron. In a leading order picture the energy flow from the hard interaction is concentrated in two jets, so the sum in the numerator can be replaced by a sum over the two jets. However in next to leading order processes additional gluon radiation is possible which gives rise to additional energy flow possibly not contained in the first two jets. Experimentally one can only identify the final state of the reaction by the two jets with the highest transverse momentum. It is impossible to attribute additional energy flow either to the hard interaction or to the photon remnant. Therefore a new

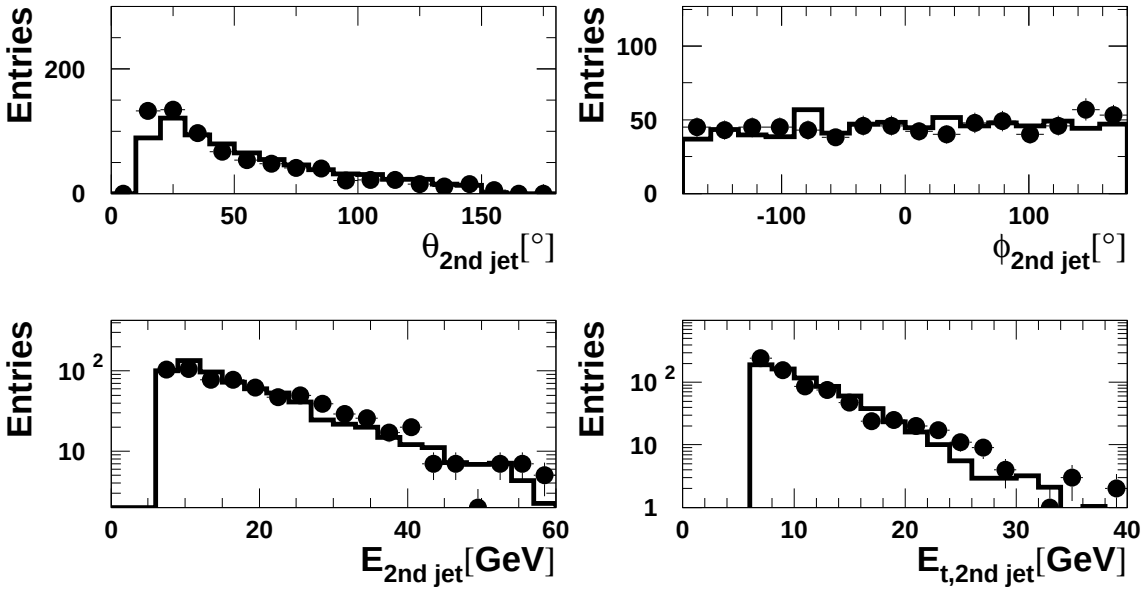

Figure 4.13: Control distributions for the 2$^{\text{nd}}$ jet The events in these histograms have to pass the final selection of the analysis. The relative contributions of beauty, charm and light flavours in the Monte Carlo simulation are taken from the fit result of this analysis, the sum of the contributions is normalised to the data.

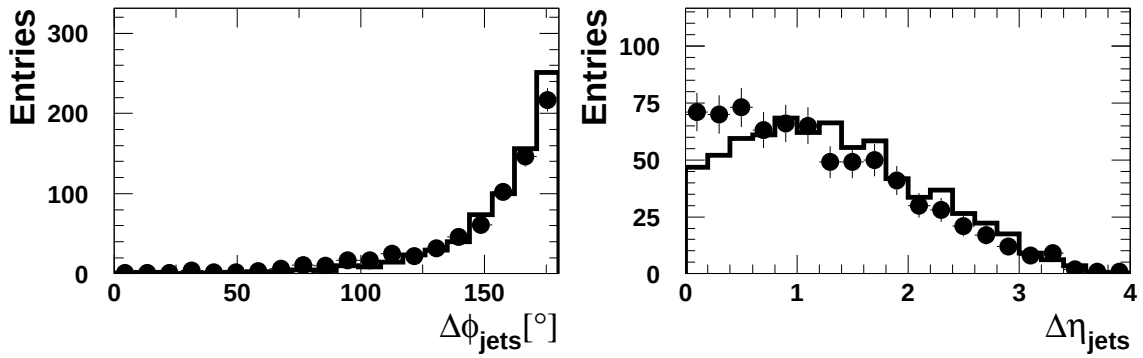

Figure 4.14: Control distributions for the correlations between the jets. The events in these histograms have to pass the final selection of the analysis. The relative contributions of beauty, charm and light flavours in the Monte Carlo simulation are taken from the fit result of this analysis, the sum of the contributions is normalised to the data.

quantity $x_\gamma^{\rm obs}$ is defined as

$$x_\gamma^{\rm obs} = \frac{\Sigma_{\mu\ \rm jet}(E-p_z) + \Sigma_{2^{\rm nd}\ \rm jet}(E-p_z)}{\Sigma_h E_h - p_{z,h}}, \tag{4.3}$$

which in a leading order picture and given a jet algorithm that collects all particles from the hard interaction into the right jet is equal to x_γ. The effects of this reconstruction method are illustrated in figure 4.15. Figure 4.15 a) shows the distribution of $x_\gamma^{\rm gen}$ as generated by the Pythia Monte Carlo simulation. Only the distributions for resolved and excitation processes are shown because for the direct production process $x_\gamma^{\rm gen}$ has a fixed value $x_\gamma^{\rm gen} = 1$. Figure 4.15 b) shows the distribution of $x_\gamma^{\rm obs,\ gen}$ as reconstructed from the jets obtained by applying the jet algorithm to the generated particles. Figure 4.15 d) shows the corresponding resolution. In the direct process the definition of x_γ implies $x_\gamma^{\rm obs,\ gen} < x_\gamma$. Because of the imperfect approximation of the hard interaction by the produced jets [4] the reconstructed $x_\gamma^{\rm obs}$ is smeared out with respect to the true x_γ. Figure 4.15 c) shows the distribution of $x_\gamma^{\rm obs}$ reconstructed from the HFS. Figure 4.15 e) shows that $x_\gamma^{\rm obs}$ is reconstructed very accurately.

The tail towards low values of $x_\gamma^{\rm obs,\ gen}$ for the direct component in figure 4.15 b) is mainly attributed to additional jets. In direct production these have to be generated in the hard interaction by gluon radiation or jet splitting due to the large beauty mass. According to the definition of x_γ in equation 4.2 these would have to be accounted for in the numerator. However in the definition of $x_\gamma^{\rm obs,\ gen}$ in equation 4.3 these additional jets are not accounted for in the numerator leading to a too low value of $x_\gamma^{\rm obs,\ gen}$. This fact is illustrated in figure 4.16: Here the fraction f_3 of events with three or more jets reconstructed from the output of the Pythia Monte Carlo generator is plotted as a function of $x_\gamma^{\rm obs,\ gen}$. Events at low $x_\gamma^{\rm obs,\ gen}$ tend to have more jets than those at high values of $x_\gamma^{\rm obs,\ gen}$. This effect is most prominent in the direct regime: For $x_\gamma^{\rm obs,\ gen} > 0.6$ all events are 2-jet events. For $x_\gamma^{\rm obs,\ gen} < 0.4$ about 80% are 3-jet events.

The distribution of $y_{\rm JB}$ and $x_\gamma^{\rm obs}$ is shown in figure 4.17. The distribution of y is well described by the Monte Carlo simulation. The distribution of $x_\gamma^{\rm obs}$ shows an overshoot of data with respect to the Monte Carlo simulation. Resolved processes are mainly located at low values of $x_\gamma^{\rm obs}$. This indicates, that the contribution from resolved processes is underestimated in the Monte Carlo simulation.

The distributions in figure 4.16 raise the question if the jet mulitplicities are well described by the Monte Carlo Simulation. Figure 4.18 shows the jet multiplicity for the total sample, the predominantly direct regime with $x_\gamma^{\rm obs} > 0.6$ and the resolved regime with $x_\gamma^{\rm obs} < 0.6$. In the direct regime the number of three jet events seems to be underestimated.

[4] see figure 1.12 on page 20

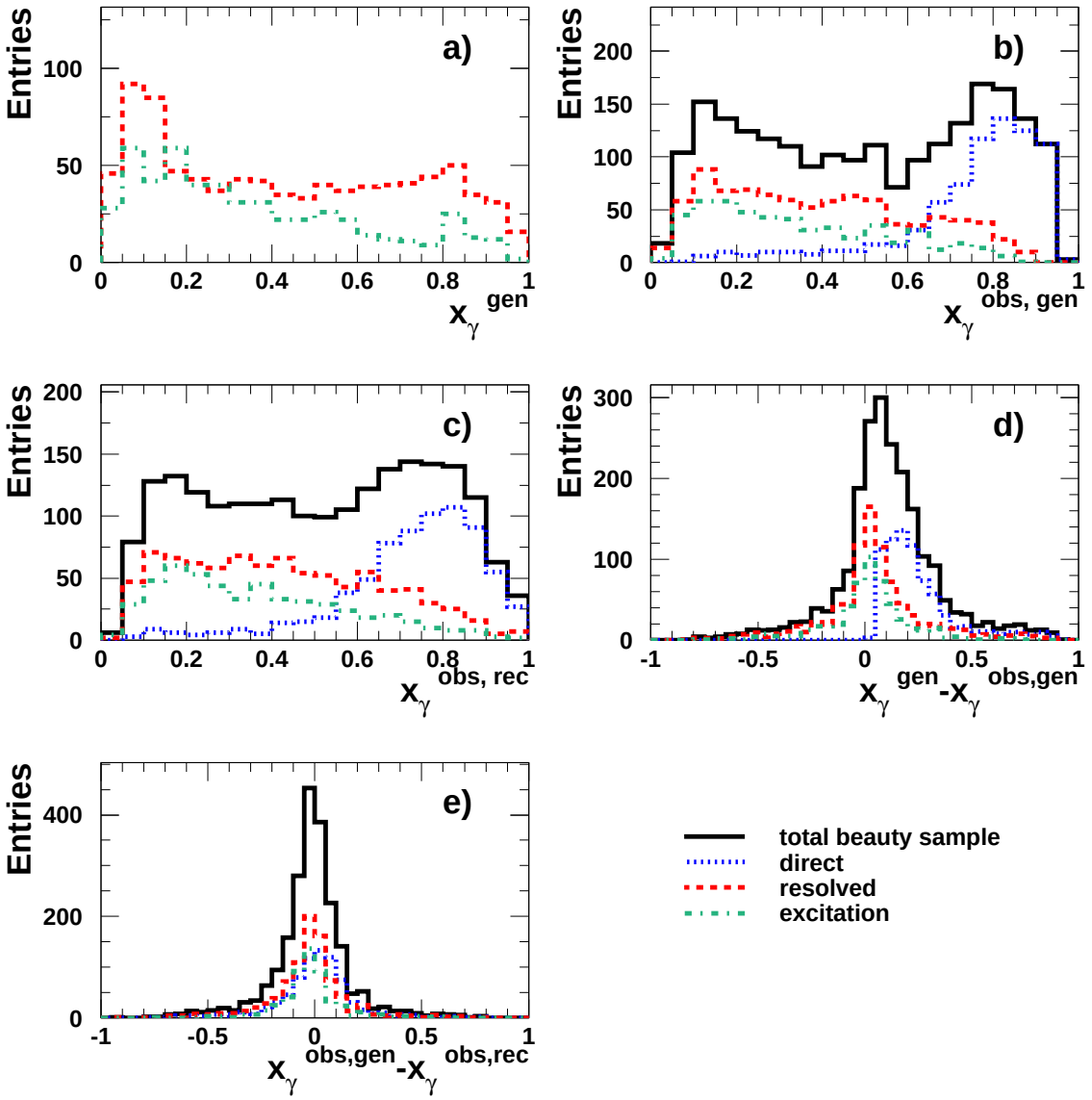

Figure 4.15: Reconstruction of x_γ: Figure a) shows the distribution of x_γ, as generated by the Pythia beauty Monte Carlo Simulation. Figure b) shows the distribution of $x_\gamma^{\text{obs, gen}}$, as reconstructed from the jets defined by the jet algorithm applied to the generated particles. Figure c) shows the distribution of x_γ^{obs}, as reconstructed from the jets defined by the jet algorithm applied to the HFS. Figures d) and e) show the corresponding resolutions. All events in these plots have to pass the final selection of this analysis.

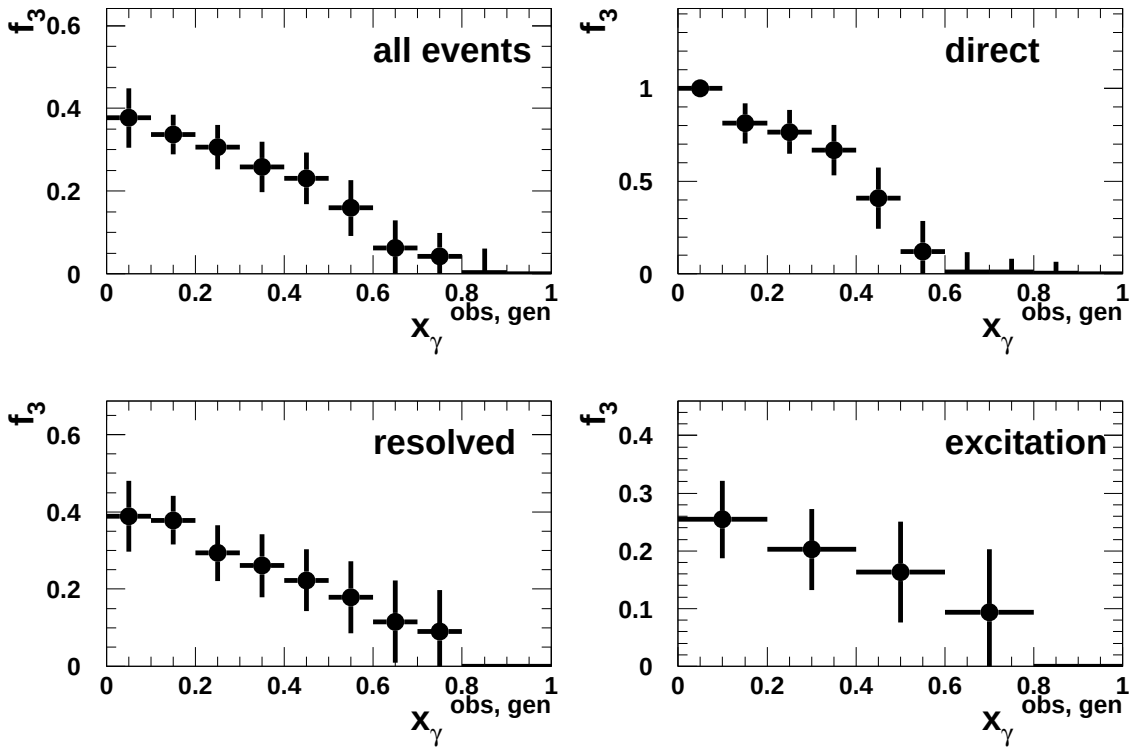

Figure 4.16: Fraction of events with three or more jets as a function of $x_\gamma^{\text{obs, gen}}$ for beauty events generated with the Pythia Monte Carlo generator. All events in these plots have to pass the final selection of this analysis.

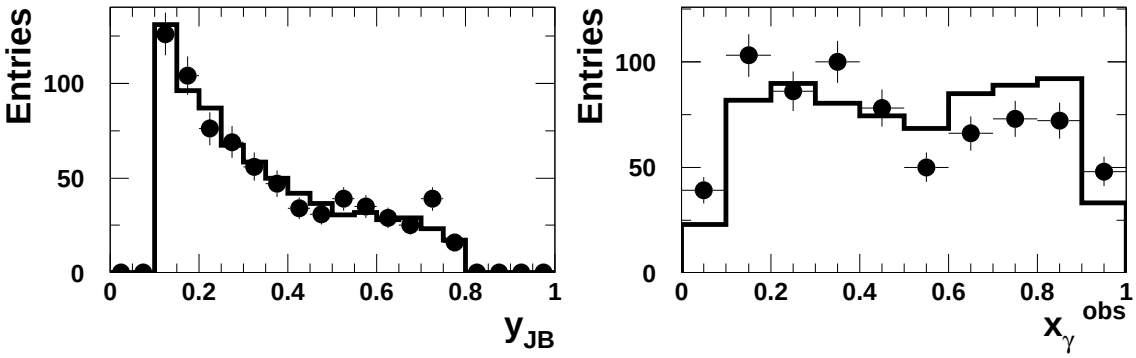

Figure 4.17: Distribution of y and x_γ^{obs}. The events in these histograms have to pass the final selection of the analysis. The relative contributions of beauty, charm and light flavours in the Monte Carlo simulation are taken from the fit result of this analysis, the sum of the contributions is normalised to the data.

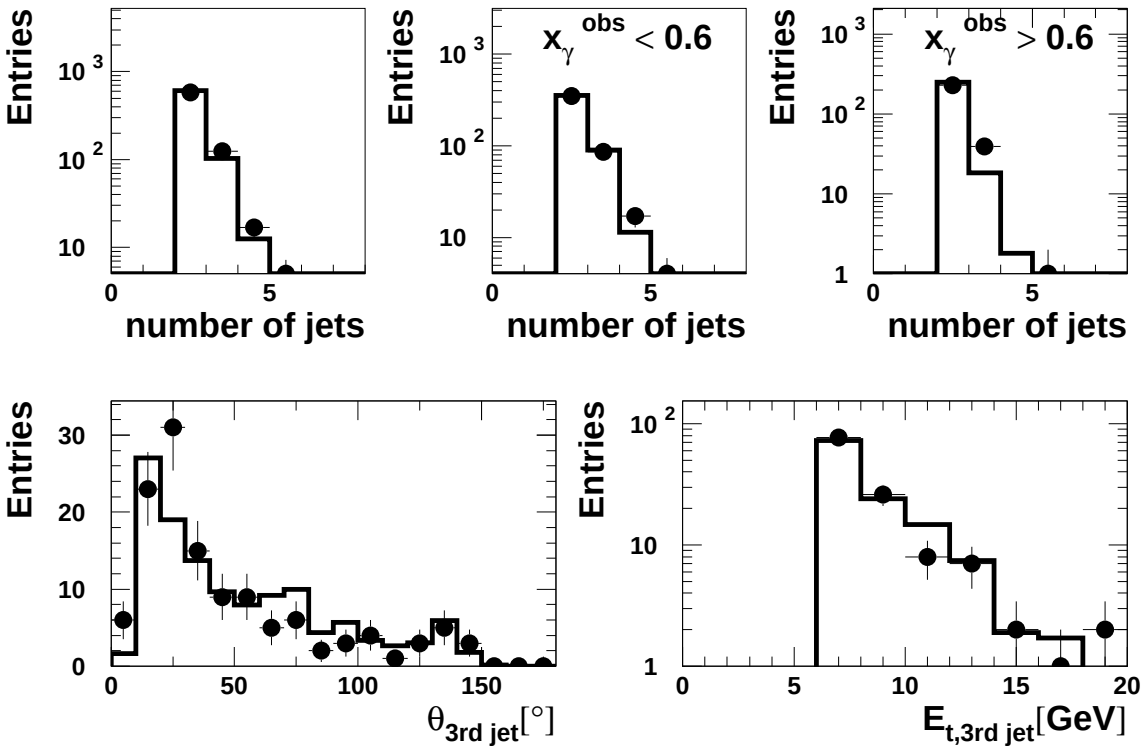

Figure 4.18: Distribution of the number of jets for the total sample and for $x_\gamma^{\rm obs} < 0.6$ and $x_\gamma^{\rm obs} > 0.6$. For the events with three or more jets the polar angle and the transverse energy of the third jet is shown. The events in these histograms have to pass the final selection of the analysis. The relative contributions of beauty, charm and light flavours in the Monte Carlo simulation are taken from the fit result of this analysis, the sum of the contributions is normalised to the data.

For the events with three or more jets the distribution of the azimuthal angle and the transverse energy of the third jet is shown.

4.4 Selection of Photoproduction Events

In photoproduction the incoming electron is scattered under a very low angle and leaves the detector through the beampipe. This means that photoproduction events can be selected by requiring the absence of an identified scattered electron is required. The scattered electron is searched for in the SpaCal. The energy deposit in the SpaCal is collected in clusters. To reject a possible scattered electron the cluster with the highest energy is required to have an energy of less than 8 GeV. If at high Q^2 the scattered electron is misidentified as an HFS object it will contribute to the calculation of $\Sigma_h(E_h - p_{z,h})$. This

would result in $\Sigma_h(E_h - p_{z,h}) = 55\,\text{GeV}$, corresponding to $y = 1$. Therefore $y < 0.8$ is required to eliminate the contribution from high Q^2.

4.5 Trigger Selection

The events can be triggered by several subtriggers. In order to obtain a well defined sample of events and to be able to calculate the trigger efficiency a subset of triggers has to be selected, which still collects a large sample of events. The events in this analysis are mainly triggered by the two subtriggers s16 and s71. s16 combines information from the FMD with information from the zVtx trigger. s71 is designed as a charged current trigger. However it turns out to be efficient as well for dijet analyses [19]. It uses LAr information combined with MWPC tracks and track information from the CJCs. On L2 a φ asymmetry in the barrel part of the LAr is required. The events in the final sample have to triggered by one of those subtriggers.

Subtrigger s16 is defined as

$$\begin{aligned} \text{s16}: \quad & \text{FwdMu\_Val\_Any} \wedge \text{Mu\_FIEC} \wedge \\ & [((\text{zVtx\_mul} == 0 \vee \text{zVtx\_mul} == 3) \wedge \text{zVtx\_T0}) \vee \text{zVtx\_sig}] \\ & \wedge \text{zVtx\_mul} < 7 \wedge (\text{zVtx\_T0} \vee \text{FwdRay\_T0}), \end{aligned}$$

where $\wedge$ denotes a logical AND and $\vee$ denotes a logical OR.

The trigger element FwdMu_Val_Any requires a track in the FMD, which is formed from hits in the ϑ planes of the FMD. Only if a pre- and a post-toroid track within the same octant can be linked, this trigger element is set. This linking module introduces a cut on the maximum bending angle which results in an effective cut on the muon momentum of $\approx 7\,\text{GeV}$. Mu_FIEC requires a coincidence of four hits in the inner region of the forward endcap of the CMD.

The zVtx trigger uses the hits in CIP, COP and FPC to constrain the z vertex of the event. Hits in the chambers are combined to form rays which are extrapolated to the beamline. Here the distribution of the z coordinate of the impact point is filled in a 16 bin zVtx histogram. For a genuine *ep* event this should show a clear peak close to the nominal vertex over an equally distributed combinatorial background. The principle is illustrated in figure 4.19.

zVtx_T0 $\wedge$ FwdRay_T0 requires at least one track in the zVtx trigger or in the FPC. zVtx_mul < 7 rejects high multiplicity proton beam induced background. zVtx_sig requires a significant peak in the zVtx-histogram, while the condition (((zVtx_mul == 0) $\vee$ (zVtx_mul == 3)) $\wedge$ zVtx_T0) requires a small peak.

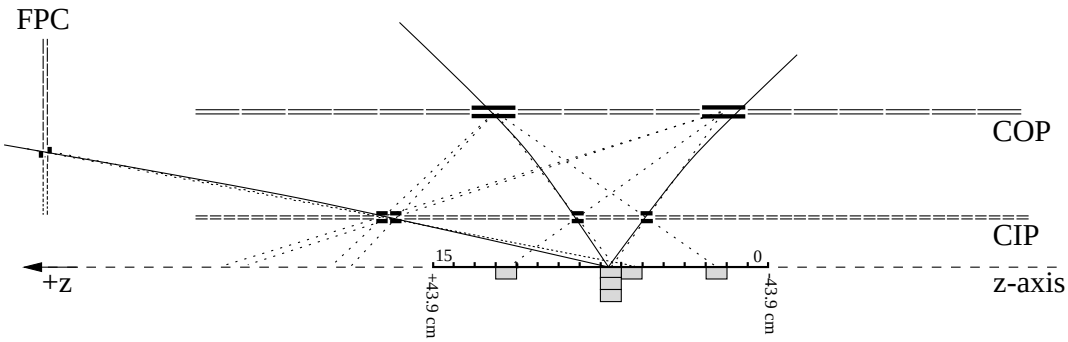

Figure 4.19: Schematic view of the mode of operation of the zVtx trigger and the creation of the zVtx histogram

The geometrical consequences of the trigger elements FwdMu_Val_Any and Mu_FIEC are illustrated in figure 4.20: Events are selected from the preselection of this analysis requiring one muon reconstructed in the FMD and two jets. Figure 4.20 a) shows events that were triggered by subtrigger s71[5], which is independent of the Forward Muon Trigger.

Figure 4.20 b) shows the effect of FwdMu_Val_Any: In the Monte Carlo simulation the acceptance of this trigger element element extends further inward than in the data. This region is excluded by the cut on $\theta_\mu > 10°$.

Figure4.20 c) shows the effect of the trigger element Mu_FIEC. The hitmaps show structures where no events are reconstructed. These structures can be explained by the geometry of the FEC. The FEC has a rectangular hole around the beampipe. The CMD can be opened along a vertical division in the FEC and this region is not instrumented. Furthermore the divisions between the modules of the CMD in the FEC at $y = -135.5$cm, $y = -43.5$cm, $y = +48.5$cm, and $y = +140.5$cm are visible. These structures in the FEC cast a shadow onto the FMD, which is visible in the hitmap. Figure 4.20 d) finally shows the hitmap of events triggered by subtrigger s16. It shows the features of both trigger elements. The structures are more pronounced in the Monte Carlo simulation than in the data.

Alignment

A possible explanation for this difference may be a shift of the FEC with respect to FMD or vice versa during the data taking period. A study of the alignment of the FMD with respect to the FEC shows shifts of the individual octants of the FMD with respect to the FEC of up to 5cm. The study starts with the muon candidates defined in section 4.1. A

[5]These are the same events as in figure 4.8 and are only shown for comparison.

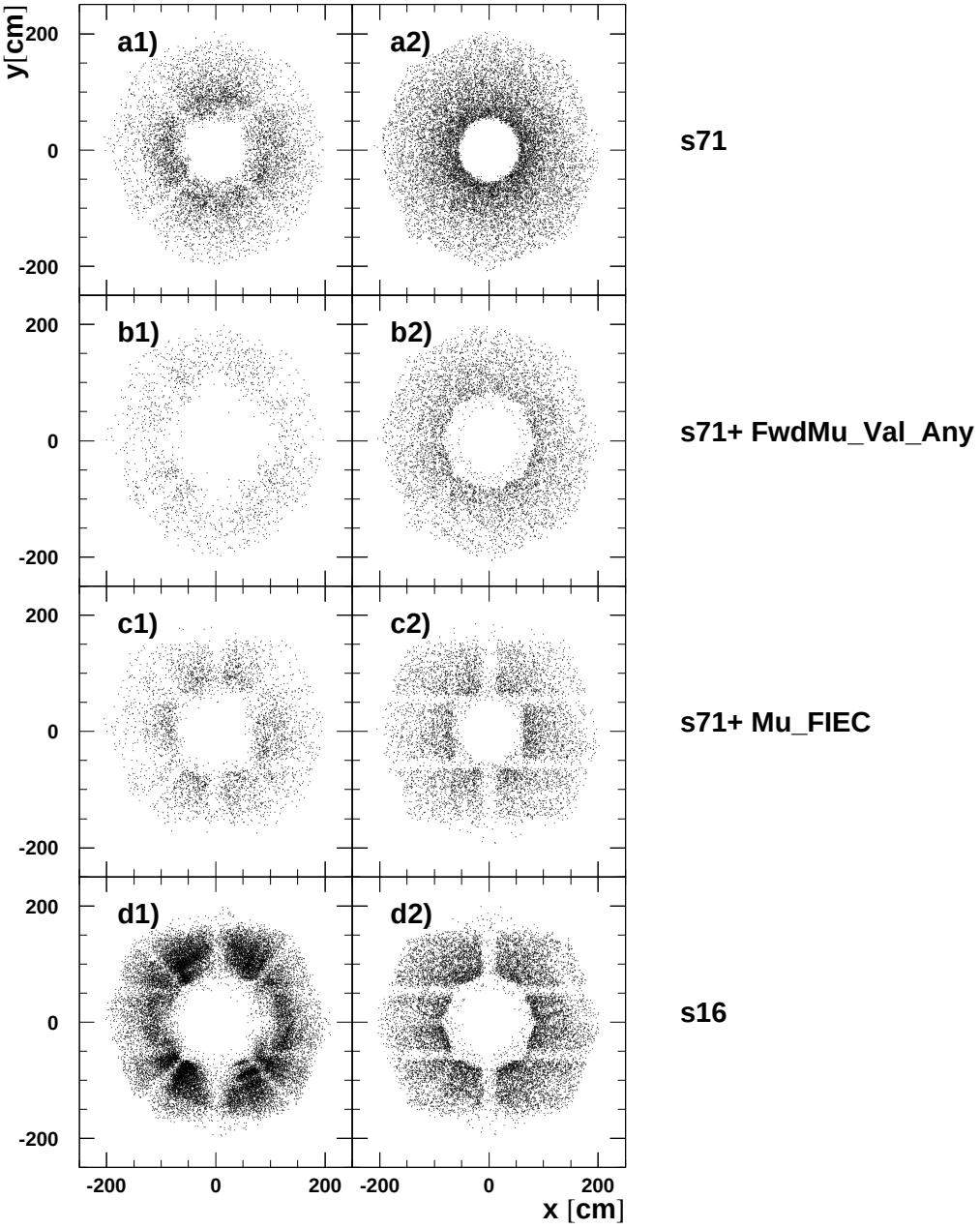

Figure 4.20: xy hitmaps of tracks in the FMD. As in figure 4.8 the events are taken from the preselection of this analysis. The left plots represent the data while the right plots represent the Monte Carlo simulation. The samples a), b) and c) have been triggered by subtrigger s71. Figure b) requires trigger element FwdMu_Val_Any in addition, figure c) Mu_FIEC. The events in figure d) are triggered by subtrigger s16 which among others requires the logical AND of these trigger elements.

track in the FEC is searched for, with a start hit within a radius of 30 cm of the intercept of the muon track with the inner plane of the FEC. This FEC track is then extrapolated as a straight line from the event vertex to the FMD. Here the distance between the start hit of the FMD track and the impact point of the extrapolated FEC track is calculated. The distribution of the difference in x and y is shown in Figure 4.21 individually for each octant of the FMD. The events are selected from the preselection of this analysis requiring a muon reconstructed in the FMD with quality 1 and two jets. The Monte Carlo simulation is a mixture of the samples used in this analysis. The location of these octants is shown in figure 2.8 on page 31.

These shifts observed in figure 4.21 do not show a correlation in the magnitude or in the direction of the shift between single octants.Neither correlated movements of the left side of the FMD with respect to the right side were observed. If any of these shifts happened during the data taking period of this analysis they would be the cause for the washed out structures in the hitmap of the data.

Subtrigger s71 is defined as

$$\begin{aligned} \text{s71}: \quad & \text{LAr\_BR} \wedge \text{DCRPh\_Tc} \wedge (\text{zVtx\_sig} > 1) \wedge \\ & (\text{DCRPh\_T0} \wedge (\text{zVtx\_T0} \vee \text{FwdRay\_T0})) \wedge \text{L2TT}. \end{aligned}$$

For the LAr trigger the LAr is segmented into trigger towers, which point towards the nominal vertex. The energy deposit in up to four of these trigger towers is combined to form a Big Tower. The segmentation of these Big Towers, which are illustrated in figure 4.22, matches the segmentation of the zVtx trigger rays. The trigger element LAr_BR requires a spatial coincidence of at least one Big Tower with an energy deposit of more than 2 GeV with a ray in the zVtx trigger. DCRPh_Tc requires at least three tracks with a transverse momentum of $p_t \gtrsim 400\,\text{MeV}$. On L2 this subtrigger is validated by the L2TT trigger element LAr_BigT_miss. This requires an energy deposit of $\gtrsim$ 2.5 GeV within exactly one Big Tower or exactly two adjacent ones in the central region of the LAr, i.e. for $\vartheta > 20^\circ$ [24, 8].

Level 4 and 5: Here the events are reconstructed and classified into physics classes. The class relevant for this analysis is the high p_t muon class (Class 10). The minimum criteria for a muon in the FMD to be identified in this class are as follows:.

- The track quality as defined in section 4.1.1 should be ≤ 2
- The intersection of the extrapolated track and the z axis as defined in equation 4.1 must lie within $-400\text{cm} < z_{\text{vx},\mu} < 300\text{cm}$

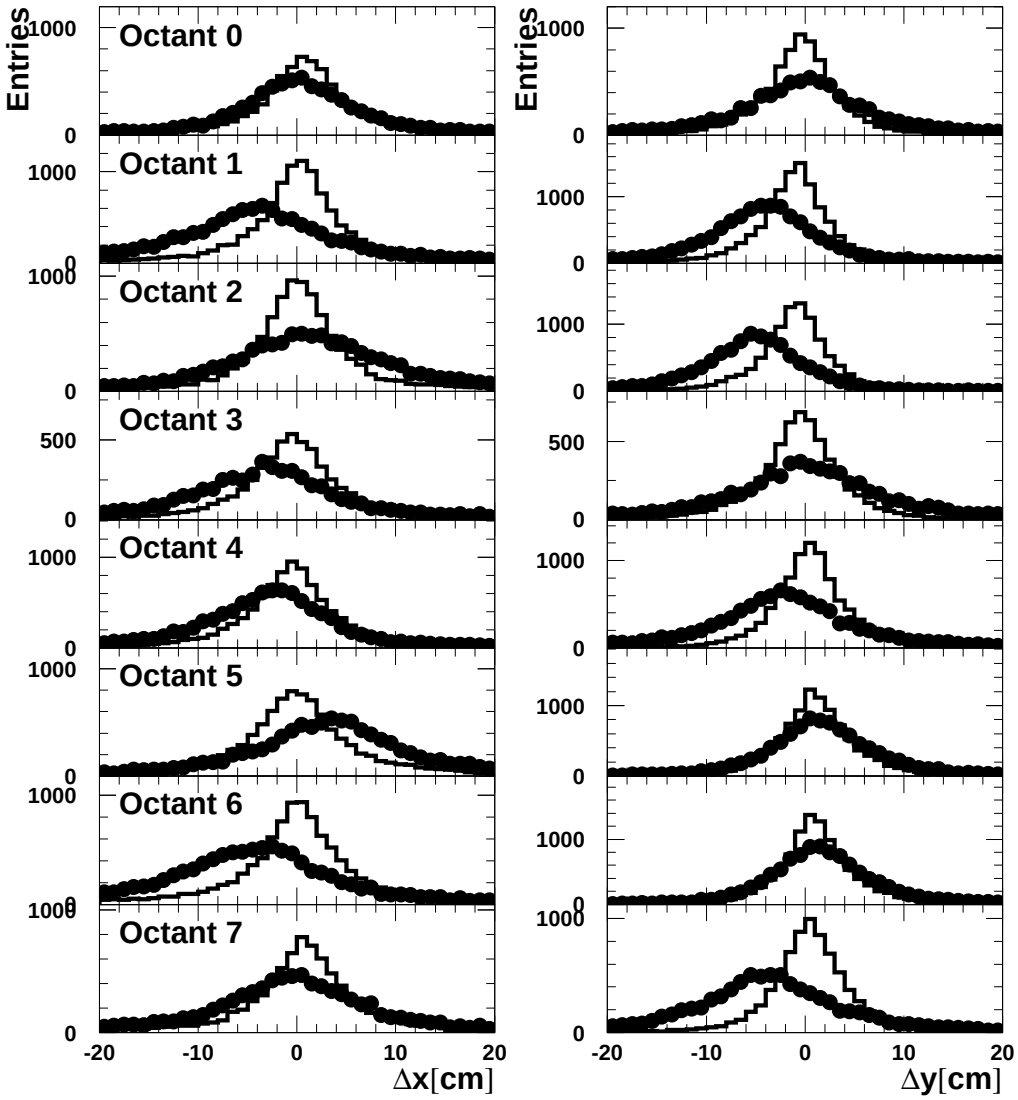

Figure 4.21: Alignment of the FMD with respect to the FEC. The distance between the start hit of the track in the FMD and the impact point of the associated FEC track in the FMD is plotted.

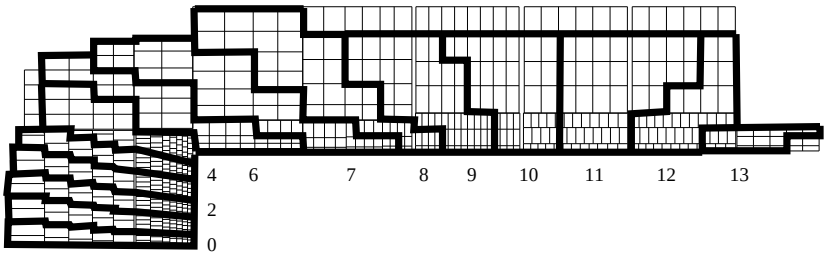

Figure 4.22: Side view of the LAr. The thick lines indicate the borders of the Big Towers.

If the level 5 classification cannot assign an event to any *hard scale* physics class, it will be assigned to the *soft physics* class. These events have to fulfil additional criteria to pass as genuine *ep* events. Events that cannot be assigned to any physics class end up in a special class for not classified events. Events in these two classes are downscaled, i.e. depending on certain event properties only a fraction of the events will be kept. An event weight is assigned to each of these events. All events in this analysis are collected in class 10 and none of them was assigned an L4 weight unequal to 1.

4.6 Trigger Efficiency

If an event passes all trigger levels of H1 it will be permanently recorded. On every level the event has a certain probability to pass. This probability is given by the trigger efficiency which is defined as

$$\epsilon_{\text{Trigger}} = \frac{N_{\text{triggered events}}}{N_{\text{all events}}}.$$

In the simulation the number of all events is known and if the trigger is well modelled in the simulation the trigger efficiency can directly be calculated from the Monte Carlo simulation. The determination of the trigger efficiency from the data is more difficult, because events that are not triggered are lost, and so the number off all events is not known. Here the trigger efficiency is calculated based on a subsample of all events. This subsample is triggered by a monitor subtrigger, which has to be independent of the trigger under investigation. Furthermore it has to be verified, that the trigger under investigation and the monitor trigger accept similar events. This trigger efficiency is calculated for each trigger element separately. The event sample which is used to determine the trigger efficiency has to pass all cuts of the final selection except the cut on the scattered electron cluster. This allows DIS events that were triggered by the SpaCal triggers to enter the sample and enhance the sample of monitor trigger events.

Trigger element	Monitors triggers	$\varepsilon^{\text{Data}}_{\text{Trigger}}$	$\varepsilon^{\text{MC}}_{\text{Trigger}}$
FwdMu_Val_Any	s19, s24, s25, s37, s39, s42, s56, s64, s66, s67, s71, s74, s75, s77, s87	$57.9 \pm 1.6\%$	$68.1 \pm 0.9\%$
Mu_FIEC	s19, s24, s25, s37, s39, s42, s64, s66, s67, s71, s76, s77	$60.4 \pm 1.8\%$	$51.4 \pm 1.0\%$
zVtx conditions	s0, s3, s9, s39	$83.6 \pm 3.5\%$	$92.7 \pm 0.7\%$
Combination		$29.2 \pm 1.7\%$	$32.4 \pm 0.7\%$

Table 4.1: Trigger efficiencies for the contributing trigger elements of subtrigger s16

Trigger element	Monitors triggers	$\varepsilon^{\text{Data}}_{\text{Trigger}}$	$\varepsilon^{\text{MC}}_{\text{Trigger}}$
LAr_BR	s16, s19, s22	$81.8 \pm 1.7\%$	$93.5 \pm 0.8\%$
DCRPh_Tc	s16	$83.1 \pm 1.8\%$	$92.4 \pm 0.9\%$
zVtx_sig > 1	s0, s3, s39	$89.1 \pm 3.0\%$	$94.9 \pm 0.6\%$
L2TT	s10,s19,s22	$33.6 \pm 2.1\%$	$49.0 \pm 1.6\%$
Combination		$20.4 \pm 1.6\%$	$40.2 \pm 1.4\%$

Table 4.2: Trigger efficiencies for the contributing trigger elements of subtrigger s71

4.6.1 Subtrigger s16

The trigger efficiency is determined for each of the contributing trigger elements both in the data and in a beauty Monte Carlo simulation. The trigger efficiency of s16 is the product of the trigger efficiencies of the trigger elements. The resulting efficiencies and the monitor triggers used are listed in table 4.1. The resulting trigger efficiency of s16 is depicted in figure 4.23. The shape of the efficiency is well described in the simulation, the total efficiency in the simulation is however higher than in the data. If the efficiency in the Monte Carlo simulation is scaled globally to be equal to the efficiency in the data, the plots are in good agreement.

4.6.2 Subtrigger s71

As for subtrigger s16 the trigger efficiency is determined for each trigger element and in addition for the L2 condition. The trigger efficiencies of the single trigger elements are listed in table 4.2, the total efficiency of s71 as a function of certain event properties is shown in figure 4.24. For all trigger elements the efficiency is higher in the simulation than in the data. The biggest discrepancy is found for the L2 condition. If the efficiency in the Monte Carlo simulation is scaled globally to be equal to the efficiency in the data,

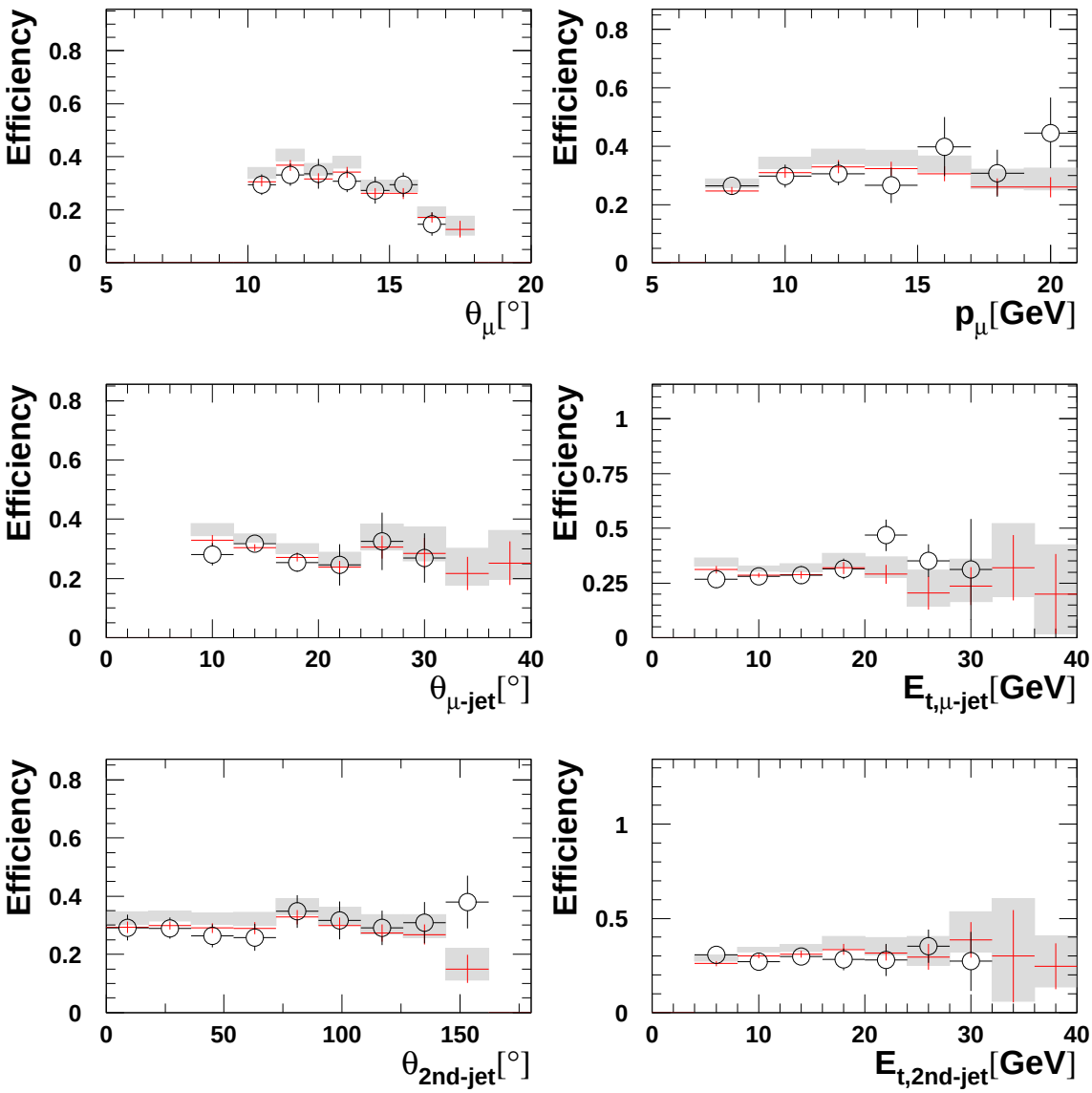

Figure 4.23: Efficiency of s16 as function of muon and jet properties. The circles show the data while the grey boxes show the beauty Monte Carlo simulation with statistical errors. The crosses show the Monte Carlo simulation scaled by 0.292/0.324 which is the global factor between the efficiencies in the data and the Monte Carlo simulation.

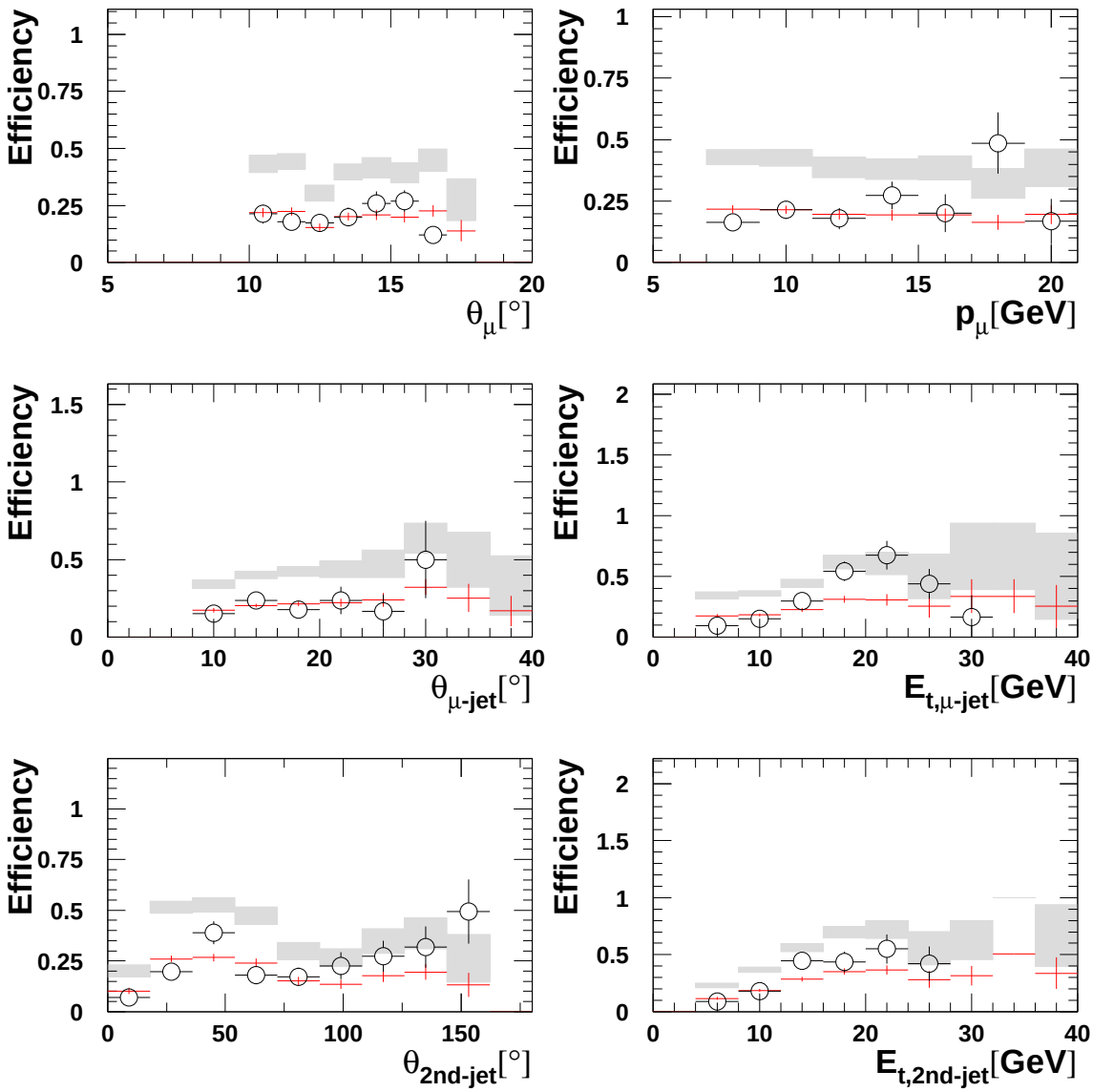

Figure 4.24: Efficiency of s71 as function of muon and jet properties. The circles show the data while the grey boxes show the beauty Monte Carlo simulation with statistical errors. The crosses show the Monte Carlo simulation scaled by 0.204/0.402, which is the global factor between the efficiencies in the data and the Monte Carlo simulation.

the plots are in reasonable agreement.

4.6.3 Combination of the Subtriggers

The resulting data sample has to be triggered by either of the two subtriggers s16 and s71. The trigger efficiency for the logical OR of those two conditions is calculated using

$$\varepsilon_{\text{Trigger}} = 1 - (1 - \varepsilon_{\text{s16}})\,(1 - \varepsilon_{\text{s71}})$$

This amounts to $\varepsilon^{\text{Data}}_{\text{Trigger}} = 43.6 \pm 1.8\%$ and $\varepsilon^{\text{MC}}_{\text{Trigger}} = 59.6 \pm 1.1\%$. The efficiency as function of some kinematic variables is plotted in figure 4.25.

The shape of the trigger efficiency is reasonably described by the Monte Carlo simulation, while the total efficiencies differ significantly. Therefore the trigger efficiency as extracted from the data is used for the determination of the visible cross section.

However, the simulation of the trigger system only enters the analysis at one stage: The p_t^{rel} reference spectra which are used to determine the beauty fraction in the data sample are taken from the Monte Carlo simulation and have to pass the same trigger selection as the data sample. If the trigger efficiency in the data had a different dependence on p_t^{rel} than in the Monte Carlo simulation, the p_t^{rel} spectra for the Monte Carlo simulation would be distorted and the fit result would be wrong. Figure 4.26 shows the resulting trigger efficiency as a function of p_t^{rel}. The efficiency in the Monte Carlo simulation has been scaled gobally to be equal to the total trigger efficiency in the data. Within the statistical errors the trigger efficiencies do not depend on p_t^{rel}. The description of the data by the Monte Carlo simulation is better for subtrigger s16 than for subtrigger s71.

4.6.4 Composition of the Data Set

Out of 727 events that passed the event selection, 452 events were triggered by subtrigger s16, while 380 events were triggered by subtrigger s71. This indicates that the overlap of the subsamples triggered by each of the subtriggers is very small, i.e. those subsamples are almost independent. Only 105 events were triggered by both subtriggers. This can be explained by the trigger efficiencies, mainly concerning the jets triggered by subtrigger s71. As can be seen in figures 4.23 and 4.24, subtrigger s71 is highly sensitive to the kinematics of the jets, the trigger becomes efficient only for high E_t of the jets and if the second jet lies sufficiently within the ϑ acceptance of the L2TT element of $\vartheta_{2^{\text{nd}}\text{ jet}} \gtrsim 20°$. As expected, the subtrigger s16 is only sensitive to the kinematics of the forward muon, and the trigger efficiency of subtrigger s16 shows no dependence on the kinematics of the jets. Figures 4.27 a) - d) show the relative contribution of each subtrigger to the data set as a function of the kinematics of the jets. In the region of low E_t of the jets and of low

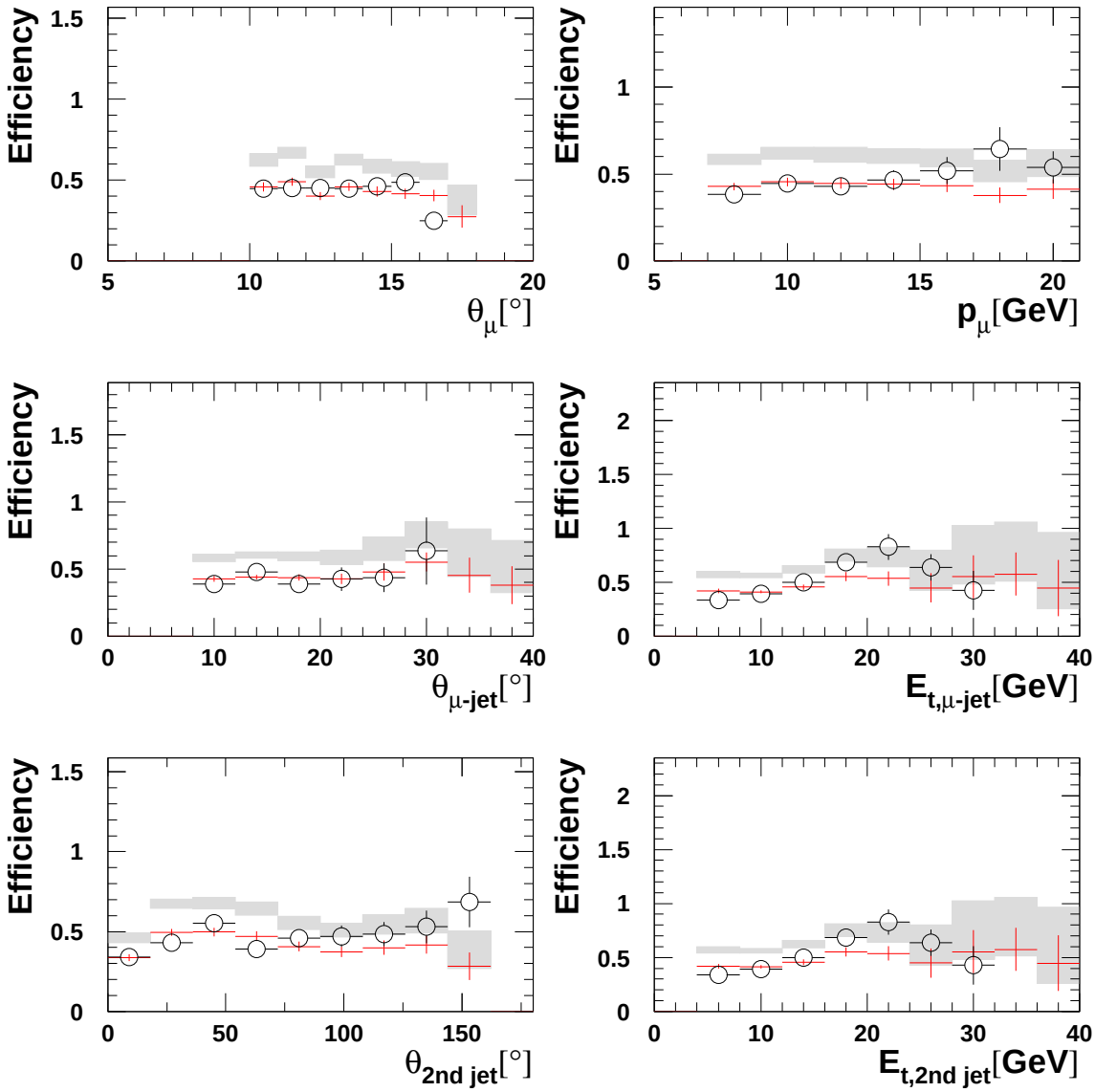

Figure 4.25: Efficiency of the combination of s16 and s71 as function of muon and jet properties.The circles show the data while the grey boxes show the beauty Monte Carlo simulation with statistical errors. The crosses show the Monte Carlo simulation scaled by 0.436/0.596, which is the global factor between the efficiencies in the data and the Monte Carlo simulation.

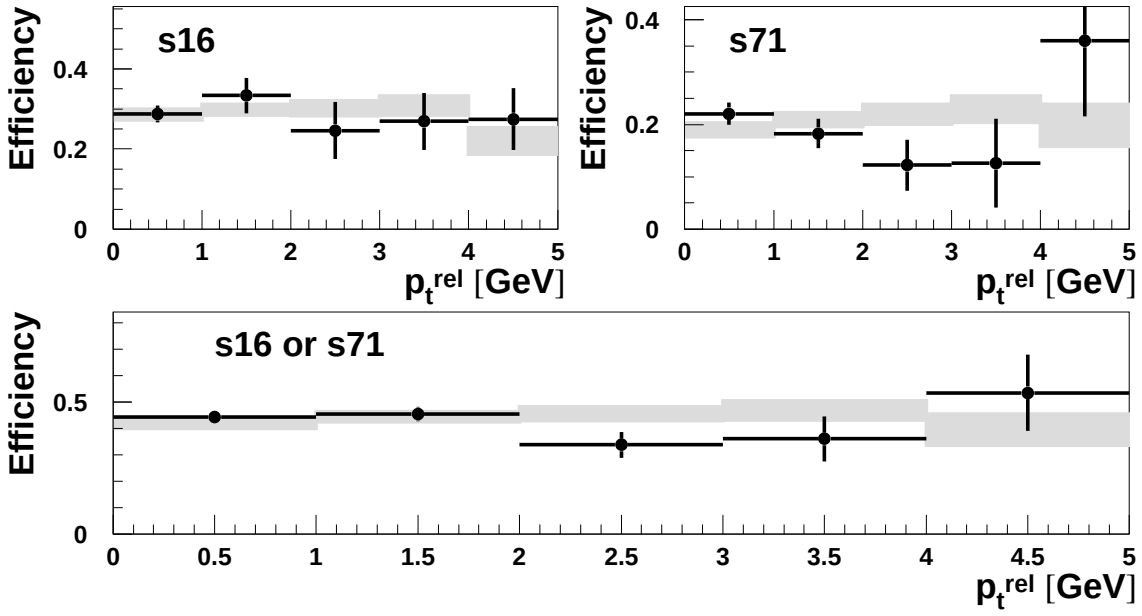

Figure 4.26: Trigger efficiency as a function of p_t^{rel} for subrigger s16, subtrigger s71 and the logical OR of both subtriggers. The points show the data while the grey boxes show the Monte Carlo simulation with statistical errors. The trigger efficiency in the Monte Carlo simulation has been scaled globally by a factor of 0.436/0.596 to be equal to the total trigger efficiency in the data.

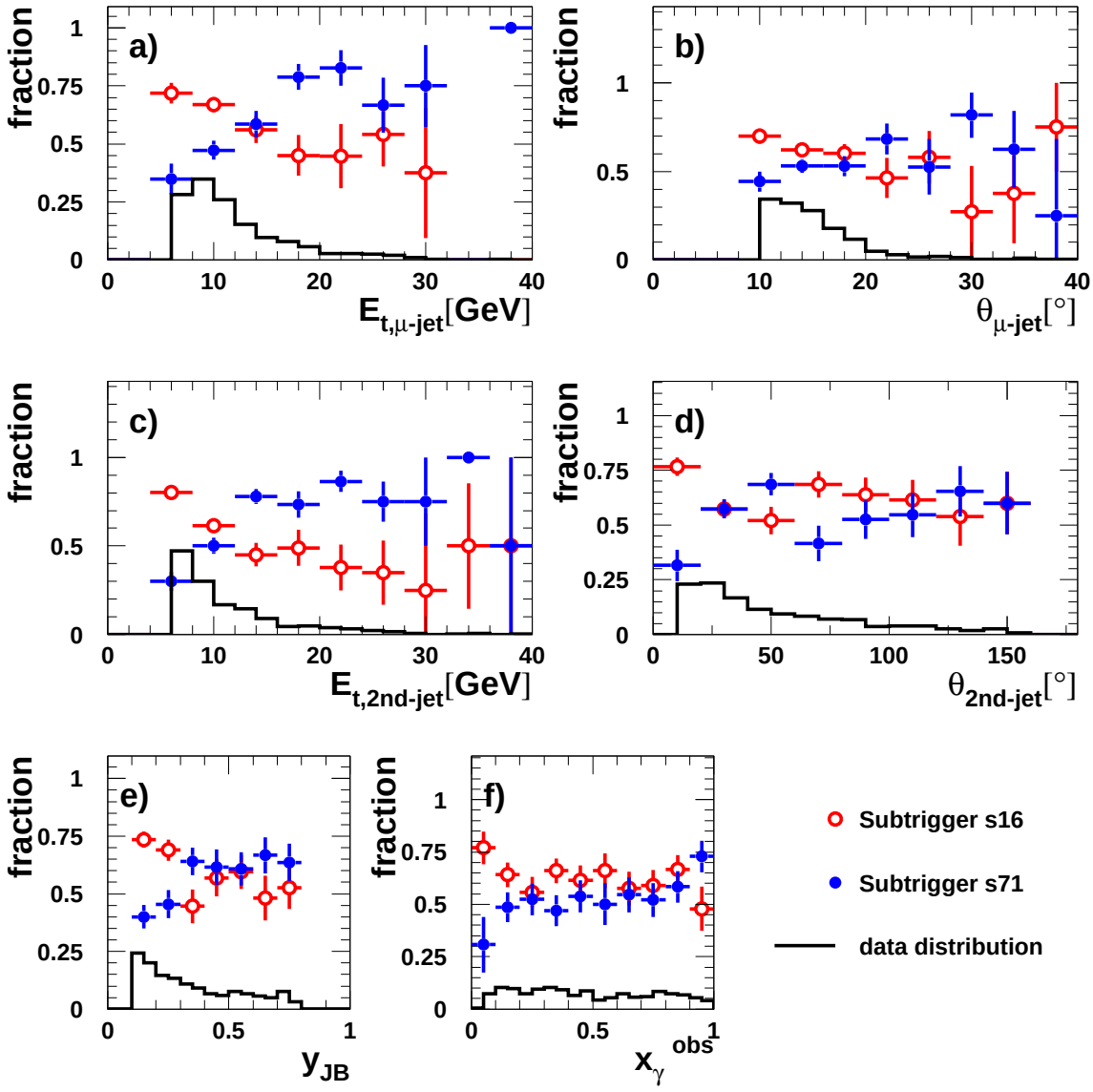

Figure 4.27: Relative contributions of the subtriggers s16 and s71 to the final data set. The scale of the y axis for the data distribution is arbitrary.

ϑ of the second jet the sample is dominated by events triggered by subtrigger s16, while at high E_t subtrigger s71 dominates the sample.

Figures 4.27 b) and d) show that events, where the jets are very forward, are mainly triggered by subtrigger s16. This is reflected in figure 4.27 e): Events with forward jets tend to have low values of y_{JB}, and so the data sample at very low y_{JB} is mainly triggered by subtrigger s16. Resolved processes are expected to contribute more in the forward region than in the central region and this is reflected in figure 4.27 f). At very low x_γ^{obs} the events are dominantly triggered by subtrigger s16, whereas in the direct regime for $x_\gamma^{\mathrm{obs}} \gtrsim 0.8$ subtrigger s71 dominates the sample.

4.7 Luminosity Measurement

The integrated luminosity is calculated by summing up the integrated luminosity of all runs which passed the selection of this analysis. Runs are classified as *good*, *medium* or *poor*, the classification is as follows:

good: All major components are operational. Major components are CJC1-2, LAr, CMD, Luminosity system, SpaCal, BPC, MWPC, FTD.

medium: One or more major components or several minor components are out of operation.

poor: One out of LAr, SpaCal, Luminosity system or the combination of both CJCs and CST is out of operation

Only good and medium runs are used in this analysis. Furthermore the selected runs have to meet the following requirements:

- All detector components vital for this analysis are working
- neither of the triggers was prescaled on L1. Averaged over the whole running period subtrigger s16 had a prescale factor of ≈ 1.05. The runs, where s16 was prescaled, are excluded from the event selection and the luminosity calculation. In these runs s16 had very high prescales and no events are lost by this selection.

The integrated luminosity of each run is calculated by integrating the instantaneous luminosity of the run over the time in which the required components were at their nominal high voltage. $56\mathrm{pb}^{-1}$ were taken by H1 during the 2000 running period for physics analysis. The total integrated luminosity used in this analysis is $\mathcal{L} = 45\mathrm{pb}^{-1}$

cut	number of events without this cut
$10^\circ < \vartheta_\mu < 18^\circ$	1015
$p_\mu > 7\,\mathrm{GeV}$	1376
$\lvert z_{vtx} \rvert < 35\mathrm{cm}$	862
0.1¡y¡0.8	1255
$E_t^{2^{\mathrm{nd}}\ \mathrm{jet}} > 6\,\mathrm{GeV}$	1354

Table 4.3: Overview of the event selection

4.8 Event Selection

The selected events must fulfil the following requirements:

- The events must have a forward muon reconstructed in the FMD with a minimum momentum of 7 GeV and within $10^\circ < \vartheta < 18^\circ$.
- The intersection point of the extrapolated FMD track with the z axis lies within $-400\mathrm{cm} < z_{\mathrm{vx},\mu} < 300\mathrm{cm}$
- One jet with $\vartheta > 10^\circ$, with $E_t > 7\,\mathrm{GeV}$ and with a maximum distance to the muon of $\Delta R < 1.5$ has been reconstructed.
- One additional jet with $E_t > 6\,\mathrm{GeV}$ and $10^\circ < \vartheta < 170^\circ$ has been found.
- The z-component of the reconstructed event vertex must lie within 35 cm of the nominal interaction point.
- The event was triggered by the subtrigger s16 or by s71 and its L2 condition.
- The inelasticity measured by the Jaquet Blondel method lies within $0.1 < y_{\mathrm{JB}} < 0.8$
- No scattered electron was identified.

After all applied cuts and the trigger selection 727 events remain. Table 4.3 shows the applied selection cuts and their effect on the event number.

This event sample will be used in the next chapter to measure the beauty production cross section in the visible range.

Chapter 5

Extraction of the Visible Cross Section

In this chapter the measurement of the beauty production cross section will be described. For the event sample defined in the previous section the contribution of beauty events will be measured and the visible cross section will be extracted.

5.1 Definition of the Visible Cross Section

The cross section measured in this analysis is defined as

$$\sigma^{\text{vis}}(e^+p \to b\bar{b}Xe' \to \ jj\mu Xe') = \frac{f_b N_{\text{data}}}{\varepsilon_{\text{Trigger}}\varepsilon_{\text{rec}}\mathcal{L}}, \tag{5.1}$$

where N_{data} is the number of events that passed the event selection, f_b is the fraction of beauty events in this sample, $\varepsilon_{\text{Trigger}}$ and ε_{rec} are the trigger and reconstruction efficiencies and $\mathcal{L}$ is the integrated luminosity.

The visible range of this measurement is defined by the basic kinematic cuts:

- $p_\mu > 7\,\text{GeV}$,
- $E_t^{\text{Jet}} > 7(6)\,\text{GeV}$,
- $Q^2 < 1\,\text{GeV}^2$,
- $10^\circ < \vartheta_\mu < 18^\circ$,
- $10^\circ < \vartheta_{\text{jet}} < 170^\circ$,
- $0.1 < y_{\text{jb}} < 0.8$

The detector dependent cuts like the cut on the primary vertex z_{vtx}, the intercept of the extrapolated FMD track with the z axis $z_{\text{vx},\mu}$ and the Maltese Cross regions are incorporated as an acceptance correction in the reconstruction efficiency.

5.2 Determination of the Beauty Fraction

An event by event identification of beauty events is not possible with the H1 Detector. Therefore the number of beauty events is extracted on a statistical basis using the method

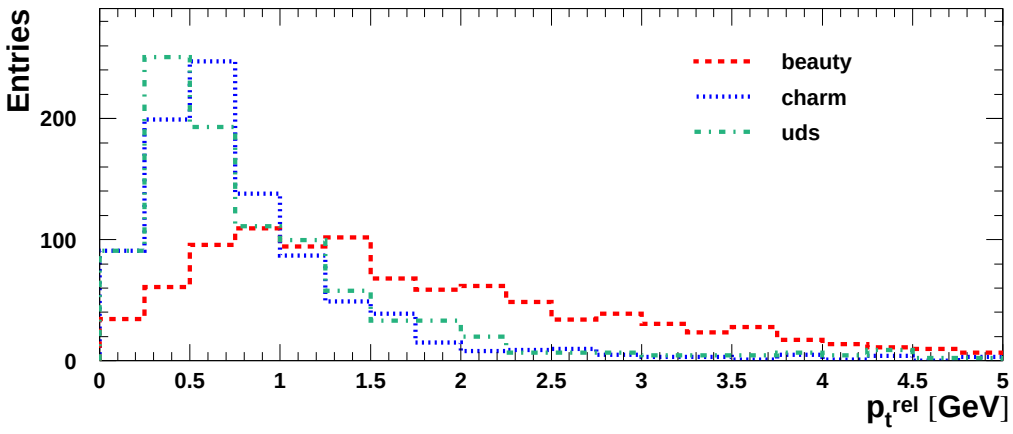

Figure 5.1: The distribution of p_t^{rel} for beauty, charm and light quarks, as predicted by Pythia 6.1

outlined in section 3.5. The mass of the beauty quark is in the range 4.0 GeV $\leq m_b \leq$ 4.5 GeV, the mass of the charm quark is 1.0 GeV $\leq m_c \leq$ 1.4 GeV [16]. The mass difference of beauty and charm quarks has to be transferred into kinetic energy of the decay products. In the centre of mass frame of the decaying hadron this leads to a on average higher momentum of the decay muon for beauty decays than for decays of charm and light quarks. In the lab frame the jet axis approximates the direction of flight of the hadron, which contained the beauty or charm quark. For beauty decays the muons will have higher transverse momenta with respect to the jet axis than for charm and light flavour decays.

5.2.1 Separating Beauty via p_t^{rel}

The beauty contribution in the selected events is extracted using the transverse momentum of the muon relative to the jet axis. A better separation of beauty from charm and light flavours is achieved if the muon is excluded from the calculation of the jet axis. The observable p_t^{rel} is defined in equation 3.1 on page 39. p_t^{rel} is expected to have higher values for beauty than for charm and light flavours. The predicted shapes of the p_t^{rel} spectra from the Monte Carlo simulation are shown in figure 5.1. The beauty sample contains both decay channels $b \to \mu X$ and the cascade decay $b \to cX' \to \mu X$. Initially both channels contribute equally, but the latter is suppressed by the cut on p_μ. The charm sample only contains the channel $c \to \mu X$. Muons from decay of light flavour hadrons, even if they are produced in heavy flavour production, are attributed to the light flavour sample. The p_t^{rel} spectrum for beauty is significantly broader and peaks at a higher value than those for

charm and light flavours. This difference is exploited in the determination of the beauty fraction.

5.2.2 Fit Method

The p_t^{rel} reference spectra from the Monte Carlo simulation are fitted to the data distribution. The fit method is a maximum likelihood fit derived from [7]. The spectra of charm and light flavour are very similar in shape, so a simultaneous fit of all three flavours is not possible. Thus the fraction of light flavours is fixed to 28.6%. This value is based on an extrapolation of a previous H1 measurement [5] into the kinematic region of this analysis. In the previous analysis a measurement of the visible beauty cross section in the central region was performed. The fit result of this analysis yields estimates for the charm and light flavour contributions [30]. The fractions are extrapolated into the kinematic region of this analysis, using Pythia 6.1. The fraction of light flavours is then fixed to the fraction obtained by the extrapolation. The uncertainty arising from this procedure will be discussed in section 5.5.1.

In the fit the fraction of light flavours stays fixed while the fractions of beauty and charm are varied. When the likelihood of the fit to the data is maximised, the corresponding charm and beauty fractions then represent the best fit result. The fit yields

$$\begin{array}{lllll} f_b & = 21.8 \pm 4.3 & \% \Longrightarrow 148 \pm 29 & \text{events} & \\ f_c & = 49.2 \pm 5.5 & \% \Longrightarrow 334 \pm 37 & \text{events} & (5.2) \\ f_{uds} & = 28.6 & \% \Longrightarrow 194 & \text{events}, & \end{array}$$

where the error is the statistical error resulting both from the finite statistics of the data and the uncertainty of the fit. The distribution of the data and the result of the fit including the reference spectra are shown in figure 5.2. The data are well described by the fit, with $\chi^2/(\text{n.d.o.f}) = 18.3/20$. The stability of this fit has been tested by variation of the number of bins and the range of the fit. The variation of the fit result is within the statistical error of the fit.

5.3 Reconstruction Efficiency

The reconstruction efficiency ε_{rec} accounts for all inefficiencies in the reconstruction of an event. It is calculated from the beauty Monte Carlo simulation by

$$\varepsilon_{\text{rec}} = \frac{N_{\text{rec}}}{N_{\text{gen}}},$$

where N_{rec} is the number of Monte Carlo events that passed the same selection as the data except the trigger selection. N_{gen} is the number of generated Monte Carlo events

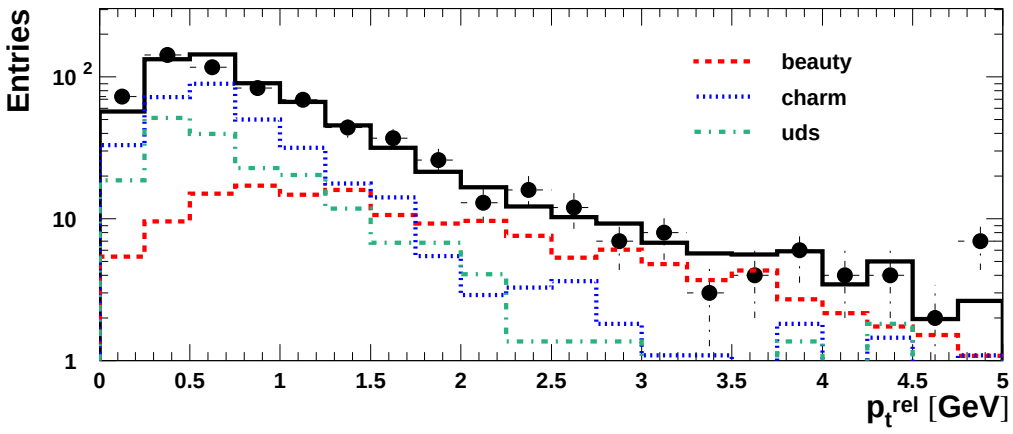

Figure 5.2: The result of the p_t^{rel} fit

in the same sample that lie within the visible range of this analysis. The selection of these events is based on the output of the event generator. The jet algorithm is applied on all stable particles that are produced as the final state of the Monte Carlo generator. Stable in this sense means that the life time of the particle has to exceed $\tau > 10^{-8}$s. The reconstruction efficiency accounts for inefficient reconstruction of the final state, .i.e. the muon and the jets and migration effects at the boundaries of the covered phase space. The total reconstruction efficiency is $\varepsilon_{\text{rec}} = 73\%$.

5.4 Visible Cross Section

The visible cross section as defined in section 5.1 can now be calculated. The total trigger efficiency was derived from the data in section 4.6. The visible cross section is

$$\sigma^{\text{vis}}(e^+p \to b\bar{b}Xe' \to \ jj\mu Xe') = 11.0 \pm 2.2\text{pb}. \tag{5.3}$$

The statistical error contains the statistical error as calculated in equation 5.2 and the statistical error of the trigger efficiency added in quadrature.

5.5 Systematic Uncertainties

The measurement of the visible cross section depends both directly and indirectly on many measured and reconstructed quantities. The influence of uncertainties of these quantities is described in this chapter and finally the total systematic error of the measurement will be estimated.

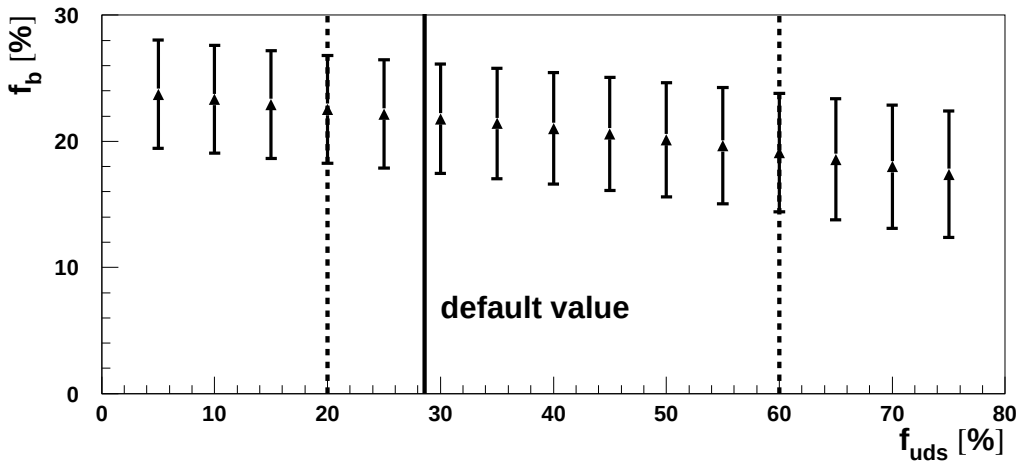

Figure 5.3: Influence of the fractions of light flavours on the measured beauty fraction. The solid line indicates the default value of the fraction of light flavours. The dashed lines show the boundaries in which the fraction of light flavours is varied.

5.5.1 Light Flavours

The fraction of light flavours is calculated using an extrapolation of a previous measurement [5, 30] into a different kinematic region. Although the Pythia Monte Carlo generator is expected to describe the data reasonably well, such large extrapolations are subject to large uncertainties. Therefore the effect of variations of the used fraction of light flavours is evaluated. The measured visible cross section is proportional to the measured beauty fraction obtained by the p_t^{rel} fit. All other quantities in the definition of the visible cross section in equation 5.1 do not depend on the fraction of light flavours. Thus to evaluate the influence of the light flavours fraction on the measurement, it is sufficient to redo the p_t^{rel} fit for different fractions of light flavours. Figure 5.3 shows the dependence of the measured beauty fraction as a function of the fraction of light flavours used in the fit.

If the shapes of the distributions for charm and light flavours were equal, the fit result should not depend on the choice of f_{uds}. The figure however shows a weak linear dependence of the measured beauty fraction on the fraction of light flavours. This can be understood from figure 5.1. The p_t^{rel} distribution of light flavours has a slightly more pronounced tail at large values of p_t^{rel} than the distribution for charm. This difference is too small to be exploited in a fit given the limited statistics of the data sample. However it is big enough to make the measurement dependent on the choice of f_{uds}: If f_{uds} is reduced this is compensated by the fit mainly by an increase of the charm fraction but as well by a slight increase of the beauty fraction, which accounts for the beauty-like tail of the p_t^{rel} spectrum of light flavours. It is assumed that the fraction of light flavours can

vary between 20% and 60%. This leads to a relative uncertainty of the measured beauty fraction and hence of the visible cross section of $^{+4.4\%}_{-14\%}$.

5.5.2 Hadronic Scale

The total energy scale of the LAr is only known to a precision of ±4%. This uncertainty would lead to migrations at the E_t threshold of this measurement. To evaluate this effect, the visible cross section as calculated on the generator Monte Carlo level is recalculated, with the energy of all jets scaled up or down by 4%. The relative variation of the obtained visible cross section is taken as the relative error of the measured visible cross section. The result is a $^{+7\%}_{-8\%}$ error on the measured cross section.

5.5.3 Trigger Dependence

It was shown in section 4.6.4, that the subtriggers contribute differently to the data set. Therefore it is checked that the almost disjoint samples analysed separately produce similar results. The analysis was rerun with data accepted only by one of the subtriggers. The results are

$$\begin{aligned} \sigma^{\text{vis}}_{\text{s16}} = &\quad 8.7 \quad \pm 2.6\text{pb} \\ \sigma^{\text{vis}}_{\text{s71}} = &\quad 10.9 \quad \pm 3.3\text{pb} \end{aligned}$$

These results agree well within the statistical error with the result obtained in equation 5.3. Therefore no systematic error is quantified for this effect.

5.5.4 Reconstruction Efficiency

The reconstruction efficiency is extracted directly from the Monte Carlo simulation. The reconstruction of jets is expected to be well described in the simulation. The biggest uncertainty is expected to come from the reconstruction of the muon in the FMD. However the reconstruction efficiency is very difficult to extract from the data. For this a monitor sample of muons would have to be defined where the cuts on p_μ and ϑ_μ can be applied. In the forward region these measurements would have to be performed using the FTD. However the bad momentum resolution of the FTD would introduce uncertainties that are very difficult to control. Therefore the reconstruction efficiency in the FMD obtained from the Monte Carlo simulation cannot be verified by an independent measurement. A relative uncertainty of the reconstruction efficiency of 7% is assumed.

5.5.5 Luminosity Measurement

The luminosity measurement for the running period of this analysis is known to be accurate to ±1.5%. This is the relative uncertainty for the cross section measurement.

5.5.6 Total Systematic Uncertainty

The main systematic uncertainties are summarised in table 5.1. The uncertainties are added in quadrature to calculate the total systematic uncertainty.

variation	relative influence on σ_{vis} in %
f_{uds} by $^{+31.4\%}_{-8.6\%}$	$^{+4.4}_{-14}$
hadronic scale by ±4%	$^{+7}_{-8}$
reconstruction efficiency	±7
Luminosity measuerment	±1.5
Total systematic uncertainty	$^{+10.9}_{-17.6}$

Table 5.1: Summary of the systematic uncertainty

Combining both the statistic and the systematic uncertainty of the measurements the visible cross section is

$$\sigma^{\text{vis}}(e^+p \to b\bar{b}Xe' \to\ jj\mu Xe') = \left[11.0 \pm 2.2(\text{stat.})^{+1.2}_{-1.9}(\text{syst.})\right] \text{pb}. \tag{5.4}$$

5.6 Comparison to QCD Predictions and Other Results

The measured visible cross section in equation 5.4 can be compared with the prediction obtained by the Pythia Monte Carlo generator. This yields a visible cross section of 5.2pb, which is 2 standard deviations below the measured cross section. The measured visible cross section is about twice as high as the Pythia Monte Carlo prediction. Cascade predicts a visible cross section of 4.6pb.

The fact that the predicition by Cascade is lower than the Pythia predicition may be attributed to the missing resolved and excitation processes in Cascade. Figure 5.4 a) shows the distribution of $x_\gamma^{\text{obs, gen}}$ as reconstructed from the jets formed from the generator output, see section 4.3 for details. Cascade fails to provide events at low $x_\gamma^{\text{obs, gen}}$ which contribute strongly in this analysis, as can be seen in figure 4.17 on page 59. Resolved processes result in a boost of the final state into the forward region. Without resolved processes Cascade cannot provide this boost and this is compenstated by a steeper y distribution as can be seen in 5.4 b).

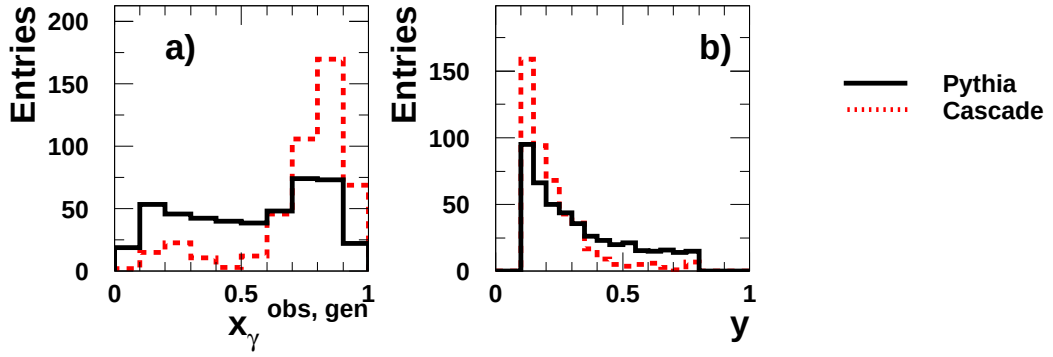

Figure 5.4: Comparision the event kinematics for the selection of this analysis as predicted by Pythia and Cascade. Figure a) shows the distribution of $x_\gamma^{\text{obs, gen}}$ as reconstrucet from the jets formed from the generator output. Figure b) shows the distribution of the inelasticity y. The events in this plots have to lie within the visble range of this analysis.

No measurement exists which can be compared directly with this measurement. But still this measurement can be set into the context of other beauty measurements performed at HERA:

Figure 5.5 shows the measurement performed by H1 in the central rapidty region [5]. For the lowest value of $p_t^\mu = 2.9\,\text{GeV}$ and for the highest value of $\eta_\mu = 0.85$ these measurements are somewhat above the theoretical prediction. The pseudorapidity range of the muon in this analysis is $1.8 < \eta_\mu < 2.4$. The p_t^μ range in this analysis extends further down as well. In the central analysis the muon has to fulfil $p_t^\mu > 2.5\,\text{GeV}$, while in this analysis the minimum p_t^μ ranges from 1.2 GeV for $\vartheta_\mu = 10°$ to 2.2 GeV for $\vartheta_\mu = 18°$. Although the selection criteria in both analyses are different it is noticeble, that the result of this analysis is compatible with the trends seen in in the shapes of the differential cross sections in figure 5.5.

In figure 5.6 some kinematic features of this analysis and the H1 analysis in the central region are compared using the Pythia beauty Monte Carlo generator. Figure 5.6 a) shows the pseudorapidity of the beauty-quark which was matched to the muon jet. The beauty quark in this analysis is produced much more forward than in the central analysis. Figure 5.6 b) shows the distribution of x_γ^{obs}, showing that in the kinematic region of this analysis the relative contribution of resolved and excitation proceses is much higher than in the central region. Figure 5.6 c) shows the distribution of the transverse momentum of the beauty-quark . The shapes are in very good agreement, which is due to the fact, that the jet selection is the same for both analyses.

Zeus has published a result for forward beauty production [12] where some selection criteria are different than in this analysis: $1.48 < \eta_\mu < 2.3$, $p^\mu > 4\,\text{GeV}$, $p_t^\mu > 1\,\text{GeV}$

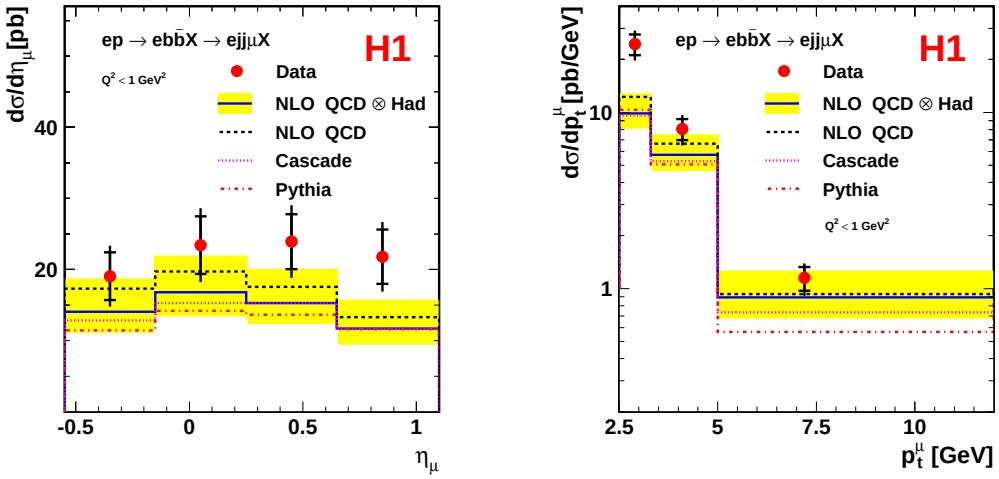

Figure 5.5: Differential cross sections $d\sigma^{\text{vis}}/d\eta_\mu$ and $d\sigma^{\text{vis}}/dp_t^\mu$ as measured by H1 in [5]

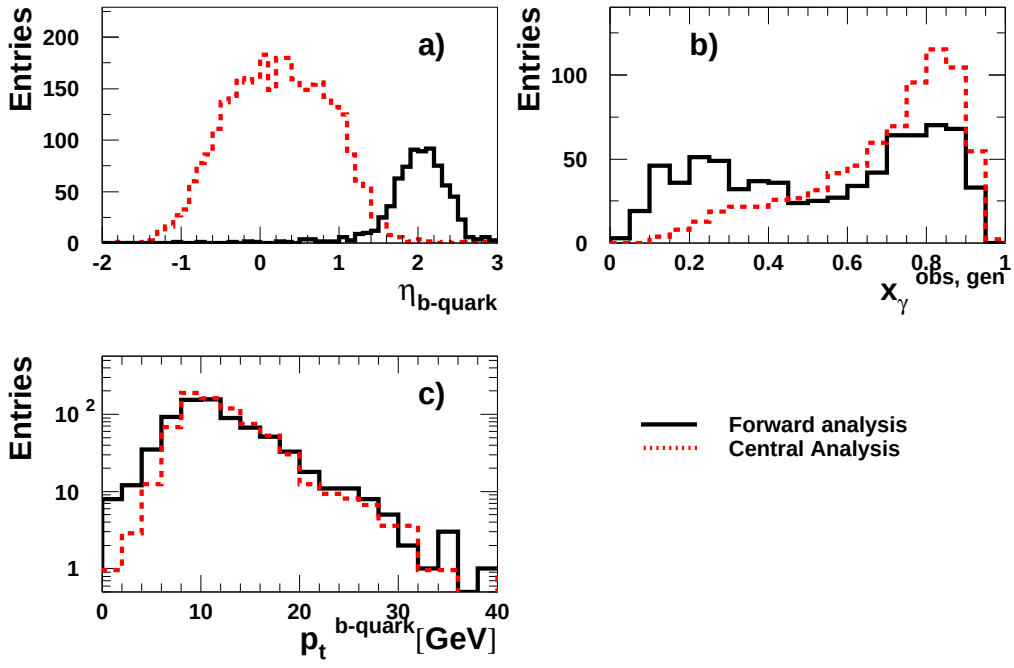

Figure 5.6: Comparision of the kinematics as computed by the Pythia Monte Carlo generator in this analysis and the kinematics of the published central H1 analysis [5]. The events in this plots have to lie within the visible range of the cited analysis.

and $0.2 < y_{\mathrm{JB}} < 0.8$. The beauty fraction was measured to be 21%. The measured cross section is $\sigma^{\mathrm{vis}} = \left[16.6 \pm 3.3(\mathrm{stat.})^{+2.9}_{-4.6}(\mathrm{syst.})\right]$ pb, compared with a NLO prediction of $\sigma^{\mathrm{vis}}_{\mathrm{NLO}} = 6.5^{+2.8}_{-1.6}$pb. As well here the measured cross section is significantly higher than the theoretical prediction.

Chapter 6

Summary and Outlook

The first measurement of the cross section for forward beauty photoproduction at H1 was presented. Events were selected with two jets and a forward muon reconstruced in the FMD. One jet has to be associated to the muon. The data was selected from data taken in the year 2000 corresponding to an integrated luminosity of 45pb^{-1} at a centre of mass energy of 319 GeV.

The main challenge of this analysis was the identification of the decay muon using the Forward Muon Detector (FMD). Hard cuts on the momentum and the azimuthal angle of the muon had to be applied to ensure a reliable description of the data by the Monte Carlo simulation.

The beauty fraction in the event sample has been extracted using the p_t^{rel} method: The transverse momentum of the muon relative to the axis of the associated jet is larger in beauty events than in charm or light flavour events. Using a fit of simulated p_t^{rel} reference spectra to the data the beauty fraction in the sample was determined and the beauty cross section in the visible range of this analysis was extracted.

The mesasured cross section is twice as high as the Pythia Monte Carlo prediction, corresponding to two standard deviations of the measurement. This is consistent with previous measurements of beauty production at HERA in other kinematic regions, which have shown significant excesses of the measured cross sections with respect to the theoretical predictions.

Outlook

In the running period of this analysis the performance of the H1 detector was limited by the inaccurate track reconstruction from the Forward Tracking Detector (FTD). The information from the FTD was therefore not used in this analysis. In the major upgrade program for HERA II carried out in the years 2001-2002 a new forward tracker was installed. In addition a Forward Silicon Tracker (FST) was installed, covering the angular

range $8^\circ \lesssim \vartheta \lesssim 18^\circ$. Combined with muon identification from the FMD and Central Muon Detector (CMD) a much more accurate muon identification will be possible. The FST will allow for life-time signatures to be used for the identification of beauty and charm hadrons. Combining p_t^{rel} and lifetime signatures as two independent variables reduces the statistical error of the measurement, as was proven in [28]. Currently a new method of muon identification in the LAr is under development, allowing muon identification within jets using neural networks [32]. This will provide reliable muon identifcation at lower momenta.

A substantial increase of integrated luminosity is furthermore expected until the end of the HERA running in the year 2007, which will provide enough data for reduced statistical errors and single and double differential measurements in the central and as well in the forward region. These measurements are expected to boost the understanding of the QCD effects which can be tested in the field of beauty production.

Bibliography

[1] I. Abt et al. The H1 Detector at HERA. *Nucl. Instrum. Meth.*, A386:310–347, 1997.

[2] C. Adloff et al. Measurement of D* Meson Cross Sections at HERA and Determination of the Gluon Density in the Proton Using NLO QCD. *Nucl. Phys.*, B545:21–44, 1999, hep-ex/9812023.

[3] C. Adloff et al. Measurement and QCD Analysis of Neutral and Charged Current Cross Sections at HERA. *Eur. Phys. J.*, C30:1–32, 2003, hep-ex/0304003.

[4] Q. R. Ahmad et al. Measurement of the Charged Current Interactions Produced by B-8 Solar Neutrinos at the Sudbury Neutrino Observatory. *Phys. Rev. Lett.*, 87:071301, 2001, nucl-ex/0106015.

[5] A. Aktas et al. Measurement of Beauty Production at HERA Using Events with Muons and Jets. 2005, hep-ex/0502010.

[6] Guido Altarelli and G. Parisi. Asymptotic Freedom in Parton Language. *Nucl. Phys.*, B126:298, 1977.

[7] R. Barlow and C. Beeston. Fitting Using Finite Monte Carlo Samples. *Comp. Phys. Com. 77*, page 219, 1993.

[8] J.C. Bizot et al. Pure LAr calorimeter L2TT trigger elements. Internal Note H1-07/99-574, H1 collaboration, July 1999.

[9] R. Brun, F. Bruyant, M. Maire, A. C. McPherson, and P. Zanarini. Geant3. 1987. CERN-DD/EE/84-1.

[10] S. Catani, Yuri L. Dokshitzer, M. H. Seymour, and B. R. Webber. Longitudinally Invariant K(t) Clustering Algorithms for Hadron Hadron Collisions. *Nucl. Phys.*, B406:187–224, 1993.

[11] S. Catani, F. Fiorani, and G. Marchesini. Qcd coherence in initial state radiation. *Phys. Lett.*, B234:339, 1990.

[12] S. Chekanov et al. Bottom Photoproduction Measured Using Decays Into Muons in Dijet Events in e p collisions at s**(1/2) = 318GeV. *Phys. Rev.*, D70:012008, 2004.

[13] S. Chekanov et al. Measurement of Charm Fragmentation Ratios and Fractions in Photoproduction at HERA. 2005, hep-ex/0508019.

[14] Marcello Ciafaloni. Coherence Effects in Initial Jets at Small q^2/s. *Nucl. Phys.*, B296:49, 1988.

[15] Yuri L. Dokshitzer. Calculation of the Structure Functions for Deep Inelastic Scattering and e+ e- Annihilation by Perturbation Theory in Quantum Chromodynamics. (in russian). *Sov. Phys. JETP*, 46:641–653, 1977.

[16] S. Eidelman et al. Particle Physics Booklet, 2004.

[17] S. Eidelman et al. Review of Particle Physics. *Physics Letters B*, 592:1+, 2004.

[18] Stephen D. Ellis and Davison E. Soper. Successive Combination Jet Algorithm for Hadron Collisions. *Phys. Rev.*, D48:3160–3166, 1993, hep-ph/9305266.

[19] Lars Finke. private communication.

[20] Philipp Fleischmann. *Elastic J/ψ production at HERA*. PhD thesis, Universität Hamburg, 2004.

[21] Stefano Frixione, Paolo Nason, and Bryan R. Webber. Matching NLO QCD and Parton Showers in Heavy Flavour Production. *JHEP*, 08:007, 2003, hep-ph/0305252.

[22] Stefano Frixione and Bryan R. Webber. Matching NLO QCD Computations and Parton Shower Simulations. *JHEP*, 06:029, 2002, hep-ph/0204244.

[23] V. N. Gribov and L. N. Lipatov. Deep Inelastic *ep* Scattering in Perturbation Theory. *Sov. J. Nucl. Phys.*, 15:438–450, 1972.

[24] Beate Heinemann. *Measurement of Charged Current and Neutral Current Cross Sections in Positron-Proton Collisions at $\sqrt{s} \simeq 300$ GeV*. PhD thesis, Universität Hamburg, 1999.

[25] Kirstee Louise Hewitt. *Elastic J/ψ Photoproduction and the Detection and Triggering of Muons at low $W_{\gamma p}$ using the H1 Detector*. PhD thesis, University of Birmingham, March 1998.

[26] F. Jacquet and A. Blondel. Detection and Study of the Charged Current event. In U. Amaldi, editor, *Study of an ep-Facility for Europe*, pages 391–396. DESY, August 1979.

[27] H. Jung. The CCFM Monte Carlo Generator CASCADE. *Comput. Phys. Commun.*, 143:100–111, 2002, hep-ph/0109102.

[28] Jürgen Kroseberg. *A Measurement of Beauty Production in High-Energy Positron-Proton Scattering.* PhD thesis, Universität Zürich, 2002.

[29] Giuseppe Marchesini. QCD Coherence in the Structure Function and Associated Distributions at Small x. *Nucl. Phys.*, B445:49–80, 1995, hep-ph/9412327.

[30] Andreas Meyer. private communication.

[31] Torbjorn Sjostrand. High-Energy Physics Event Generation with PYTHIA 5.7 and JETSET 7.4. *Comput. Phys. Commun.*, 82:74–90, 1994.

[32] Michael Steder. Myonidentifikation im Kalorimeter des H1-Detektors mit Neuronalen Netzen. Master's thesis, Universität Hamburg, 2005.

Danksagung

Ich bedanke mich bei allen, die diese Arbeit ermöglicht und begleitet haben.

Zuallererst sei Frau Prof. Dr. Naroska genannt, die mich auf Empfehlung von Herrn Prof. Dr. Büßer in ihre Arbeitsgruppe aufgenommen hat. Ihr verdanke ich eine hervorragende Betreuung und Unterstützung nicht nur, aber vor allem, in der letzten Phase dieser Arbeit. Herrn Professor Dr. Schleper danke ich für die Erstellung des Zweitgutachtens.

Andreas Meyer sei gedankt für die geduldige Einführung in die Beauty-Analyse, die umfassende Programmsammlung, auf der ich meine Analyse aufbauen konnte, und das ausgiebige Korrekturlesen. Auch Jenny List und Brian Grell danke ich für das Korrekturlesen.

Gedankt sei weiterhin allen jetzigen und ehemaligen Mitgliedern der Hamburger Arbeitsgruppe, die mir eine schöne Zeit bei H1 bereitet haben. Hier seien Mária Martišíková, Lars Finke, Philipp Fleischmann, Duncan Brown, Shiraz Habib, Michael Steder, Christian Sager, Christian Berg, Christian Helebrant, Tammo Gsänger und Lea Hallermann genannt.

Auch außerhalb der Kollaboration habe ich wertvolle Unterstützung gefunden. Insbesondere danke ich meiner Freundin Ana, die alle Höhen und Tiefen dieser Arbeit mitgemacht hat. Meine Kommilitonen René Eiselt, Gesa Netzeband und Markus Ball haben meine Studienzeit durch viel schöne Erlebnisse bereichert. Besonders bedanke ich mich bei meinen Eltern, die mich in meinem gesamten Studium nicht nur finanziell unterstützt haben.